

Article

Green Synthesis of Metal-Organic Framework Bacterial Cellulose Nanocomposites for Separation Applications

Radwa M. Ashour^{1,2,*}, Ahmed F. Abdel-Magied^{1,2,*}, Qiong Wu³, Richard T. Olsson^{3,*} and Kerstin Forsberg^{1,*}

¹ Department of Chemical Engineering, KTH Royal Institute of Technology, 100 44 Stockholm, Sweden

² Nuclear Materials Authority, P.O. Box 530, ElMaadi, Cairo 11381, Egypt

³ Department of Fibre and Polymer Technology, KTH Royal Institute of Technology, 100 44 Stockholm, Sweden; qiongwu@kth.se

* Correspondence: radwa@kth.se (R.M.A.); fawzy@kth.se (A.F.A.-M.); rols@kth.se (R.T.O.); kerstino@kth.se (K.F.)

† These authors contributed equally to this work.

Received: 30 March 2020; Accepted: 9 May 2020; Published: 13 May 2020

Abstract: Metal organic frameworks (MOFs) are porous crystalline materials that can be designed to act as selective adsorbents. Due to their high porosity they can possess very high adsorption capacities. However, overcoming the brittleness of these crystalline materials is a challenge for many industrial applications. In order to make use of MOFs for large-scale liquid phase separation processes they can be immobilized on solid supports. For this purpose, nanocellulose can be considered as a promising supporting material due to its high flexibility and biocompatibility. In this study a novel flexible nanocellulose MOF composite material was synthesised in aqueous media by a novel and straightforward in situ one-pot green method. The material consisted of MOF particles of the type MIL-100(Fe) (from Material Institute de Lavoisier, containing Fe(III) 1,3,5-benzenetricarboxylate) immobilized onto bacterial cellulose (BC) nanofibers. The novel nanocomposite material was applied to efficiently separate arsenic and Rhodamine B from aqueous solution, achieving adsorption capacities of 4.81, and 2.77 mg g⁻¹, respectively. The adsorption process could be well modelled by the nonlinear pseudo-second-order fitting.

Keywords: bacterial cellulose; metal organic framework; nanocomposite; adsorption

1. Introduction

Since the advent of the industrial revolution, dumping of large amounts of industrial waste including dyes and toxic metal ions has contributed to the serious issue of water pollution [1]. Consequently, various techniques for the removal of organic dyes and toxic metal ions from aqueous solutions, including adsorption [2–4], chemical precipitation [5], ion exchange [6], and membrane separation [7] have been evaluated. Amongst these, adsorption is proven to be an effective and convenient method for water purification due to the ease of operation and the low cost. However, for nanoadsorbents, complicated and tedious high-speed centrifugation or separation of the adsorbent using filtration is required, hindering the extensive application of such adsorbents. Therefore, development of novel materials for water treatment is of great interest.

Metal-organic frameworks (MOFs) are porous hybrid materials composed of metal ions bridged by polydentate organic ligands. Since the synthesis of MOF-5 reported by Yaghi and co-workers (1999) [8], MOFs have received significant attention due to their high crystallinity, large surface areas, thermal stability and unique porosity. MOF applications are numerous, including catalysis [9–11],

drug delivery [12], gas storage [13–15], chemical sensing [16], and separation [17–19]. The properties of the MOF structures can be easily tuned by selecting different metal ions and bridging organic polydentate ligands, and the design and preparation of new MOFs into various structures is still of great interest [20]. However, the handling and processing of MOFs are also challenging due to the crystalline nature of the MOFs, making them brittle and fragile as inorganic materials [21,22]. To tackle this problem, efforts have been made to entrap MOFs onto various substrates, thus realizing a combination of their advantages, while circumventing, and to different extents addressing the MOF's shortcomings. Various MOF composites have been successfully prepared via direct deposition of MOF particles on solid substrate surfaces [23]. However, although such synthetic protocols produce a new types of functional materials, their applications are limited by their constrained morphologies and synthetic protocols. Usually, substrate surface modifications are needed to increase the MOF loading and conditions must be applied that in many cases involve environmentally hazardous reagents [24].

Membrane adsorption can be applied to separate metal ions in larger scale. For this purpose, a column is used that is packed with a short stack of porous membranes with a large diameter, to avoid high pressure drops. In membrane adsorption fibres can act as an adsorbing medium. One advantage of this technology is that process flow rates can be orders of magnitudes higher than for packed beds, without elevated pressure. The challenge is to achieve a comparable adsorption capacity to that of packed beds. However, by using functionalised nanofibers the adsorption capacities can even exceed packed bed resins due to the very high surface area of the fibres. Refined low-cost biopolymers such as nanocellulose can here be considered as a promising supporting material due to its very interesting properties, such as high chemical purity and crystallinity, flexibility and biocompatibility [25]. Furthermore, nanocellulose is the most abundant and renewable green biopolymer and a sustainable raw material. Bacterial cellulose (BC) fibrils are one of the most frequently reported nanocellulose types. It is produced by cultivating *Acetobacter xylinum* in the presence of sugar [26]. BC nanofibrillar cellulose shows great promise to be used as a substrate since it can be generated in high yield from its natural source containing >70 wt% crystalline cellulose. It also shows high aspect ratio due to its fibrillar length reaching up to several micrometers while at the same time providing average fiber diameters of 20–100 nm [27]. To date, only a few studies have reported integration of MOFs onto nanocellulose. Matsumoto and co-workers reported the successful growth of MOFs (up to 44% loading) at carboxyl groups on crystalline TEMPO-oxidized cellulose nanofibers and prepared densely packed films coated on a filter paper, which demonstrated high gas separation selectivity [28]. Zhu and co-workers have developed a strategy for combining MOFs and cellulose nanocrystals into a highly functional aerogel for separation applications, where the MOF loading can be easily tailored by changing the initial ratio of the components [29]. Recently, Au-Duong and co-workers successfully demonstrated that a flexible nanocomposite pellicle combining imidazolate framework-8 (ZIF-8) and wet BC could be simply synthesized when polydopamine surface coating on cellulose nanofibers is applied in advance [30].

Herein, we report a new, straightforward, environmentally friendly in situ green strategy to integrate MOF Material Institute de Lavoisier-100(Fe), Fe-BTC (alternatively known as MIL-100(Fe); BTC = 1,3,5-benzenetricarboxylate) [31] into BC in aqueous media. This method makes it possible to synthesize cellulose-based metal organic framework nanocomposite material without using any chemical modifier. The synthetic approach provides a general strategy to prepare such nanocomposites for various applications. The synthesized MIL-100(Fe)@BC nanocomposite not only maintained high micro/ mesoporosities of the MIL-100(Fe) particles, but also combined flexibility and shapeability of the BC crystal support. This combination produces a shapeable, low-cost, chemically inert and scalable product that can be used in various applications, for example, water purification. The synthesized hybrid MIL-100(Fe)@BC nanocomposite was evaluated in water purification as an efficient adsorbent for the removal of arsenic As(III), and Rhodamine B.

2. Materials and Methods

Materials: Iron(III) chloride hexahydrate ($\geq 98\%$), 1,3,5-benzenetricarboxylate (98%) were purchased from VWR (Stockholm, Sweden). Rhodamine B ($\geq 95\%$) was purchased from Sigma-Aldrich (Stockholm, Sweden). Arsenic pure single-element standard (1000 mg L^{-1}) was purchased from PerkinElmer (Stockholm, Sweden). All chemicals were used as received without further purification. Deionized water (resistivity: $18.2 \text{ M}\Omega/\text{cm}$) was used to prepare aqueous solutions. The bacterial cellulose nanofibrils were extracted from a uniformly grown bacterial cellulose pellicle, using 1 L aqueous sulphuric acid solution containing 30 vol% of reagent grade acid (Merck KGaA, Stockholm, Sweden) under stirring at $60 \pm 0.5 \text{ }^\circ\text{C}$ (300 rpm). The total time for the extraction was 7 h, i.e., until no visible cellulose pieces were apparent and the solution had acquired an even beige color. The supernatant was decanted after a first isothermal centrifugation at 10,000 rpm for 10 min and replaced with fresh MilliQ water. The procedure was repeated twice until a neutral pH was obtained. The yield of the extraction was ca. 60 wt% based on the dry weight of the bacterial cellulose. The surface area of the bacterial cellulose nanofibrils was approximated to ca. $159 \text{ m}^2 \text{ g}^{-1}$ from size distributions and counting of a minimum of 500 fibrils deposited on TEM grids. The approximated surface area was in relatively good agreement with the surface area of $189 \text{ m}^2 \text{ g}^{-1}$ reported by Roman et al. [32] while larger than the experimental value of $103 \text{ m}^2 \text{ g}^{-1}$ for dry bacterial cellulose fibrils by Olsson et al. [26].

In situ one-pot synthesis of MIL-100(Fe)@BC: Iron(III) chloride hexahydrate (164 mg) was added to 50 mL of well-sonicated BC (2.0 wt% dry contents) and the reaction mixture was refluxed at $100 \text{ }^\circ\text{C}$ under mechanical stirring (350 rpm). After 30 min, different concentrations of 1,3,5-benzenetricarboxylate were dissolved in 4 mL of deionized water and added to the reaction mixture, which was kept for an additional 30 min at $100 \text{ }^\circ\text{C}$. The final suspension was centrifuged and washed 3 times with acetone followed by deionized water. The product was placed in a plastic tube that was directly frozen by immersing the tube in liquid N_2 followed by freeze-drying to obtain the final hybrid nanocomposite MIL-100(Fe)@BC, that was activated at $100 \text{ }^\circ\text{C}$ for 12 h before being used as an adsorbent.

Adsorption: The adsorption experiments were carried out at room temperature. Adsorption studies were carried out by soaking MIL-100(Fe)@BC (0.18 g) in aqueous solution containing different contaminants (20 mg L^{-1} of As(III) (50 mL) and 10 mg L^{-1} of Rhodamine B (40 mL)) for a certain amount of time. After adsorption, the MIL-100(Fe)@BC nanocomposite was separated from the aqueous solution, and the dye concentration was analyzed by UV-vis based on a calibration curve prepared from solutions with known contaminant concentration at the maximum wavelengths (554 nm). The concentration of As(III) in the supernatant was determined by inductively coupled plasma atomic emission spectroscopy (ICP-OES, Waltham, MA, USA). The adsorption experiments were performed in duplicate/triplicate and the average values of total adsorption are reported. The adsorption capacity (q_t , mg g^{-1}) and the removal % at time t were determined using Equations (1) and (2).

$$q_t = \frac{(C_0 - C_t)V}{m} \quad (1)$$

$$\text{Removal (\%)} = \frac{C_0 - C_t}{C_0} \times 100 \quad (2)$$

where C_0 and C_t (mg L^{-1}) are the initial concentration and concentration at time t in aqueous solution, respectively, V (L) is the volume of the aqueous phase, and m (g) is the mass of the MIL-100(Fe)@BC nanocomposite. The kinetics of the adsorption process was investigated by fitting the nonlinear forms of pseudo-first order and pseudo-second order models to the data using Equations (3) and (4).

$$q_t = q_e(1 - e^{-k_1 t}) \quad (3)$$

$$q_t = \frac{k_2 q_e^2 t}{1 + k_2 q_e t} \quad (4)$$

MIL-100(Fe)@BC nanocomposite (Figure 1c). The BET surface area of the MIL-100(Fe)@BC nanocomposite is $47.13 \pm 0.15 \text{ m}^2/\text{g}$.

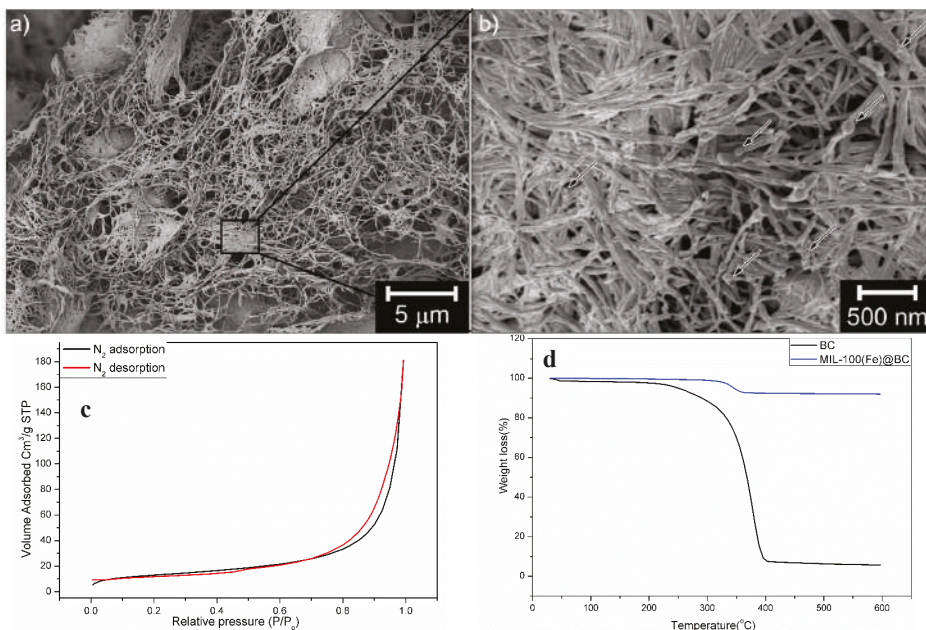


Figure 1. (a,b) SEM image of hybrid MIL-100(Fe)@BC nanocomposite (BTC/Fe(III) = 120), (c) Brunauer-Emmett-Teller (BET) analysis of MIL-100(Fe)@BC (BTC/Fe(III) = 120), and (d) thermogravimetric analysis (TGA) of bacterial cellulose (BC) and MIL-100(Fe)@BC.

Figure 1d shows the thermogravimetric analysis (TGA) of the MOF-cellulose hybrid material and the BC. A gradual decrease in weight of ca. 0.3 wt% occurred up to ca. 180 °C, which was synonymous with structurally bonded water entrapped in the porous material. Further condensation and densification (ca. 1 wt%) of the material occurred from ca. 180 °C until the degradation temperature of the cellulose was reached at ca. 350 °C. The sharp weight loss to 91.8 wt% (of the materials original weight) at 350 °C could thus be correlated to a total loading of bacterial cellulose equivalent with ca. 8 wt%. At temperatures above 400 °C, degradation and evaporation of carbon residuals occurred. The density of the entire cylindrical sample (Scheme 1) could further be derived from the volume of the sample and its weight. The low density of MIL-100(Fe)@BC was 47.8 mg cm^{-3} , implying that the nanocomposite was very porous with a large accessible surface area.

Owing to their high specific surface area, MOFs are intended for various applications [34]. Herein, we evaluate the synthesized MIL-100(Fe)@BC nanocomposite in water purification to demonstrate the adsorption ability of MOF-cellulose materials as interpenetrating networks with an integrated cellulose phase. Arsenic is recognized as one of the most hazardous metal ions in drinking water and is listed by the World Health Organization among the top 10 major public health concerns. In this context, the adsorption capacity of the MIL-100(Fe)@BC nanocomposite was tested for the removal of As(III) from aqueous solutions. In the tests, a small MIL-100(Fe)@BC nanocomposite (0.18 g) was soaked into 50 mL of an aqueous solution containing As(III) (20 ppm) (See Experimental Section for more details). The adsorption capacities (q_t in mg g^{-1}) and removal (%) of As(III) at different times (t) are shown in Figure 2a. High adsorption capacity for As(III) adsorption onto MIL-100(Fe)@BC nanocomposite was observed (removal efficiency $\approx 85\%$ within 72 h).

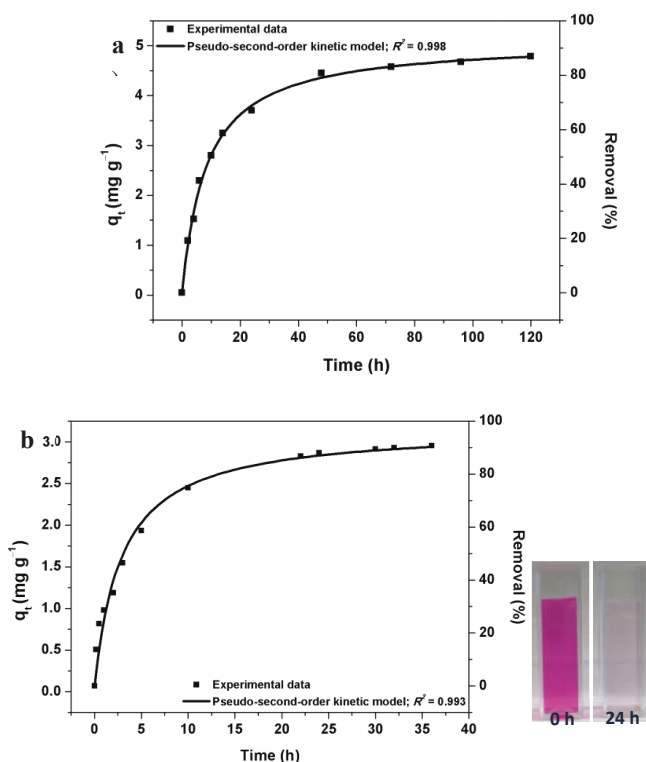


Figure 2. Adsorption capacity versus time, and the nonlinear pseudo-second-order fitting for the adsorption of As(III) (a); and Rhodamine B (b) on MIL-100(Fe)@BC nanocomposite, respectively. The inset shows a photograph of the Rhodamine B aqueous solutions before and after the adsorption process.

Two kinetic models, the pseudo-first-order and pseudo-second-order models, were used to investigate the mechanism of As(III) adsorption on the MIL-100(Fe)@BC nanocomposite (Figure S3a and Figure 2a, respectively). The nonlinear pseudo-second-order kinetic model fitted well to the experimental data (Figure 2a), and the experimental $q_{t,exp}$ values and the calculated $q_{t,cal}$ values obtained from the pseudo-second-order kinetic model are in good agreement (Table S1). The calculated values of the pseudo-second-order parameters are listed in Table S1. The fitting results indicate that the BC network is not hindering the accessibility of the MIL-100(Fe) pores and most of the MIL-100(Fe) particles are functional in the adsorption of As(III) onto the MIL-100(Fe)@BC nanocomposite as a chemical process via surface complexation [35]. The total concentration of Fe in the solution was measured by ICP-OES after the adsorption experiments in order to investigate the stability of the material. No Fe was detected, indicating a high stability of the synthesized MIL-100(Fe)@BC nanocomposite under the employed conditions.

Removal of organic dyes from aqueous solution is another significant challenge in the field of water purification. Among several organic dyes, Rhodamine B was chosen for the present study due to its extensive use as a colorant in the textile and food industries [36]. Rhodamine B was used as a model tracer to monitor the adsorption capacity and kinetics for adsorption onto the MIL-100(Fe)@BC nanocomposite. Herein, a small amount of the nanocomposite MIL-100(Fe)@BC (0.18 g) was added to 40 mL of an aqueous solution containing Rhodamine B (10 ppm), and the dye concentration in the solution at certain time was determined by UV-Vis (see Experimental Section for more details). The adsorption experiments were carried out at room temperature. The adsorption capacity (q_t) and

removal percentage of Rhodamine B as a function of time (t) are shown in Figure 2b. The adsorption capacities for Rhodamine B increased with increasing time, and reached equilibrium within 24 h, achieving a removal percentage of 85%. The high adsorption capacity of the MIL-100(Fe)@BC nanocomposite results from the hierarchical porosity and small MIL-100(Fe) crystals integrated within the BC network, which offer a high number of external surface sites for the adsorption.

The kinetics for Rhodamine B adsorption onto the MIL-100(Fe)@BC nanocomposite was studied using pseudo-first-order and pseudo-second-order models (Figure S3b and Figure 2b, respectively). The obtained experimental data for the adsorption process, determined by UV-Vis at 554, fitted very well with the pseudo-second-order kinetic model (Figure 2b), which indicate that the adsorption was controlled by intraparticle diffusion [37]. The calculated values of the pseudo-second-order parameters are listed in Table S1. After soaking the MIL-100(Fe)@BC nanocomposite with the Rhodamine B aqueous solution, the pink dye solution gradually faded into colorless over time, and its UV-Vis maximum absorption peak at 554 nm reduced significantly (Figure S4). The inset in Figure 2b visually confirms the color change of Rhodamine B aqueous solution before and after the adsorption process by MIL-100(Fe)@BC nanocomposite. The adsorption mechanism can be attributed to the electrostatic interactions between MIL-100(Fe)@BC nanocomposite and Rhodamine B [38].

A comparison of the obtained results for As(III) and Rhodamine B removal using MIL-100(Fe)@BC nanocomposite with other reported systems is summarized in Table 1.

Table 1. Comparison of As(III) and Rhodamine B removal with other reported adsorbents.

Adsorbents	q_e (mg g ⁻¹)	Ref.
As(III) Removal		
MIL-53(Al)-graphene oxide	65.0	[39]
Surfactant-modified montmorillonite	1.48	[40]
Magnetic pinecone biomass	18.02	[41]
Zn-MOF	49.50	[42]
MIL-100(Fe)	120	[35]
MIL-100(Fe)@BC	4.81	This work
Rhodamine B Removal		
Hypercross-linked polymeric adsorbent	2.1	[43]
Mango leaf powder	3.31	[44]
Zn-MOF	3.750	[45]
Fe ₃ O ₄ /MIL-100(Fe)	28.36	[38]
MIL-100(Fe)@BC	2.77	This work

4. Conclusions

A MIL-100(Fe)@BC nanocomposite was synthesized by an environmentally friendly method using water as solvent. The bacterial cellulose (BC) acted as structural support during the lyophilisation of the MIL-100(Fe), which resulted in a flexible and light weight material suitable for membrane adsorption processes. It was demonstrated that the size of the loaded MIL-100(Fe) particles on the BC can be tailored by changing the initial ratio of MIL-100(Fe) precursors. The synthesized nanocomposite is efficient in removal of As(III) and Rhodamine B from aqueous solutions. The kinetic studies revealed that the adsorption of As(III) and Rhodamine B was best fitted to the pseudo-second order model. The synthetic approach provides a simple strategy to prepare the MOFs@BC nanocomposites for various applications, in particular for water purification. Further studies on how to immobilize other types of MOFs using BC could be explored.

Supplementary Materials: The following are available online at <http://www.mdpi.com/2073-4360/12/5/1104/s1>, Figure S1: Photograph (inset) and TEM image of MIL-100(Fe)@BC nanocomposite (BTC/Fe(III) = 25), Figure S2: XRD patterns of (a) BC and (b) MIL-100(Fe)@BC nanocomposite (BTC/Fe(III) = 120), Figure S3: Plots of pseudo-first-order kinetics models for the adsorption of As(III) (a) and Rhodamine B (b) using MIL-100(Fe)@BC nanocomposite (BTC/Fe(III) = 120), Figure S4: UV-Vis spectra for the adsorption of Rhodamine B using MIL-100(Fe)@BC nanocomposite (BTC/Fe(III) = 120) at different time, and Table S1: Kinetic parameters for the adsorption of As(III) and Rhodamine B using MIL-100(Fe)@BC nanocomposite.

Author Contributions: R.M.A., A.F.A.-M. and Q.W.: Investigation; R.T.O. and K.F.: Validation; R.M.A. and A.F.A.-M.: Writing—original draft; R.T.O. and K.F.: Writing—Review & Editing; R.M.A., A.F.A.-M., R.T.O. and K.F.: Methodology. All authors have read and agreed to the published version of the manuscript.

Funding: This work was funded by a start-up grant at KTH Royal Institute of Technology.

Conflicts of Interest: The authors declare no conflict of interest.

References

1. Yin, F.; Deng, X.; Jin, Q.; Yuan, Y.; Zhao, C. The impacts of climate change and human activities on grassland productivity in Qinghai Province, China. *Front. Earth Sci.* **2014**, *8*, 93–103. [[CrossRef](#)]
2. Geisse, R.A.; Ngule, M.C.; Genna, T.D. Removal of lead ions from water using thiophene-functionalized metal–organic frameworks. *Chem. Commun.* **2020**, *56*, 237–240. [[CrossRef](#)] [[PubMed](#)]
3. Li, D.; Tian, X.; Wang, Z.; Guan, Z.; Li, X.; Qiao, H.; Ke, H.; Luo, L.; Wei, Q. Multifunctional adsorbent based on metal-organic framework modified bacterial cellulose/chitosan composite aerogel for high efficient removal of heavy metal ion and organic pollutant. *Chem. Eng. J.* **2020**, *383*, 123127. [[CrossRef](#)]
4. Huang, L.; He, M.; Chen, B.; Hu, B. Magnetic Zr-MOFs nanocomposites for rapid removal of heavy metal ions and dyes from water. *Chemosphere* **2018**, *199*, 435–444. [[CrossRef](#)]
5. Chen, Q.; Luo, Z.; Hills, C.; Xue, G.; Tyrer, M. Precipitation of heavy metals from wastewater using simulated flue gas: Sequent additions of fly ash, lime and carbon dioxide. *Water Res.* **2009**, *43*, 2605–2614. [[CrossRef](#)] [[PubMed](#)]
6. Wang, Z.; Feng, Y.; Hao, X.; Huang, W.; Feng, X. A novel potential-responsive ion exchange film system for heavy metal removal. *J. Mater. Chem. A* **2014**, *2*, 10263–10272. [[CrossRef](#)]
7. Tofighy, A.M.; Mohammadi, T. Divalent heavy metal ions removal from contaminated water using positively charged membrane prepared from a new carbon nanomaterial and HPEI. *Chem. Eng. J.* **2020**, *388*, 124192. [[CrossRef](#)]
8. Li, H.; Eddaoudi, M.; O’Keeffe, M.; Yaghi, O.M. Design and synthesis of an exceptionally stable and highly porous metal-organic framework. *Nature* **1999**, *402*, 276. [[CrossRef](#)]
9. David, F.; Sonia, A.; Catherine, P. Metal-Organic frameworks: Opportunities for catalysis. *Angew. Chem. Int. Ed.* **2009**, *48*, 7502–7513.
10. Lee, J.; Farha, O.K.; Roberts, J.; Scheidt, K.A.; Nguyen, S.T.; Hupp, J.T. Metal-Organic framework materials as catalysts. *Chem. Soc. Rev.* **2009**, *38*, 1450–1459. [[CrossRef](#)]
11. Zhu, L.; Liu, X.-Q.; Jiang, H.-L.; Sun, L.-B. Metal-Organic frameworks for heterogeneous basic catalysis. *Chem. Rev.* **2017**, *117*, 8129–8176. [[CrossRef](#)] [[PubMed](#)]
12. Wu, M.-X.; Yang, Y.-W. Metal-Organic framework (MOF)-based drug/Cargo delivery and cancer therapy. *Adv. Mater.* **2017**, *29*, 1606134. [[CrossRef](#)] [[PubMed](#)]
13. Alkordi, M.H.; Belmabkhout, Y.; Cairns, A.; Eddaoudi, M. Metal–organic frameworks for H₂ and CH₄ storage: Insights on the pore geometry–sorption energetics relationship. *IUCr* **2017**, *4*, 131–135. [[CrossRef](#)] [[PubMed](#)]
14. Tian, T.; Zeng, Z.; Vulpe, D.; Casco, M.E.; Divitini, G.; Midgley, P.A.; Silvestre-Albero, J.; Tan, J.-C.; Moghadam, P.Z.; Fairen-Jimenez, D. A sol-gel monolithic metal-organic framework with enhanced methane uptake. *Nat. Mater.* **2017**, *17*, 174. [[CrossRef](#)]
15. Zheng, H.; Zhang, Y.; Liu, L.; Wan, W.; Guo, P.; Nyström, A.M.; Zou, X. One-pot synthesis of metal–organic frameworks with encapsulated target molecules and their applications for controlled drug delivery. *J. Am. Chem. Soc.* **2016**, *138*, 962–968. [[CrossRef](#)]
16. Chen, B.; Yang, Z.; Zhu, Y.; Xia, Y. Zeolitic imidazolate framework materials: Recent progress in synthesis and applications. *J. Mater. Chem. A* **2014**, *2*, 16811–16831. [[CrossRef](#)]

17. Li, J.-R.; Sculley, J.; Zhou, H.-C. Metal-organic frameworks for separations. *Chem. Rev.* **2012**, *112*, 869–932. [[CrossRef](#)]
18. Qiu, S.; Xue, M.; Zhu, G. Metal–organic framework membranes: From synthesis to separation application. *Chem. Soc. Rev.* **2014**, *43*, 6116–6140. [[CrossRef](#)]
19. Abdel-Magied, A.F.; Abdelhamid, H.N.; Ashour, R.M.; Zou, X.; Forsberg, K. Hierarchical porous zeolitic imidazolate frameworks nanoparticles for efficient adsorption of rare-earth elements. *Microporous Mesoporous Mater.* **2019**, *278*, 175–184. [[CrossRef](#)]
20. Almeida Paz, F.A.; Klinowski, J.; Vilela SM, F.; Tomé JP, C.; Cavaleiro JA, S.; Rocha, J. Ligand design for functional metal–organic frameworks. *Chem. Soc. Rev.* **2012**, *41*, 1088–1110. [[CrossRef](#)]
21. Chen, Y.; Huang, X.; Zhang, S.; Li, S.; Cao, S.; Pei, X.; Zhou, J.; Feng, X.; Wang, B. Shaping of metal–organic frameworks: From fluid to shaped bodies and robust foams. *J. Am. Chem. Soc.* **2016**, *138*, 10810–10813. [[CrossRef](#)] [[PubMed](#)]
22. Liu, C.; Zhang, J.; Zheng, L.; Zhang, J.; Sang, X.; Kang, X.; Zhang, B.; Luo, T.; Tan, X.; Han, B. Metal-organic framework for emulsifying carbon dioxide and water. *Angew. Chem. Int. Ed.* **2016**, *55*, 11372–11376. [[CrossRef](#)] [[PubMed](#)]
23. Bétard, A.; Fischer, R.A. Metal–organic framework thin films: From fundamentals to applications. *Chem. Rev.* **2012**, *112*, 1055–1083. [[CrossRef](#)] [[PubMed](#)]
24. Denny, M.S.; Cohen, S.M. In situ modification of metal–organic frameworks in mixed-matrix membranes. *Angew. Chem. Int. Ed.* **2015**, *54*, 9029–9032. [[CrossRef](#)]
25. Moon, R.J.; Martini, A.; Nairn, J.; Simonsen, J.; Youngblood, J. Cellulose nanomaterials review: Structure, properties and nanocomposites. *Chem. Soc. Rev.* **2011**, *40*, 3941–3994. [[CrossRef](#)]
26. Olsson, R.T.; Azizi Samir MA, S.; Salazar-Alvarez, G.; Belova, L.; Ström, V.; Berglund, L.A.; Ikkala, O.; Nogués, J.; Gedde, U.W. Making flexible magnetic aerogels and stiff magnetic nanopaper using cellulose nanofibrils as templates. *Nat. Nanotechnol.* **2010**, *5*, 584. [[CrossRef](#)]
27. Lee, K.Y. *Nanocellulose and Sustainability: Production, Properties, Applications, and Case Studies*; CRC Press: Boca Raton, FL, USA, 2018.
28. Matsumoto, M.; Kitaoka, T. Ultraselective gas separation by nanoporous metal-organic frameworks embedded in gas-barrier nanocellulose films. *Adv. Mater.* **2016**, *28*, 1765–1769. [[CrossRef](#)]
29. Zhu, H.; Yang, X.; Cranston, E.D.; Zhu, S. Flexible and porous nanocellulose aerogels with high loadings of metal–organic-framework particles for separations applications. *Adv. Mater.* **2016**, *28*, 7652–7657. [[CrossRef](#)]
30. Au-Duong, A.-N.; Lee, C.-K. Flexible metal–organic framework-bacterial cellulose nanocomposite for iodine capture. *Cryst. Growth Des.* **2018**, *18*, 356–363. [[CrossRef](#)]
31. Férey, G.; Serre, C.; Mellot-Draznieks, C.; Millange, F.; Surblé, S.; Dutour, J.; Margiolaki, I. A hybrid solid with giant pores prepared by a combination of targeted chemistry, simulation, and powder diffraction. *Angew. Chem. Int. Ed.* **2004**, *43*, 6296–6301. [[CrossRef](#)]
32. Roman, M.; Winter, W.T. Effect of sulfate groups from sulfuric acid hydrolysis on the thermal degradation behavior of bacterial cellulose. *Biomacromolecules* **2004**, *5*, 1671–1677. [[CrossRef](#)] [[PubMed](#)]
33. Cravillon, J.; Nayuk, R.; Springer, S.; Feldhoff, A.; Huber, K.; Wiebcke, M. Controlling Zeolitic imidazolate framework nano- and microcrystal formation: Insight into crystal growth by time-resolved in situ static light scattering. *Chem. Mater.* **2011**, *23*, 2130–2141. [[CrossRef](#)]
34. Pettinari, C.; Marchetti, F.; Mosca, N.; Tosi, G.; Drozdov, A. Applications of metal-organic frameworks. *Polym. Int.* **2017**, *66*, 731–744. [[CrossRef](#)]
35. Georgiou, Y.; Perman, J.A.; Bourlino, A.B.; Deligiannakis, Y. Highly efficient arsenite [As(III)] adsorption by an [MIL-100(Fe)] metal–organic framework: Structural and mechanistic insights. *J. Phys. Chem. C* **2018**, *122*, 4859–4869. [[CrossRef](#)]
36. Mohammadi, M.; Hassani, A.J.; Mohamed, A.R.; Najafpour, G.D. Removal of Rhodamine B from aqueous solution using Palm shell-based activated carbon: Adsorption and kinetic studies. *J. Chem. Eng. Data* **2010**, *55*, 5777–5785. [[CrossRef](#)]
37. Plazinski, W.; Dziuba, J.; Rudzinski, W. Modeling of sorption kinetics: The pseudo-second order equation and the sorbate intraparticle diffusivity. *Adsorption* **2013**, *19*, 1055–1064. [[CrossRef](#)]
38. Haochi, L.; Xiaohui, R.; Ligang, C.J. Synthesis and characterization of magnetic metal–organic framework for the adsorptive removal of Rhodamine B from aqueous solution. *Ind. Eng. Chem.* **2016**, *34*, 278–285.

39. Tonoy, C.; Lei, Z.; Junqing, Z.; Srijan, A. Removal of Arsenic(III) from aqueous solution using metal organic framework-graphene oxide nanocomposite. *Nanomaterials* **2018**, *8*, 1062.
40. Samira, S.; Ghasem, A.; Faramarz, M.; Abdolreza, K.; Kazem, G.; Ehsan, N. Application of surfactant-modified montmorillonite for As (III) removal from aqueous solutions: Kinetics and isotherm study. *Desalin. Water Treat.* **2018**, *115*, 236–248.
41. Agnes, P.; Eliazar, B.N.; Augustine, E.O. Enhanced Arsenic (III) adsorption from aqueous solution by magnetic pine cone biomass. *Mater. Chem. Phys.* **2019**, *222*, 20–30.
42. Jian, M.; Liu, B.; Zhang, G.; Liu, R.; Zhang, X. Adsorptive removal of arsenic from aqueous solution by zeolitic imidazolate framework-8 (ZIF-8) nanoparticles. *Colloids Surf. Physicochem. Eng. Asp.* **2015**, *465*, 67–76. [[CrossRef](#)]
43. Huang, J.-H.; Huang, K.-L.; Liu, S.-Q.; Wang, A.-T.; Yan, C. Adsorption of Rhodamine B and methyl orange on a hypercrosslinked polymeric adsorbent in aqueous solution. *Colloid Surf. A Physicochem. Eng. Asp.* **2008**, *330*, 55. [[CrossRef](#)]
44. Khan, T.A.; Sharma, S.; Ali, I. Adsorption of Rhodamine B dye from aqueous solution onto acid activated mango (*Mangifera indica*) leaf powder: Equilibrium, kinetic and thermodynamic studies. *Toxicol. Environ. Health Sci.* **2011**, *3*, 286–297.
45. Zhang, J.; Li, F.; Sun, Q. Rapid and selective adsorption of cationic dyes by a unique metal-organic framework with decorated pore surface. *Appl. Surf. Sci.* **2018**, *440*, 1219–1226. [[CrossRef](#)]



© 2020 by the authors. Licensee MDPI, Basel, Switzerland. This article is an open access article distributed under the terms and conditions of the Creative Commons Attribution (CC BY) license (<http://creativecommons.org/licenses/by/4.0/>).

Article

Development of a Highly Proliferated Bilayer Coating on 316L Stainless Steel Implants

Fatemeh Khosravi ¹, Saied Nouri Khorasani ^{1,*}, Shahla Khalili ¹, Rasoul Esmaeely Neisiany ^{2,*}, Erfan Rezvani Ghomi ³, Fatemeh Ejeian ⁴, Oisik Das ^{5,*} and Mohammad Hossein Nasr-Esfahani ^{4,*}

¹ Department of Chemical Engineering, Isfahan University of Technology, Isfahan 8415683111, Iran; f.khosravi@ce.iut.ac.ir (F.K.); shahla.khalili65@gmail.com (S.K.)

² Department of Materials and Polymer Engineering, Faculty of Engineering, Hakim Sabzevari University, Sabzevar 9617976487, Iran

³ Department of Mechanical Engineering, Center for Nanofibers and Nanotechnology, National University of Singapore, Singapore 119260, Singapore; erfanzrezvani@u.nus.edu

⁴ Department of Cellular Biotechnology, Cell Science Research Center, Royan Institute for Biotechnology, ACECR, Isfahan 8159358686, Iran; fatemeh.eje@gmail.com

⁵ Material Science Division, Department of Engineering Sciences and Mathematics, Luleå University of Technology, 97187 Luleå, Sweden

* Correspondence: saied@cc.iut.ac.ir (S.N.K.); r.esmaeely@hsu.ac.ir (R.E.N.); oisik.das@ltu.se (O.D.); mh.nasr-esfahani@royaninstitute.org (M.H.N.-E.)

Received: 1 April 2020; Accepted: 28 April 2020; Published: 1 May 2020

Abstract: In this research, a bilayer coating has been applied on the surface of 316 L stainless steel (316LSS) to provide highly proliferated metallic implants for bone regeneration. The first layer was prepared using electrophoretic deposition of graphene oxide (GO), while the top layer was coated utilizing electrospinning of poly (ϵ -caprolactone) (PCL)/gelatin (Ge)/forsterite solutions. The morphology, porosity, wettability, biodegradability, bioactivity, cell attachment and cell viability of the prepared coatings were evaluated. The Field Emission Scanning Electron Microscopy (FESEM) results revealed the formation of uniform, continuous, and bead-free nanofibers. The Energy Dispersive X-ray (EDS) results confirmed well-distributed forsterite nanoparticles in the structure of the top coating. The porosity of the electrospun nanofibers was found to be above 70%. The water contact angle measurements indicated an improvement in the wettability of the coating by increasing the amount of nanoparticles. Furthermore, the electrospun nanofibers containing 1 and 3 wt.% of forsterite nanoparticles showed significant bioactivity after soaking in the simulated body fluid (SBF) solution for 21 days. In addition, to investigate the in vitro analysis, the MG-63 cells were cultured on the PCL/Ge/forsterite and GO-PCL/Ge/forsterite coatings. The results confirmed an excellent cell adhesion along with considerable cell growth and proliferation. It should be also noted that the existence of the forsterite nanoparticles and the GO layer substantially enhanced the cell proliferation of the coatings.

Keywords: biocomposites; nanofibers; electrospinning; cell culture; graphene oxide

1. Introduction

At present, numerous types of bone diseases, e.g., bone fractures, bone infections, bone cancers, and genetic diseases are rising due to increasing prevalence of physical inactivity, obesity and lack of safe exercising [1]. It is reported that over 20 million people suffer from bone disorders and clinical troubles annually, making this an global issue [2]. Traditional bone regeneration methods were based on utilizing autograft and allograft [3]. There are serious drawbacks for using bone substitutes

from the patient's iliac crest, including limited donor tissue, donor site illness and increased risk for infections or disease transmission, which highlights the importance of engineered implants [1,4]. Emerging tissue engineering strategies provide a remarkable opportunity for the regeneration of injured tissues through the fabrication of the artificial constructs [5,6]. Such structures must afford a suitable microenvironment for cell attachment and proliferation to stimulate the damaged tissue formation [7]. Furthermore, biocompatibility, biodegradability, and porosity of the structures directly affect their treatment performance [8]. Currently, different types of materials such as metals, polymers, and ceramics are used as biomedical implants [9]. The metallic implants such as stainless steel, cobalt, and titanium alloys are mainly exploited due to the excellent mechanical properties and superior corrosion resistance in orthopedic targets, while polymer and ceramic-based implants exhibit weak and brittle properties [10]. Among the different types of metallic implants, the surgical grade 316LSS is the most common bone-implant offering high mechanical properties, low cost, and availability [11]. Regarding the 316LSS properties, the biggest drawback is the release of the metal ions, e.g., iron, nickel, and chromium in the biological environment, making it pernicious in nature [12,13].

In order to overcome the aforementioned issue, several surface modification procedures have been applied. Based on the literature, the composite coatings method using polymers and ceramic components is considered as the most popular strategy for this purpose [14,15]. Poly (ϵ -caprolactone) (PCL) is a well-known synthetic polymer composed of semi-crystalline linear polyester, which is approved by the U.S. Food and Drug Administration (FDA) as a biomedical material [16]. Although PCL exhibits significant mechanical strength and biocompatibility, it is inherently hydrophobic which negatively affects its biological properties such as cell adhesion and proliferation [17,18]. Therefore, a combination of PCL with a natural hydrophilic polymer such as Ge was utilized as an ideal coating for bone regeneration [19–21]. Ge has been utilized widely in medical applications as a natural biopolymer derived from partial hydrolysis of collagen. In addition to its biocompatibility, low cost, availability the suitable hydrophilicity of Ge-based materials promote cell attachment and proliferation of the blends comprised of Ge [22].

Since rapid biodegradability and weak mechanical properties are considered as the key drawbacks of Ge, it is normally used for tissue engineering combined with artificial polymers such as PCL to fulfill the mechanical properties requirement [23,24]. Yao et al. [25] fabricated PCL/Ge nanofibrous scaffolds containing various polymer ratios for tissue engineering application. The essays of cellular behaviors indicated that the blend of PCL/Ge had higher adhesion and proliferation in comparison with pure PCL and Ge. Additionally, the PCL/Ge having the ratio of 2:1 showed the best cell spreading, viability and cytoskeleton organization. Fanaee et al. [26] prepared PCL/Ge nanofiber mats with a 70/30 weight ratio containing bioactive glass particles via electrospinning for bone tissue engineering application. The results of in vitro tests confirmed no considerable cytotoxicity as well as good cell adhesion for the prepared nanofibers comprised of PCL and Ge. Moreover, bioceramics are exploited to generate osteoconductive feature for these artificial constructs. Various types of bioceramics and bioglasses such as HA, alumina, zirconia, phosphates, and forsterite have been used to stimulate cell growth and/or bone cell formations by releasing active ions in cell microenvironment [27–31]. Recently, forsterite (Mg_2SiO_4) has been highly recommended as an osteoconductive biomaterial for use in bone regeneration applications, based on its remarkable mechanical properties and biocompatibility. It is worthwhile to note that forsterite enhances cell proliferation and bone regeneration by releasing Mg ion after implantation. Moreover, a higher degradation rate of forsterite composite scaffolds is reported because of its low degree of crystallinity [32,33].

GO is one of the most efficient derivatives of graphene, which has abundant hydroxyls, epoxides and carboxyl functional groups on its surface [34,35]. GO possesses many benefits such as solubility in water and some polar solvents, excellent biocompatibility, good mechanical properties, and high flexibility. It is also a potential biomaterial for cell proliferation enhancement because of its superior biocompatibility. GO nanosheets were incorporated into PCL nanofibers in order to investigate cell behavior of two types of cells such as mMSCs and PC12-L on the PCL/GO [36]. The results showed

that GO incorporation substantially improved the cell attachment, spreading and proliferation of the prepared scaffolds. Therefore, the shortcomings of 316LSS—which include releasing of ions such as nickel and chromium—can be addressed using these two materials to improve the biocompatibility and corrosion resistance of 316LSS.

In our previous research, a bilayer coating of GO and polymeric nanofibrous composite was prepared via electrophoretic deposition (EPD) and electrospinning, whereby the corrosion resistance of 316LSS significantly improved [37]. The central aim of this research is evaluating the cellular behavior of that nanocomposite and the bilayer coating. In other words, the effects of GO layer and forsterite concentration on the bioactivity of the nanofibers were assessed.

2. Materials and Methods

2.1. Surface and Coatings Preparation

The 316LSS substrate was cut into rectangular samples with a dimension of $2 \times 1 \times 0.4 \text{ cm}^3$. Before the EPD process, the samples were mechanically polished using SiC papers with 80, 120, 240 and 320 grit-size. Then, the samples were rinsed with deionized (DI) water and were sonicated in acetone to remove any remained grease on the surface of the samples followed by drying at room temperature.

To apply GO coating on the surface of the samples, firstly different amounts of GO nanopowder (Nanosany Corporation, Mashhad, Iran) were dispersed in DI water by ultra-sonication to obtain a homogenous suspension. To reach a uniform coating, different EPD variables such as voltage and deposition time were optimized as discussed in our previous study [37].

To perform the electrospinning process, solutions containing PCL (average Mw = 80,000, Sigma, St. Louis, MO, USA), gelatin (type B bovine skin, Mw = 50,000–100,000) with 1 and 3 weight percent of forsterite nanoparticles were prepared using formic acid and acetic acid (1:3 *v/v*) as solvents. In order to prepare the solvents, forsterite nanoparticles were first ultrasonically dispersed in adequate solvents. Afterward, the solutions were prepared by dissolving the PCL and gelatin in the solvents and magnetically stirred at room temperature for more than six hours. The solutions were then electrospun with a constant gap distance of 15 cm, applied voltage range of 12–26 kV, and feed rates of 0.1–0.5 mL/h.

2.2. Characterization of the Nanofibrous Layer

The morphology of the electrospun samples and distribution of the nanoparticles in the PCL/gelatin nanofibers were evaluated by FESEM (Quanta 450 FEG, Graz, Austria) and Energy Dispersive X-ray (EDS, Octane Elite EDS, Graz, Austria), respectively.

The porosity of the electrospun layer was determined based on the analysis of the nanofiber FESEM micrographs, utilizing image J software (Image J, National Institutes of Health, Bethesda, MD, USA). The surface area of pores (S_p) and the total surface area of the samples (S_t) were measured. Moreover, the porosity percent was calculated according to Equation (1) [38]:

$$\%P = \frac{S_p}{S_t} \times 100 \quad (1)$$

Brookfield DV-II viscometer (Middleboro, MA, USA) and JENWA 3540 conductivity meter (Burlington, NJ, USA) were used to measure the conductivity and viscosity of the electrospinning solutions, respectively. The viscosity was measured at 25 °C and the rotational speed of 6 rpm. Water contact angle measurements were carried out with a drop shape analyzer (Sessile Drop-G10, Tehran, Iran) to investigate the surface wettability and hydrophilicity of the GO layer and electrospun nanofibers.

The degradation rate of the samples was determined by measuring the weight loss of the samples based on ASTM-F1635 after 21 days of immersion in PBS at 37 °C and pH = 7.4. The weight loss percentage was calculated according to Equation (2). In the equation, the W_0 , W_t refer to the weights of the coated samples before and after immersion, respectively. In addition, W_s is the weight of the 316LSS substrate.

$$\% \text{Weight loss} = \frac{w_0 - w_t}{w_0 - w_s} \times 100 \quad (2)$$

Since the pH changes indicate the release of the alkaline ions and HA formation [39], the pH value of the solutions was measured during the soaking time using an electrolyte-type pH meter.

2.3. Bioactivity Investigations of the Coatings

The bioactivity of the coatings was investigated according to the amount of HA formed on the substrates after soaking in SBF. The SBF solution was prepared according to the Kokubo et al. method [40]. The substrates were immersed in SBF at 37 °C in a stable water bath for 21 days. X-ray diffraction (ASENWARE, AW-XDM 300, Shenzhen, China), using monochromatized CuK α radiation generated from 40 kV and 30 mA and ranging from 10° to 80°, was employed to confirm the crystalline phase of the formed HA on the coated substrates. The morphology of the HA was evaluated by FESEM images after 3, 7, 14 and 21 days soaking in the SBF.

2.4. In-vitro Cell Behavior of the Coatings

The MG-63 cells were cultured in Dulbecco's modified Eagle's medium (DMEM) complemented with 10% FBS (Gibco, Biosciences, Dublin, Ireland), 1% Glutamax, 1% penicillin/streptomycin and 1% Non-essential Amino Acid (NEAA). The seeded cells were incubated at 37 °C and carbon dioxide amount of 5%. The nanofibrous coatings were electrospun on circular disks based on previous work [41]. All the coatings were sterilized under UV over 15 min on each side, immersed in 70% ethanol for 12 h and then washed with amphotericin/gentamicin/penicillin and PBS for 15 min. After that, the electrospun coated substrates were placed in 24-well plates and MG-63 cells, at a density of 30,000 cells, were seeded on the surfaces of each sample. The cell morphology and adhesion on the seeded nanofibers were evaluated by FESEM images after 1 and 7 days of cell seeding. The cultured cells on the coatings were fixed by 2.5 v% glutaraldehyde solution (Sigma, St. Louis, MO, USA) in PBS and dehydrated through various concentrations of ethanol (0, 25, 50, 75 and 100 v%).

The MTS tests were also performed on the coatings after 1, 3, 5 and 7 days' cell seeding to evaluate the viability of the samples. The seeded samples were washed and placed in an incubator with 10% of MTS reagent under 37 °C and 5% carbon dioxide. After 3.5 h of incubation, the aliquots were transferred into a 96-well plate. Then, the absorbance of the samples at 429 nm was quantified using a spectrophotometric plate reader (Awareness Technology Inc., Palm City, FL, USA).

3. Results and Discussion

3.1. Characterization of the Electrospun Nanofibers

Figure 1 indicates the FESEM micrographs of the electrospun nanofibers. In addition, the viscosity and conductivity of the solutions along with the average fiber diameter of the electrospun nanofibers were measured and summarized in Tables 1 and 2, respectively. Table 2 reveals that the incorporation of 1 wt.% forsterite to the PCL/Ge composition decreased the fiber diameter from 167 to 148 nm. Increasing the forsterite content to 3 wt.% increased the average fiber diameter to 171 nm. The addition of the forsterite nanopowder increased the conductivity and the surface charge density of the solution, which caused the diameter reduction. On the other hand, the higher amount of forsterite had a dominant effect on the solution viscosity, leading to an increase in the nanofiber diameter. These results are in agreement with previous researches [42,43].

The morphology and the corresponding EDS analysis of the nanoparticles distribution in the PCL/Ge nanofibers are presented in Figure 2. It can be observed that the nanoparticles are uniformly distributed on the coatings. It can be also discerned that the dispersion of the nanoparticles in the nanofibers with 1 wt.% forsterite is better than the 3 wt.% loaded sample. The low amount of agglomeration in the PCL/Ge/forsterite-3 sample can be attributed to the strong surface energy among the nanoparticles [44].

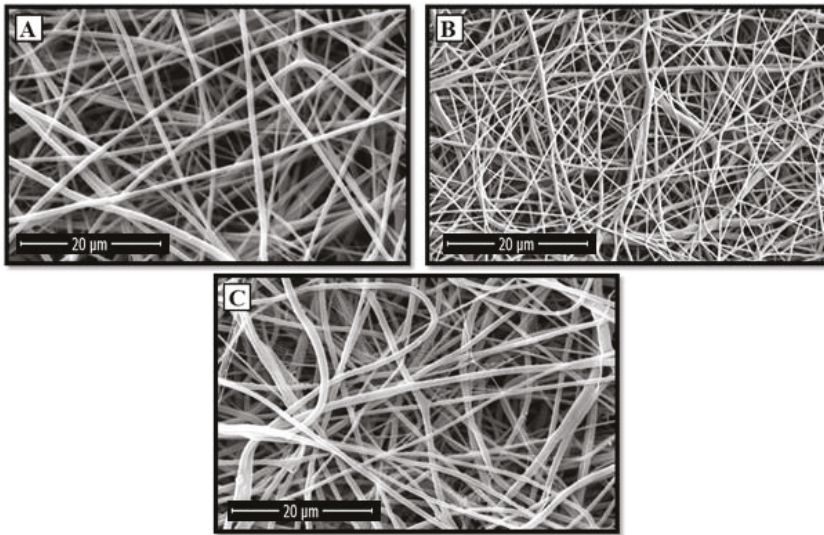


Figure 1. FESEM micrographs of the prepared PCL/Ge nanofibers containing (A) 0%, (B) 1%, and (C) 3 wt.% forsterite nanoparticles.

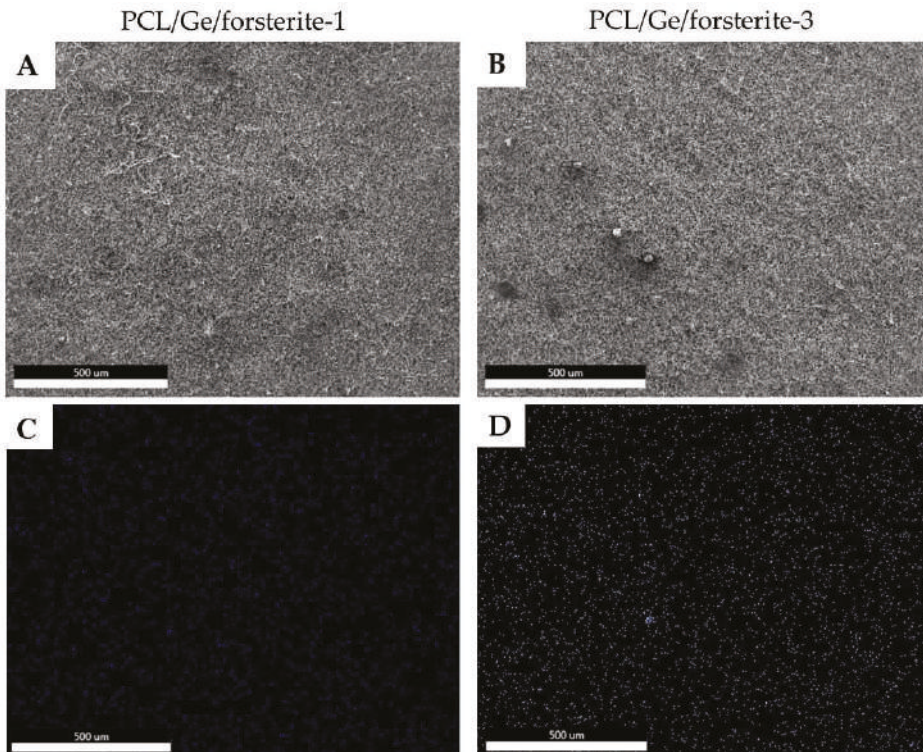


Figure 2. FESEM micrographs (A) and (B), and the distribution map of Mg element (C) and (D) of the electrospun PCL/Ge nanofibers with 1% and 3% forsterite nanoparticles.

Table 1. Physical properties of the solutions.

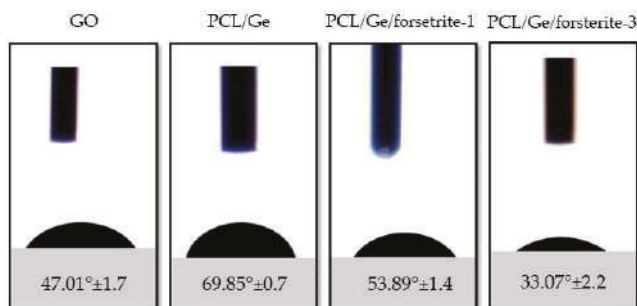
Nanofiber Composition	Viscosity (cP)	Conductivity ($\mu\text{S}/\text{cm}$)
PCL/Ge	910 \pm 32	271 \pm 13
PCL/Ge/forsterite-1	980 \pm 24	288 \pm 10
PCL/Ge/forsterite-3	1400 \pm 100	290 \pm 20

Table 2. Morphology characteristic of the electrospun scaffolds.

Nanofiber Composition	Fiber Diameter (nm)	Porosity (%)	Weight Loss (%)
PCL/Ge	167 \pm 29	77.4 \pm 0.2	12.0 \pm 0.2
PCL/Ge/forsterite-1	148 \pm 36	71.1 \pm 0.1	15.0 \pm 0.2
PCL/Ge/forsterite-3	171 \pm 43	82.6 \pm 0.2	17.9 \pm 0.1

Since the porosity influences the scaffold's cell adhesion and proliferation, it is essential to consider this scaffold characteristic during the tissue engineering [45]. It was reported that the porosity of the electrospun nanofibers are mostly controlled by the diameter of the nanofibers [46]. The porosity of the samples was measured based on the FESEM micrographs (Figure 1) and reported in Table 2. The porosity of the electrospun scaffolds was reduced by introducing 1 wt.% of nanoparticles and then increased at the nanoparticles content of 3 wt.%. Therefore, the effect of the amount of nanoparticles on the porosity was similar to the fiber diameter. The lowest porosity content was present in the coatings having thinner nanofibers. On the other hand, the highest porosity was assigned to the PCL/Ge/forsterite-3 nanofibers at 82.6% \pm 0.2%, which had a thicker fiber diameter. Generally, all of the samples illustrated porosity above 70%, which is apt for medical applications [47]. Therefore, it is anticipated that all of the electrospun mats would have a high potential for cell attachment and proliferation.

Figure 3 shows the obtained results of the wettability analysis by measuring the water contact angle for the PCL/Ge, PCL/Ge/forsterite-1 and PCL/Ge/forsterite-3 coatings. The relaxation time of the water droplet was 10 s. According to Sup Kim et al. [48], the contact angle of PCL was reported to be 120°, hence it is clear that the incorporation of gelatin increases the hydrophilicity of PCL nanofibers, which is due to the existence of amine and carboxylic groups in gelatin [49]. As can be seen in Figure 3, when the forsterite nanoparticles content increased from 1 to 3 wt.%, the water contact angle of the nanofibers decreased from 53.59° to 35.55°. Therefore, the hydrophilicity of the nanofibers is affected by the concentration of the nanoparticles. As a result, it is expected that cells would show higher extent adhesion on PCL/Ge/forsterite-3 nanofibers due to increased hydrophilicity.

**Figure 3.** The water contact angles of GO layer and PCL/Ge nanofibers containing 0, 1 and 3 wt.% forsterite.

The weight loss percentage of the samples was measured after 21 days' soaking in PBS at 37 °C and pH = 7.4. The results are summarized in Table 2. The weight loss of the PCL/Ge nanofibers increased from ca. 12% to ca. 18% by increasing the forsterite content from 0 to 3 wt.%. Therefore,

increasing the forsterite content increased the hydrophilicity, porosity and the weight loss of the scaffolds. The degradation of the coating can be associated not only with the hydrolysis of gelatin but also the diffusion of the nanoparticles from the surface of the nanofibrous coating to the solution [50]. Moreover, due to the highly crystalline phase of PCL, its weight loss is considered to be negligible [51].

The pH changes of the PBS solutions containing the scaffolds were assessed and depicted in Figure 4. It is clear that the pH values of the solution reduced from 7.4 to 6.9 in the PBS solution of the PCL/Ge nanofibers within 21 days. Releasing of acidic products from the degradation of the PCL and gelatin is responsible for the decrease in pH values [52]. In contrast to PCL/Ge, the amount of pH in the solution containing PCL/Ge/forsterite with 1 and 3 wt.% nanoparticles increased to 8.1 and 8.2, respectively, during the first week. The release of the Mg ions from forsterite incorporated into the scaffolds increased the alkalinity of the solution and consequently the pH value [52]. Moreover, the pH slightly decreased in the next week due to polymer degradation and remained constant.

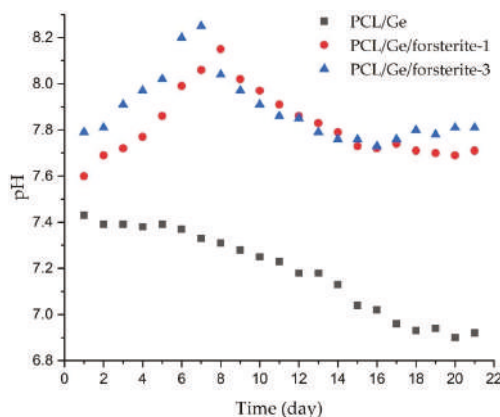


Figure 4. The pH values of the PBS solutions containing PCL/Ge with 0, 1 and 3 wt.% forsterite during 21 days immersion.

3.2. Bioactivity of the Electrospun Scaffolds

Osteoconductivity is a crucial characteristic of the implants utilized in bone tissue engineering applications to predict bone regeneration during implant employment [41]. The osteoconductivity of the electrospun nanofibers was evaluated by studying the capability of the coated samples in the creation of bone-like apatite. The PCL/Ge nanofibers containing various concentrations of the nanoparticle (1 and 3 wt.%) were soaked in SBF for 3, 7, 14 and 21 days. Figure 5 demonstrates the FESEM images of the PCL/Ge/forsterite with 1 and 3 wt.% after immersion in SBF. The bone-like apatite deposition was found to form on the surface of the resulting electrospun structure after three days in SBF and noticeably increased within 21 days. The presence of the nanoparticle in the scaffold structure led to the formation of the silanol ($-\text{Si}-\text{OH}$) groups, which contributed to Ca-P nucleation. As a result, the interaction of phosphate and carbonate groups in SBF and positively charged positions of the Ca-P nucleation caused phosphate layer formation during the immersion time [53]. From Figure 5, it can be seen that the HA formation on the electrospun structures having 3 wt.% of forsterite is significantly higher than the PCL/Ge/forsterite-1 structure, especially in three and seven days' immersion. Figure 6 presents the WAXS profiles of the samples PCL/Ge/forsterite-1 and PCL/Ge/forsterite-3 after 21 days soaking in SBF. From the diffractograms, the peaks at 2θ of 21.4° and 23.8° can be ascribed to the existence of PCL in the structure [26]. In addition, the peaks at 26.7° , 31.7° , 43.6° , 45.5° , 50.7° , and 74.6° can be related to the created HA on the electrospun substrates containing nanoparticles. The observed peaks for HA were also reported for HA in previous works [14,54]. The XRD patterns also confirm the formation of HA after 21 days' incubation of samples in SBF.

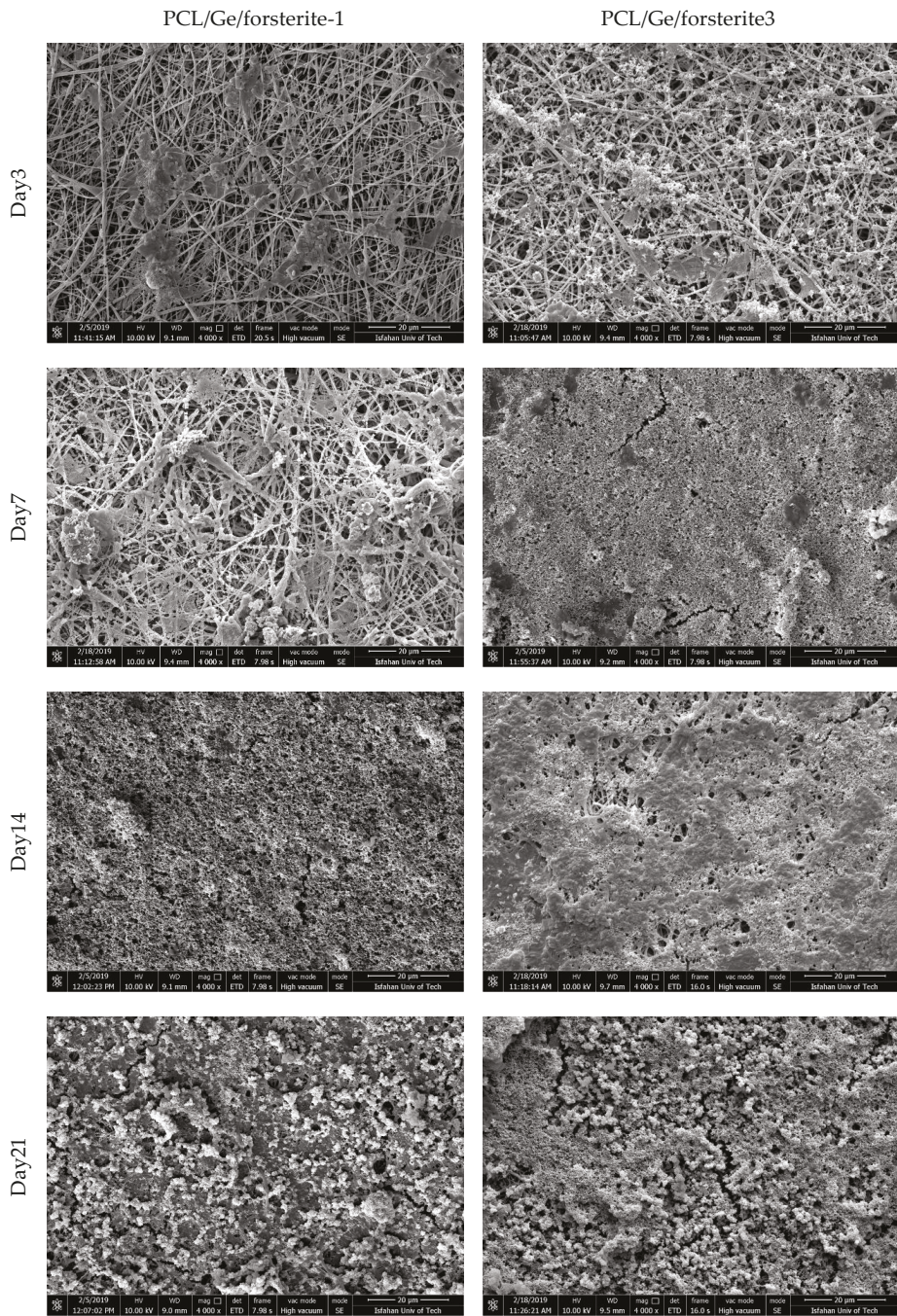


Figure 5. FESEM micrographs of the PCL/Ge/forsterite with 1 and 3 wt.% after 3, 7, 14, and 21 days immersion in the SBF solution.

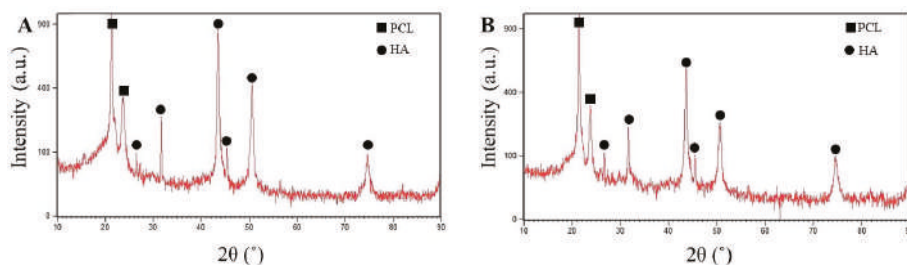


Figure 6. XRD patterns of PCL/Ge nanofibers containing (A) 1 and (B) 3% of forsterite after 21 days of immersion in SBF.

3.3. Cell Culture Studies

Cell attachment and proliferation are the results of efficient cell-material interactions [55]. The cell morphology on the PCL/Ge and GO-PCL/Ge electrospun structures containing 1 and 3 wt.% forsterite nanoparticles after one and seven days of MG-63 cells seeding is shown in Figure 7. It can be observed that the cells were well attached and spread on all the samples due to the proper interactions between the cells and the coatings. Specific cellular adhesion and well-spread morphology were higher for the GO-PCL/Ge structure rather than PCL/Ge after seven days. The better performance of the bilayer structure can be attributed to the presence of GO layer (with OH and COOH groups on the surface) and high hydrophilicity of the coatings. The existence of the surface roughness, as the intrinsic property of GO [36], and GO functional groups assisted the serum protein adsorption as well as cell attachment [56]. Additionally, the cells showed better growth on the structures containing a higher amount of the nanoparticles. The MTS results are illustrated in Figure 8 where the progressive growth of the cells confirms the non-cytotoxicity of the coatings [57]. All the bilayer structures with various amounts of the nanoparticles showed effective compatibility and interactions with the cells. The GO-PCL/Ge with 3 wt.% nanoparticles showed a noticeably higher cell viability in comparison with other nanostructures. The higher hydrophilicity of the coatings in the presence of the GO layer and the larger amount of the nanoparticles increased the cell viability. Besides, adsorption of the serum protein is affected by surface oxygen-containing groups of GO as its intrinsic feature [58]. Another reasonable explanation for the good cell growth is the conductivity of GO having oxygenated groups on its structure. Although GO is a poor conductor compared to graphene, it has higher conductivity than PCL/Ge nanofibrous layer [59].

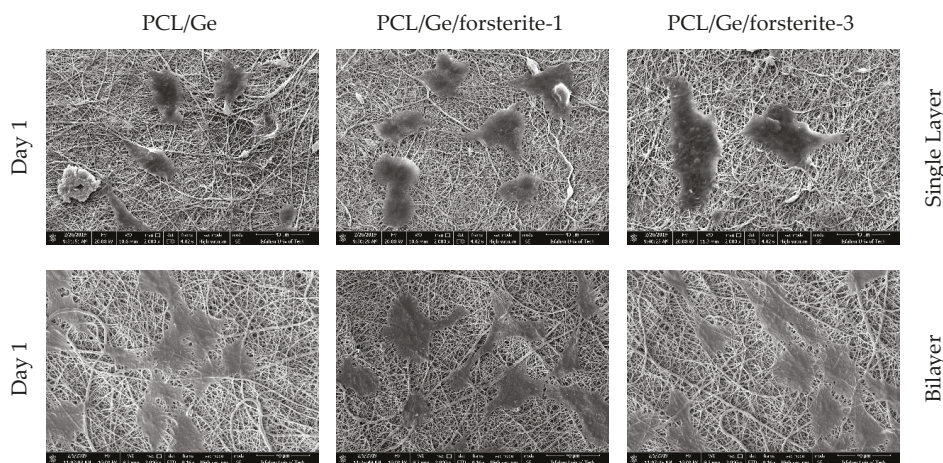


Figure 7. Cont.

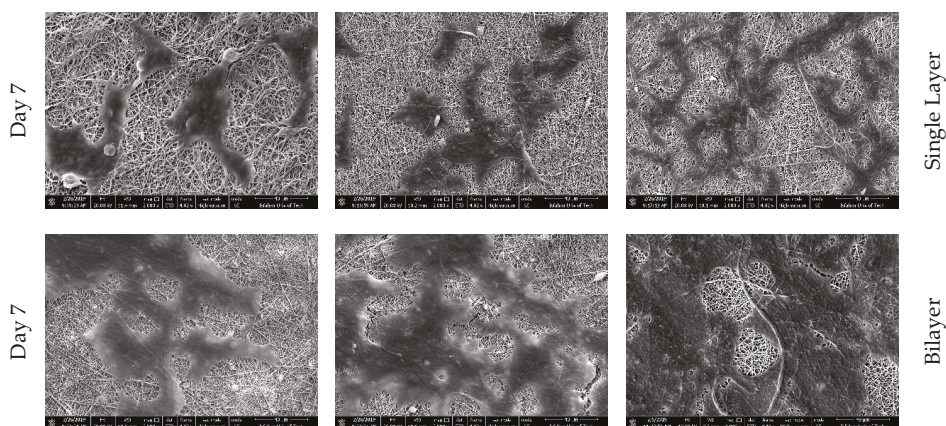


Figure 7. Morphology of the MG-63 cells on PCL/Ge/forsterite nanofibers with 1 and 3 wt.% and GO-PCL/Ge/forsterite with 1 and 3 wt.% after one and seven days of cell culture.

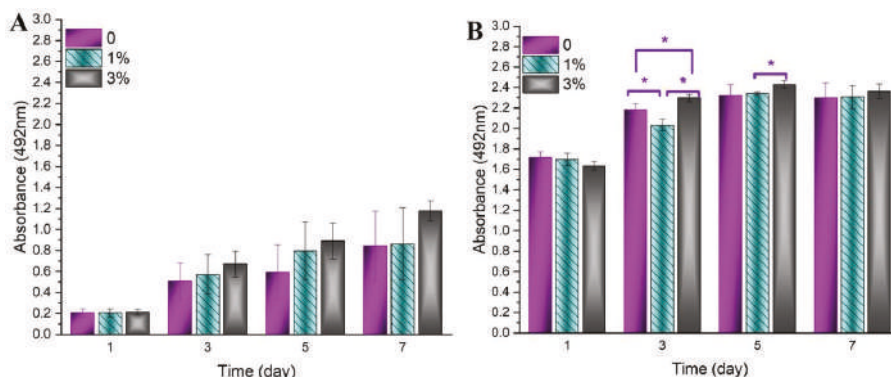


Figure 8. The MTS results of PCL/Ge structures containing 0, 1 and 3 wt.% forsterite nanoparticles, (A) without the GO layer and (B) with the GO layer (*significant difference at $p_{value} < 0.05$).

4. Conclusions

To recapitulate, a bilayer bioactive coating containing GO layer and nanofibrous PCL/Ge/forsterite was applied on 316LSS to develop a potential platform for bone implant application.

- Characterization of the nanofiber layer revealed the formation of a uniform beadless nanofibrous layer on the surface of the GO layer. It was also indicated that the forsterite nanoparticles were well-distributed on the top layer. The presence of gelatin and forsterite nanoparticles increased the wettability and biodegradation rate of the top layer (electrospun nanofibrous layer) which marks a development in bilayer coating in bone implant applications.
- The bioactivity results indicated the formation of HA on the surface of the nanofiber structures which was subsequently confirmed by XRD. the incorporation of the forsterite nanoparticles increased the bioactivity of the samples, especially after 14 and 21 days of soaking in the SBF solution.
- The PCL/Ge/forsterite and GO-PCL/Ge/forsterite coatings were found to be non-cytotoxic structures with an ability to enhance cell attachment and proliferation. Furthermore, the enhanced adhesion and growth of MG63 cells on bilayer coatings in comparison with nanocomposite coatings revealed the beneficial biocompatibility and hydrophilicity of GO due to functional groups on its surface as well as high surface roughness.

Author Contributions: Methodology, F.K., S.K., R.E.N., E.R.G., and F.E.; validation, F.K., S.K., R.E.N., E.R.G., F.E., and O.D.; formal analysis, F.K., S.N.K., S.K., R.E.N., E.R.G., F.E., and M.H.N.-E.; investigation, F.K., S.K., R.E.N., E.R.G., and F.E.; data curation, F.K., S.K., R.E.N., E.R.G., O.D., writing—original draft preparation, F.K., S.K., R.E.N., E.R.G., and F.E.; writing—review and editing, F.K., S.N.K., S.K., R.E.N., E.R.G., F.E., O.D. and M.H.N.-E.; supervision, S.N.K., and M.H.N.-E. All authors have read and agreed to the published version of the manuscript.

Funding: This research received no external funding.

Conflicts of Interest: The authors declare no conflict of interest. The funders had no role in the design of the study; in the collection, analyses, or interpretation of data; in the writing of the manuscript, or in the decision to publish the results.

References

- De Witte, T.-M.; Fratila-Apachitei, L.E.; Zadpoor, A.A.; Peppas, N.A. Bone tissue engineering via growth factor delivery: From scaffolds to complex matrices. *Regen. Biomater.* **2018**, *5*, 197–211. [[CrossRef](#)] [[PubMed](#)]
- Habibovic, P. Strategic Directions in Osteoinduction and Biomimetics. *Tissue Eng. Part A* **2017**, *23*, 1295–1296. [[CrossRef](#)] [[PubMed](#)]
- Ricciardi, B.F.; Bostrom, M.P. Bone graft substitutes: Claims and credibility. *Semin. Arthroplast.* **2013**, *24*, 119–123. [[CrossRef](#)]
- Burg, K.J.L.; Porter, S.; Kellam, J.F. Biomaterial developments for bone tissue engineering. *Biomaterials* **2000**, *21*, 2347–2359. [[CrossRef](#)]
- Rezwani, K.; Chen, Q.Z.; Blaker, J.J.; Boccacini, A.R. Biodegradable and bioactive porous polymer/inorganic composite scaffolds for bone tissue engineering. *Biomaterials* **2006**, *27*, 3413–3431. [[CrossRef](#)]
- Esmaeely Neisiany, R.; Enayati, M.S.; Sajkiewicz, P.; Pahlevanneshan, Z.; Ramakrishna, S. Insight into the Current Directions in Functionalized Nanocomposite Hydrogels. *Front. Mater.* **2020**, *7*, 25. [[CrossRef](#)]
- Bose, S.; Vahabzadeh, S.; Bandyopadhyay, A. Bone tissue engineering using 3D printing. *Mater. Today* **2013**, *16*, 496–504. [[CrossRef](#)]
- Loh, Q.L.; Choong, C. Three-Dimensional Scaffolds for Tissue Engineering Applications: Role of Porosity and Pore Size. *Tissue Eng. Part B Rev.* **2013**, *19*, 485–502. [[CrossRef](#)]
- Meinert, K.; Uerpmann, C.; Matschullat, J.; Wolf, G.K. Corrosion and leaching of silver doped ceramic IBAD coatings on SS 316L under simulated physiological conditions. *Surf. Coat. Technol.* **1998**, *103–104*, 58–65. [[CrossRef](#)]
- Sivaraj, D.; Vijayalakshmi, K. Novel synthesis of bioactive hydroxyapatite/f-multiwalled carbon nanotube composite coating on 316L SS implant for substantial corrosion resistance and antibacterial activity. *J. Alloys Compd.* **2019**, *777*, 1340–1346. [[CrossRef](#)]
- Yao, H.; Li, J.; Li, N.; Wang, K.; Li, X.; Wang, J. Surface Modification of Cardiovascular Stent Material 316L SS with Estradiol-Loaded Poly (trimethylene carbonate) Film for Better Biocompatibility. *Polymers* **2017**, *9*, 598. [[CrossRef](#)] [[PubMed](#)]
- Gopi, D.; Prakash, V.C.A.; Kavitha, L. Evaluation of hydroxyapatite coatings on borate passivated 316L SS in Ringer's solution. *Mater. Sci. Eng. C* **2009**, *29*, 955–958. [[CrossRef](#)]
- González, M.B.; Saidman, S.B. Electrodeposition of polypyrrole on 316L stainless steel for corrosion prevention. *Corros. Sci.* **2011**, *53*, 276–282. [[CrossRef](#)]
- Madhan Kumar, A.; Rajendran, N. Electrochemical aspects and in vitro biocompatibility of polypyrrole/TiO₂ ceramic nanocomposite coatings on 316L SS for orthopedic implants. *Ceram. Int.* **2013**, *39*, 5639–5650. [[CrossRef](#)]
- Chang, S.-H.; Hsiao, Y.-C. Surface and Protein Adsorption Properties of 316L Stainless Steel Modified with Polycaprolactone Film. *Polymers* **2017**, *9*, 545. [[CrossRef](#)]
- Ghasemi-Mobarakeh, L.; Prabhakaran, M.P.; Morshed, M.; Nasr-Esfahani, M.-H.; Ramakrishna, S. Electrospun poly(ϵ -caprolactone)/gelatin nanofibrous scaffolds for nerve tissue engineering. *Biomaterials* **2008**, *29*, 4532–4539. [[CrossRef](#)]
- Gautam, S.; Dinda, A.K.; Mishra, N.C. Fabrication and characterization of PCL/gelatin composite nanofibrous scaffold for tissue engineering applications by electrospinning method. *Mater. Sci. Eng. C* **2013**, *33*, 1228–1235. [[CrossRef](#)]
- Ren, K.; Wang, Y.; Sun, T.; Yue, W.; Zhang, H. Electrospun PCL/gelatin composite nanofiber structures for effective guided bone regeneration membranes. *Mater. Sci. Eng. C* **2017**, *78*, 324–332. [[CrossRef](#)]
- Rajzer, I.; Menaszek, E.; Kwiatkowski, R.; Planell, J.A.; Castano, O. Electrospun gelatin/poly(ϵ -caprolactone) fibrous scaffold modified with calcium phosphate for bone tissue engineering. *Mater. Sci. Eng. C* **2014**, *44*, 183–190. [[CrossRef](#)]

20. Lee, J.-h.; Lee, Y.J.; Cho, H.-j.; Kim, D.W.; Shin, H. The incorporation of bFGF mediated by heparin into PCL/gelatin composite fiber meshes for guided bone regeneration. *Drug Deliv. Transl. Res.* **2015**, *5*, 146–159. [[CrossRef](#)]
21. Cirillo, V.; Guarino, V.; Ambrosio, L. Design of Bioactive Electrospun Scaffolds for Bone Tissue Engineering. *J. Appl. Biomater. Funct. Mater.* **2012**, *10*, 223–228. [[CrossRef](#)] [[PubMed](#)]
22. Rezvani Ghomi, E.; Khalili, S.; Nouri Khorasani, S.; Esmaeely Neisiany, R.; Ramakrishna, S. Wound dressings: Current advances and future directions. *J. Appl. Polym. Sci.* **2019**, *136*, 47738. [[CrossRef](#)]
23. Chong, E.J.; Phan, T.T.; Lim, I.J.; Zhang, Y.Z.; Bay, B.H.; Ramakrishna, S.; Lim, C.T. Evaluation of electrospun PCL/gelatin nanofibrous scaffold for wound healing and layered dermal reconstitution. *Acta Biomater.* **2007**, *3*, 321–330. [[CrossRef](#)] [[PubMed](#)]
24. Khalili, S.; Khorasani, S.N.; Neisiany, R.E.; Ramakrishna, S. Theoretical cross-link density of the nanofibrous scaffolds. *Mater. Des. Process. Commun.* **2019**, *1*, e22. [[CrossRef](#)]
25. Yao, R.; He, J.; Meng, G.; Jiang, B.; Wu, F. Electrospun PCL/Gelatin composite fibrous scaffolds: Mechanical properties and cellular responses. *J. Biomater. Sci. Polym. Ed.* **2016**, *27*, 824–838. [[CrossRef](#)]
26. Fanaee, S.; Labbaf, S.; Enayati, M.H.; Baharlou Houreh, A.; Esfahani, M.-H.N. Creation of a unique architectural structure of bioactive glass sub-micron particles incorporated in a polycaprolactone/gelatin fibrous mat; characterization, bioactivity, and cellular evaluations. *J. Biomed. Mater. Res. Part A* **2019**, *107*, 1358–1365. [[CrossRef](#)] [[PubMed](#)]
27. Pang, X.; Zhitomirsky, I. Electrophoretic deposition of composite hydroxyapatite-chitosan coatings. *Mater. Charact.* **2007**, *58*, 339–348. [[CrossRef](#)]
28. Kheirkhah, M.; Fathi, M.; Salimijazi, H.R.; Razavi, M. Surface modification of stainless steel implants using nanostructured forsterite (Mg₂SiO₄) coating for biomaterial applications. *Surf. Coat. Technol.* **2015**, *276*, 580–586. [[CrossRef](#)]
29. Vallet-Regí, M.; Salinas, A.J. 6—Ceramics as bone repair materials. In *Bone Repair Biomaterials*, 2nd ed.; Pawelec, K.M., Planell, J.A., Eds.; Woodhead Publishing: Sawston, UK; Cambridge, UK, 2019; pp. 141–178. [[CrossRef](#)]
30. Enayati, M.S.; Neisiany, R.E.; Sajkiewicz, P.; Behzad, T.; Denis, P.; Pierini, F. Effect of nanofiller incorporation on thermomechanical and toughness of poly (vinyl alcohol)-based electrospun nanofibrous bionanocomposites. *Theor. Appl. Fract. Mech.* **2019**, *99*, 44–50. [[CrossRef](#)]
31. Kouhi, M.; Jayarama Reddy, V.; Fathi, M.; Shamanian, M.; Valipouri, A.; Ramakrishna, S. Poly (3-hydroxybutyrate-co-3-hydroxyvalerate)/fibrinogen/bredigite nanofibrous membranes and their integration with osteoblasts for guided bone regeneration. *J. Biomed. Mater. Res. Part A* **2019**, *107*, 1154–1165. [[CrossRef](#)]
32. Devi, K.B.; Tripathy, B.; Roy, A.; Lee, B.; Kumta, P.N.; Nandi, S.K.; Roy, M. In Vitro Biodegradation and In Vivo Biocompatibility of Forsterite Bio-Ceramics: Effects of Strontium Substitution. *ACS Biomater. Sci. Eng.* **2019**, *5*, 530–543. [[CrossRef](#)]
33. Tavangarian, F.; Emadi, R. Improving degradation rate and apatite formation ability of nanostructure forsterite. *Ceram. Int.* **2011**, *37*, 2275–2280. [[CrossRef](#)]
34. Dreyer, D.R.; Park, S.; Bielawski, C.W.; Ruoff, R.S. The chemistry of graphene oxide. *Chem. Soc. Rev.* **2010**, *39*, 228–240. [[CrossRef](#)] [[PubMed](#)]
35. Cobos, M.; De-La-Pinta, I.; Quindós, G.; Fernández, J.M.; Fernández, D.M. Synthesis, Physical, Mechanical and Antibacterial Properties of Nanocomposites Based on Poly(vinyl alcohol)/Graphene Oxide–Silver Nanoparticles. *Polymers* **2020**, *12*, 723. [[CrossRef](#)] [[PubMed](#)]
36. Song, J.; Gao, H.; Zhu, G.; Cao, X.; Shi, X.; Wang, Y. The preparation and characterization of polycaprolactone/graphene oxide biocomposite nanofiber scaffolds and their application for directing cell behaviors. *Carbon* **2015**, *95*, 1039–1050. [[CrossRef](#)]
37. Khosravi, F.; Nouri Khorasani, S.; Rezvani Ghomi, E.; Kichi, M.K.; Zilouei, H.; Farhadian, M.; Esmaeely Neisiany, R. A bilayer GO/nanofibrous biocomposite coating to enhance 316L stainless steel corrosion performance. *Mater. Res. Exp.* **2019**, *6*, 086470. [[CrossRef](#)]
38. Grove, C.; Jerram, D.A. jPOR: An ImageJ macro to quantify total optical porosity from blue-stained thin sections. *Comput. Geosci.* **2011**, *37*, 1850–1859. [[CrossRef](#)]
39. Diba, M.; Kharaziha, M.; Fathi, M.H.; Gholipourmalekabadi, M.; Samadikuchaksaraei, A. Preparation and characterization of polycaprolactone/forsterite nanocomposite porous scaffolds designed for bone tissue regeneration. *Compos. Sci. Technol.* **2012**, *72*, 716–723. [[CrossRef](#)]

40. Kokubo, T.; Takadama, H. How useful is SBF in predicting in vivo bone bioactivity? *Biomaterials* **2006**, *27*, 2907–2915. [[CrossRef](#)]
41. Masoudi Rad, M.; Nouri Khorasani, S.; Ghasemi-Mobarakeh, L.; Prabhakaran, M.P.; Foroughi, M.R.; Kharaziha, M.; Saadatkish, N.; Ramakrishna, S. Fabrication and characterization of two-layered nanofibrous membrane for guided bone and tissue regeneration application. *Mater. Sci. Eng. C* **2017**, *80*, 75–87. [[CrossRef](#)]
42. Haider, A.; Haider, S.; Kang, I.-K. A comprehensive review summarizing the effect of electrospinning parameters and potential applications of nanofibers in biomedical and biotechnology. *Arab. J. Chem.* **2018**, *11*, 1165–1188. [[CrossRef](#)]
43. Sharifi, A.; Khorasani, S.N.; Borhani, S.; Neisiany, R.E. Alumina reinforced nanofibers used for exceeding improvement in mechanical properties of the laminated carbon/epoxy composite. *Theor. Appl. Fract. Mech.* **2018**, *96*, 193–201. [[CrossRef](#)]
44. Shi, H.; Liu, F.; Yang, L.; Han, E. Characterization of protective performance of epoxy reinforced with nanometer-sized TiO₂ and SiO₂. *Prog. Org. Coat.* **2008**, *62*, 359–368. [[CrossRef](#)]
45. Madhan Kumar, A.; Nagarajan, S.; Ramakrishna, S.; Sudhagar, P.; Kang, Y.S.; Kim, H.; Gasem, Z.M.; Rajendran, N. Electrochemical and in vitro bioactivity of polypyrrole/ceramic nanocomposite coatings on 316L SS bio-implants. *Mater. Sci. Eng. C* **2014**, *43*, 76–85. [[CrossRef](#)] [[PubMed](#)]
46. Neisiany, R.E.; Enayati, M.S.; Kazemi-Beydokhti, A.; Das, O.; Ramakrishna, S. Multilayered Bio-Based Electrospun Membranes: A Potential Porous Media for Filtration Applications. *Front. Mater.* **2020**, *7*, 67. [[CrossRef](#)]
47. Meng, Z.X.; Wang, Y.S.; Ma, C.; Zheng, W.; Li, L.; Zheng, Y.F. Electrospinning of PLGA/gelatin randomly-oriented and aligned nanofibers as potential scaffold in tissue engineering. *Mater. Sci. Eng. C* **2010**, *30*, 1204–1210. [[CrossRef](#)]
48. Kim, M.S.; Jun, I.; Shin, Y.M.; Jang, W.; Kim, S.I.; Shin, H. The Development of Genipin-Crosslinked Poly(caprolactone) (PCL)/Gelatin Nanofibers for Tissue Engineering Applications. *Macromol. Biosci.* **2010**, *10*, 91–100. [[CrossRef](#)]
49. Xue, J.; He, M.; Liang, Y.; Crawford, A.; Coates, P.; Chen, D.; Shi, R.; Zhang, L. Fabrication and evaluation of electrospun PCL–gelatin micro-/nanofiber membranes for anti-infective GTR implants. *J. Mater. Chem. B* **2014**, *2*, 6867–6877. [[CrossRef](#)]
50. Nie, L.; Wu, Q.; Long, H.; Hu, K.; Li, P.; Wang, C.; Sun, M.; Dong, J.; Wei, X.; Suo, J.; et al. Development of chitosan/gelatin hydrogels incorporation of biphasic calcium phosphate nanoparticles for bone tissue engineering. *J. Biomater. Sci. Polym. Ed.* **2019**, *30*, 1636–1657. [[CrossRef](#)]
51. Bartnikowski, M.; Dargaville, T.R.; Ivanovski, S.; Hutmacher, D.W. Degradation mechanisms of polycaprolactone in the context of chemistry, geometry and environment. *Prog. Polym. Sci.* **2019**, *96*, 1–20. [[CrossRef](#)]
52. Kharaziha, M.; Fathi, M.H.; Edris, H. Development of novel aligned nanofibrous composite membranes for guided bone regeneration. *J. Mech. Behav. Biomed. Mater.* **2013**, *24*, 9–20. [[CrossRef](#)] [[PubMed](#)]
53. Jokar, M.; Darvishi, S.; Torkaman, R.; Kharaziha, M.; Karbasi, M. Corrosion and bioactivity evaluation of nanocomposite PCL–forsterite coating applied on 316L stainless steel. *Surf. Coat. Technol.* **2016**, *307*, 324–331. [[CrossRef](#)]
54. Bavva Devi, K.; Singh, K.; Rajendran, N. Sol–gel synthesis and characterisation of nanoporous zirconium titanate coated on 316L SS for biomedical applications. *J. Sol-Gel Sci. Technol.* **2011**, *59*, 513. [[CrossRef](#)]
55. Kumbar, S.G.; Nukavarapu, S.P.; James, R.; Nair, L.S.; Laurencin, C.T. Electrospun poly(lactic acid-co-glycolic acid) scaffolds for skin tissue engineering. *Biomaterials* **2008**, *29*, 4100–4107. [[CrossRef](#)]
56. Yang, J.; Wan, Y.; Tu, C.; Cai, Q.; Bei, J.; Wang, S. Enhancing the cell affinity of macroporous poly(L-lactide) cell scaffold by a convenient surface modification method. *Polym. Int.* **2003**, *52*, 1892–1899. [[CrossRef](#)]
57. Mahlooji, E.; Atapour, M.; Labbaf, S. Electrophoretic deposition of Bioactive glass—Chitosan nanocomposite coatings on Ti-6Al-4V for orthopedic applications. *Carbohydr. Polym.* **2019**, *226*, 115299. [[CrossRef](#)]
58. Ku, S.H.; Park, C.B. Myoblast differentiation on graphene oxide. *Biomaterials* **2013**, *34*, 2017–2023. [[CrossRef](#)]
59. Ryu, S.; Kim, B.-S. Culture of neural cells and stem cells on graphene. *Tissue Eng. Regen. Med.* **2013**, *10*, 39–46. [[CrossRef](#)]



Article

Performance of Straw/Linear Low Density Polyethylene Composite Prepared with Film-Roll Hot Pressing

Lei Zhang, Huicheng Xu and Weihong Wang *

Key Lab of Bio-based Material Science and Technology (Ministry of Education), College of Material Science and Engineering, Northeast Forestry University, Harbin 150040, China; zl857910712@163.com (L.Z.); Hynnner@163.com (H.X.)

* Correspondence: weihongwang2001@nefu.edu.cn; Tel.: +86-451-8219-0932

Received: 18 December 2019; Accepted: 17 March 2020; Published: 9 April 2020

Abstract: Thermoplastic composites are usually prepared with the extrusion method, and straw reinforcement material must be processed to fiber or powder. In this study, film-roll hot pressing was developed to reinforce linear low density polyethylene (LLDPE) with long continuous straw stems. The long straw stems were wrapped with LLDPE film and then hot pressed and cooled to prepare straw/LLDPE composite. Extruded straw fiber/LLDPE composite was prepared as a control. The mechanical properties of these LLDPE-based composites were evaluated. The hot pressed straw/LLDPE composite provided higher tensile strength, tensile modulus, flexural strength, flexural modulus, and impact strength than the traditional extruded straw/LLDPE composite, by 335%, 107%, 68%, 57%, and 181%, respectively, reaching 35.1 MPa, 2.65 GPa, 3.8 MPa, 2.15 GPa, and 25.1 KJ/m². The density of the hot pressed straw/LLDPE composite (0.83 g/cm³) was lower than that of the extruded straw/LLDPE composite (1.31 g/cm³), and the former had a higher ratio of strength-to-weight. Scanning electron microscopy indicated that the orientation of the straws in the composite was better with the new method. Differential scanning calorimetry tests revealed that in hot pressed straw/LLDPE composite, straw fibers have a greater resistance to the melting of LLDPE than extruded composite. Rotary rheometer tests showed that the storage modulus of the hot pressed straw/LLDPE was less affected by frequency than that of the extruded composite, and the better elastic characteristics were pronounced at 150 °C. The hot pressed straw/LLDPE composite absorbed more water than the extruded composite and showed a potential ability to regulate the surrounding relative humidity. Our results showed that straw from renewable sources can be used to produce composites with good performance.

Keywords: bio-composite; linear low density polyethylene; performance; straws

1. Introduction

Natural fiber reinforced composite is a kind of biomass composite. It uses plant-based natural fibers (such as straw, bamboo, jute, and sisal, etc.) as reinforcement, polymers such as polyethylene (PE) and polypropylene (PP) as the matrix, prepared by blending extrusion or molding [1,2]. Natural fiber reinforced composites are widely used in automotive interiors, panel or wall panels, and sports equipment because of their low cost, safety, non-toxicity, renewability, wide source and excellent performance [3,4].

Straw is a type of renewable, abundant natural fiber. The world's crops can provide approximately two billion tons of straw per year [5]. In the past, the main disposal method of straw was incineration, but given the serious associated environmental problems and increasing environmental awareness, straw recycling has become an international priority [6].

Researchers have made some achievements in straw fiber reinforced composites. Nyambo et al. [7] used maleic acid-grafted polyurethane (PU-g-MA) to improve the interfacial adhesion between wheat straw and polyurethane (PU). They found that the addition of 3 phr and 5 phr PU-g-MA significantly increased the tensile strength (20%) and flexural strength (14%) of straw/PU composites, and proved that the increase in strength was due to the well combination of fibers and matrix. Xiao et al. [8] treated the straw with NaOH solution, blended the straw, polyethylene, stearic acid and maleic anhydride, then hot pressed to manufacture the straw/PP composite. The composite has low water absorption and good acid and alkali resistance; Zhang et al. [9] investigated the effects of different straw treatment methods, the particle size of straw powder, and the mass fraction of straw on the mechanical properties of straw/PP composites. The results show that when the straw is treated with the silane coupling agent KH570, the mechanical properties of the straw/PP composite are the best when the particle size of the straw powder is 60 mesh and the mass fraction is 50%; Zabihzadeh et al. [10] investigated the effect of maleic acid grafted polyethylene on the mechanical properties of straw/high density polyethylene (HDPE) composites. It was found that compared with no addition, adding 2% MAPE can increase the tensile strength of the composite by 43%, increase the tensile modulus by 116%, and increase the impact strength by 12%. Even with the addition of 1%, there is a clear improvement.

Straw fiber reinforced composites are a branch of Wood Plastic Composites (WPC). The extrusion molding process, one of the main molding processes of WPC, refers to a processing method in which natural fiber powder, thermoplastic, and various additives are melted in a high temperature, high pressure extruder to be fully mixed, plasticized, finally passed through the top mold of the machine continuously. Due to its advantages of continuous production and high production efficiency, extrusion molding is widely used in industrial production. As of 2017, China's WPC output was close to three million tons, accounting for two-thirds of the world's total output, and the China's production, consumption and exports ranked first in the world, which is precisely due to the development and improvement of extrusion molding processes over the years. The extrusion molding process is mainly divided into one-step extrusion and two-step extrusion. In two-step molding process, the raw materials are first pelletized in a twin-screw extruder, then extruded in single-screw extruder to prepare the composite, and the one-step process skips the pelletizing stage. The two-step process is simpler, flexible, and easy to adjust, which is the most commonly used molding process for enterprises and research units. However, the extrusion molding is easily affected by many factors due to the complicated process. The combined effect of many factors caused many uncertainties among the variables [11].

In extrusion molding process, straw is mostly used in form of short fiber or powder in composite structures. The interface bonding conditions of long fiber reinforced composites are very different from that of short fiber reinforced composites [12]. For example, the friction at the fiber/plastic interface of the former is much larger than that of the latter [13]. The stem of the straw itself has good tensile strength. Nevertheless, this strength often decreases when the straw is used in powder form. We know that orienting short fibers and powders is difficult. Therefore, owing to long straw integrity, long straw reinforced composites should theoretically have high strength. In addition, polypropylene (PP) and high density polyethylene are commonly used as matrixes because of their high strength and suitable processing temperatures [14,15], but the toughness of HDPE and PP-based composites is poor [16]. Therefore, other matrix options must be developed. Linear low density polyethylene (LLDPE) has excellent properties, such as tear strength and environmental stress crack resistance, in addition to the properties of general polyolefins [17]. LLDPE has a disadvantage of poor stiffness besides, it potentially could be remedied by straws.

The main aim of this study is to develop a novel method to prepare long straw stem reinforced LLDPE composites, whose properties are compared with those of short fiber reinforced LLDPE composites.

2. Materials and Methods

2.1. Materials

Straws were obtained from the suburb of Harbin, China. LLDPE film (Film, 10H01) and LLDPE particles (Hytrel, 22402) were purchased from Runwen Packaging Materials Co., Ltd., Shanghai, China. Talcum powder (2000 mesh) was produced by Liangjiang Titanium Chemical Products Co., LTD, Shanghai, China, and was used to enhance the stiffness of straw-plastic composite. Maleic anhydride grafted polyethylene (MAPE) with a grafting rate of 0.9% was purchased from Rizhisheng Fine Chemical Co., Ltd., Nantong, China, and was used as the coupling agent. PE wax, also from Shanghai Liangjiang Titanium Chemical Co., Ltd. and zinc stearate, purchased from Natural Oil Chemical Co., Ltd., Pasir Gudang Town, Johor Bahru, Malaysia, were used as lubricants.

2.2. Preparation of Straw/LLDPE Composite

The straw was first oven dried at 103 °C in a DHG-9140A drier (Yiheng Scientific Instrument Co., Ltd., Shanghai, China) to decrease its moisture content to below 3%. Then the straw was used to prepare composite through two molding processes.

2.2.1. Extrusion Molding

Dry straws were cut to 1 cm lengths. Then the short straws, LLDPE particles, talcum, MAPE, PE wax and zinc stearate were weighed in a ratio of 60:25:10:3:1:1. These materials were mixed in a SHR-10A high-speed mixer (Tonghe Rubber & Plastic Machinery Co., Ltd., Zhangjiagang, China) for 5 min. The mixture was pelleted in a JSH30 twin-screw extruder (Nanjing Rubber & Plastic Machinery Factory in Nanjing, China) at 140 °C and then shattered in a GL-01 pulverizer (Evian Machinery Co., Ltd., Shanghai, China). The pulverized raw materials were fed into a BHMS single-screw extruder (Nanjing Saiwang Technology Development Co., Ltd., Nanjing, China). The extruded lumber had a rectangular cross section of 40 mm in width and 4 mm in thickness.

2.2.2. Film-Roll Hot Press Molding

MAPE and talcum powder were evenly spread on the LLDPE film. Long dry straws were spread in parallel on the film. The proportions of straw, LLDPE, talcum and MAPE were 60%, 27%, 10% and 3%, respectively. The film was rolled up, and the straw stems were enveloped. The rolls were first pre-heated without pressure for 4 min and then hot pressed for 5 min under 10 MPa pressure in a SY01 hot press (Shanghai Board Equipment Technology Co., Ltd., Shanghai, China). In this process, the temperature was set to 140 °C. After hot pressing, the panel was cooled. A gauge was used to control the thickness of the straw/LLDPE composite. The size of the result panel was 165mm × 165mm × 4 mm. The detailed steps are shown in Figure 1. Straw particles and straw stems are shown in Figure 2.

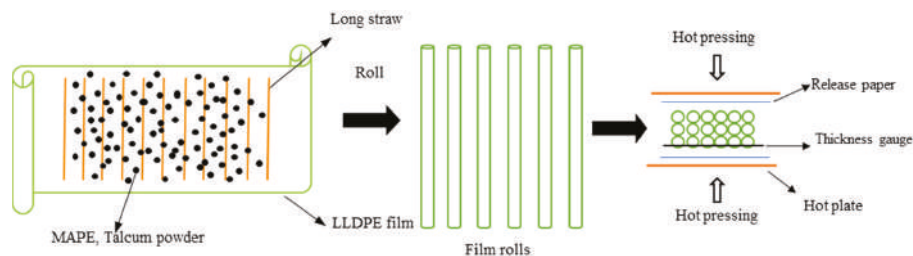


Figure 1. Preparation of straw/LLDPE composite through the film-roll hot pressing process.



Figure 2. Straw particle (a), straw stem (b).

2.3. Characterization of Straw/LLDPE Composite

2.3.1. Mechanical Property Tests

The unnotched impact strength was examined on the basis of GB/T 1043.1–2008 (“Plastics, Determination of Charpy Impact Properties, Part 1: Noninstrumented Impact Test”) with a JC-5 Charpy Impact Tester (Chengde Precision Testing Machine Co., Ltd., Chengde, Hebei, China). Specimens of 80mm × 10mm × 4 mm with a span length of 60 mm were analyzed. The striking velocity of the tests was 2.9 m/s, and the pendulum energy was 2 J. Six replicates of each preparation were tested to determine the impact strength.

The tensile tests were carried out in accordance with the method of GB/T 1040.2–2006 (“Plastics–Determination of tensile properties–Part 2: Test conditions for molding and extrusion plastics”). The test piece had a dumbbell shape, and its gauge length was 50 mm. The length of the specimen is parallel to the fiber orientation. The length of the test piece was 165 mm, the width of the narrow portion was 13 mm, and the thickness was 4 mm. The tests were carried out with a loading speed of 5 mm/min. The clamp stretches the specimen along the fiber orientation. Six replicates of each preparation were tested to obtain values for the tensile modulus and strength.

Flexural tests were carried out in accordance with the procedure of GB/T 1449–2005 (“Fiber-Reinforced Plastic composite- Determination of Flexural Properties”). The specimens of 80mm × 13mm × 4 mm had a span length of 64 mm. A loading speed of 2 mm/min was used for testing. The extension direction of the probes is perpendicular to the fiber orientation. Six replicates of each preparation were tested to obtain values for the flexural modulus and flexural strength. The tensile and flexural tests are completed by a CMT5504 mechanical testing machine (MTS industrial Systems (China) Co., LTD., Shanghai, China).

2.3.2. Density Tests

The composites were cut into 50 mm × 35 mm test pieces, and the length, width and thickness of the sample and the sample quality were measured according to GB/T 17657–2013 “Physical Testing Methods for Artificial Board and Finished Panels.” The composite density was characterized according to the ratio of mass to volume. Three replicates of each preparation were tested. The density of each replicate was measured once, then averaged the measurement of each replicate.

2.3.3. Water Absorption Performance

The material was formed into a test piece of 76.2mm × 25.4mm × 4 mm, and water absorption performance tests were carried out in accordance with the standard ASTM D570 “Standard Test Method for Water Absorption of Plastics.” The test pieces were dried in an oven for 24 h at 50 °C and then completely immersed in water at 24 °C. After 24 h, the test pieces were removed and weighed immediately. Vernier calipers were used to measure the thickness of test pieces before and after soaking. Three replicates of each preparation were tested. The mass and thickness of each replicate were measured three times and then averaged.

The water absorption and thickness expansion were calculated according to Equations (1) and (2), respectively:

$$c = \frac{m_1 - m_0}{m_0} \times 100\% \quad (1)$$

$$T = \frac{t_1 - t_0}{t_0} \times 100\% \quad (2)$$

where c denotes the water absorption mass fraction, T denotes the thickness expansion ratio, m_0 and t_0 denote the mass and thickness of the test piece after drying, respectively, and m_1 and t_1 denote the mass and thickness of the test piece after immersion, respectively.

2.3.4. Differential Scanning Calorimetry (DSC) Analysis

A differential scanning calorimeter (DSC Q100, TA Instruments, New Castle, PA, USA) was used to detect the melting behavior of the straw/LLDPE composite. The temperature of the straw/LLDPE composite sample was reduced to -70 °C, then heated to 180 °C at a rate of 10 °C min^{-1} . The entire testing process was performed under a nitrogen atmosphere.

2.3.5. Interfacial Morphological Observations by Scanning Electric Microscopy (SEM)

SEM was used to characterize the internal structural changes. The straw/LLDPE composite samples were frozen in liquid nitrogen for 10 min and then broken. The broken surfaces were sputter-coated with gold and then observed under a scanning electron microscope (FEI Quanta 200, FEI Co, Hillsboro, TX, USA) operated at an acceleration voltage of 12.5 kV. Three samples of each preparation were observed.

2.3.6. Rotating Rheological Tests

The dynamic rheological properties of straw/LLDPE composite were tested with a rotary rheometer (AR2000ex, TA Instruments, New Castle, PA, USA). Dynamic frequency scanning tests were conducted. The frequency range was 628.3 rad/s to 0.01 rad/s, and the strain was fixed at 0.05%. The above operations were carried out at 150 °C.

3. Results

3.1. Mechanical Property Analysis

The mechanical properties of extruded and hot pressed straw/LLDPE composite are shown in Figure 3.

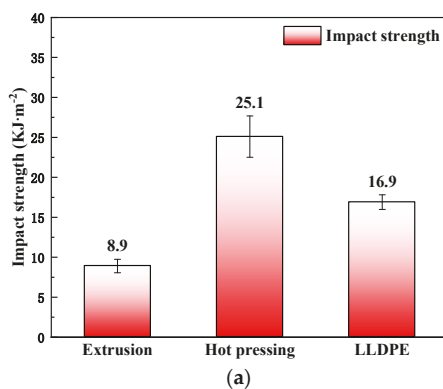


Figure 3. Cont.

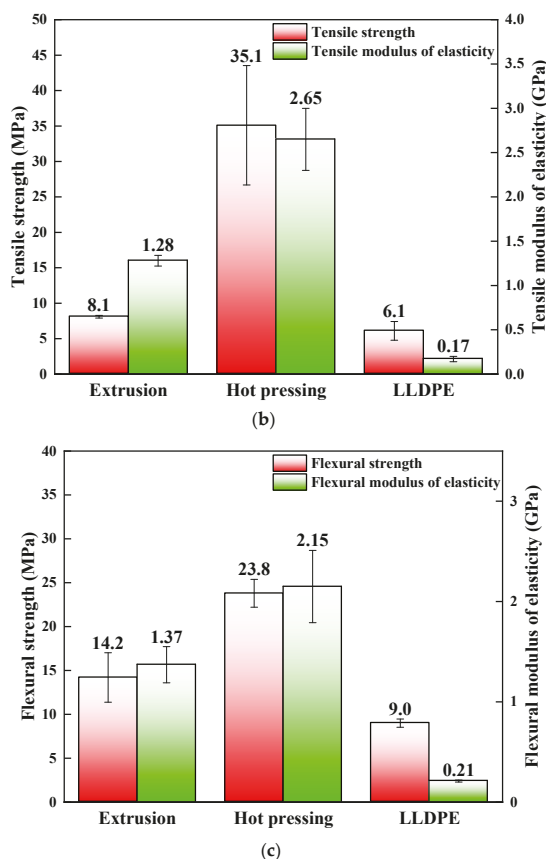


Figure 3. Impact strength (a), tensile properties (b) and bending properties (c) of hot pressed and extruded straw/LLDPE composite.

As shown in Figure 3, the mechanical properties of hot pressed straw/LLDPE composite were significantly higher than those of the extruded composite. Compared with the extruded panel, the hot pressed panel showed 181% greater impact strength (Figure 3a), 335% greater tensile strength, 107% greater tensile modulus (Figure 3b), 68% greater bending strength and 57% greater flexural modulus (Figure 3c). These results might be due to several factors.

Fiber orientation is known to positively influence the strength of reinforced composites. In the extruded straw/LLDPE composite, the straw fibers were randomly distributed, whereas in the hot pressed straw/LLDPE composite, the straw stems were highly oriented and remained at full length. Under loading, more energy was needed to overcome the interface bonding between the straws and the LLDPE as well as to break the straw stems themselves [18]. However, in extrusion preparation, the straw was in the forms of short fibers or powder, whose specific ratios were small and whose lengths were shorter than the critical length. If the length is less than the critical length, straw fibers are not be snapped but may be pulled out (the fibers slip from the matrix), i.e., straw fibers fail to fully exert the fiber strength within critical length and cannot play a reinforcing role (only as a filling material).

Because the length of straw stems is longer than straw fibers, the energy consumed for fiber extraction in the composite is higher, so the impact strength of hot pressed composite is higher. In addition, the fiber ends where stress is concentrated is the crack initiation point. The longer the fiber, the fewer the fiber ends in the composite. This is also the reason for its high impact strength.

3.2. Melting Performance Analysis

The melting performance of extruded and hot pressed straw/LLDPE composites is shown in Figure 4. The crystallinity of LLDPE was calculated according to Equation (3):

$$X_C = \frac{\Delta H_f(m_c / m_{LLDPE})}{\Delta H_f^0} \quad (3)$$

where ΔH_f denotes the melting enthalpy, m_c denotes the mass of the sample, m_{LLDPE} denotes the mass of LLDPE in the sample and ΔH_f^0 denotes the melting enthalpy of LLDPE with 100% crystallization, 293 J/g [19].

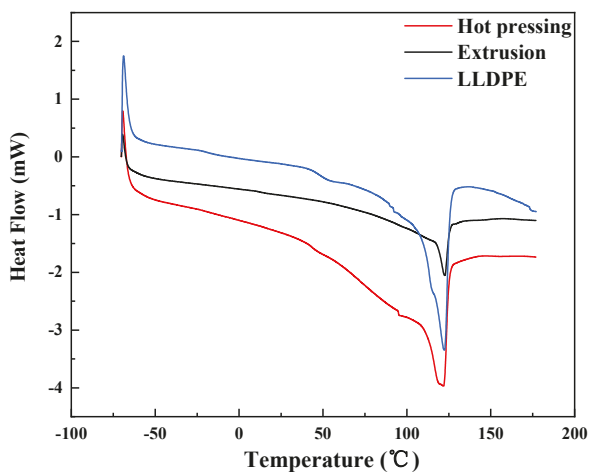


Figure 4. DSC image of hot pressed and extruded straw/LLDPE composite.

The data in Table 1 show the enthalpy and melting temperatures of samples. The composite manufactured by hot pressing and extrusion showed clear melting peaks at 121.97 °C and 122.61 °C, respectively, values similar to that of LLDPE, at 122.28 °C. The endothermic peaks might possibly be caused by the melting of LLDPE [20]. The peak of the hot pressed composite was wider and higher than that of the extruded composite. As shown in Table 1, the melting enthalpy of the hot pressed straw/LLDPE composite was much higher than that of the extruded composite. This shows that in hot pressed straw/LLDPE composite, straw fibers have a greater resistance to the melting of LLDPE, so that the melting process requires more heat than extruded composite [21]. This is because the melting enthalpy is related to the crystallinity. Compared with long straw stems, short straw fibers are more easily dispersed uniformly in the composite, and the contact area with LLDPE molecules increases, which plays a role in diluting LLDPE, so it can reduce the interaction between LLDPE molecules to a greater extent. The lower crystallinity, the fewer the heat required for heating and melting, i.e., the lower melting enthalpy. Pore structure of long straw in hot pressed composite would be expected to store more thermal energy, thereby resulting in slow progress of melting.

Table 1. Melting enthalpy and temperature of straw/LLDPE composite.

Sample	X_c (%)	T_m (°C)	ΔH_f (J/g)
LLDPE	17.41	122.28	51.01
hot pressing	35.76	121.97	62.87
extrusion	6.94	122.61	12.20

X_c —crystallinity; T_m —melting temperature; ΔH_f —melting enthalpy.

3.3. Water Absorption Performance Analysis

The water resistance test results of hot pressed and extruded straw/LLDPE composites are shown in Figure 5.

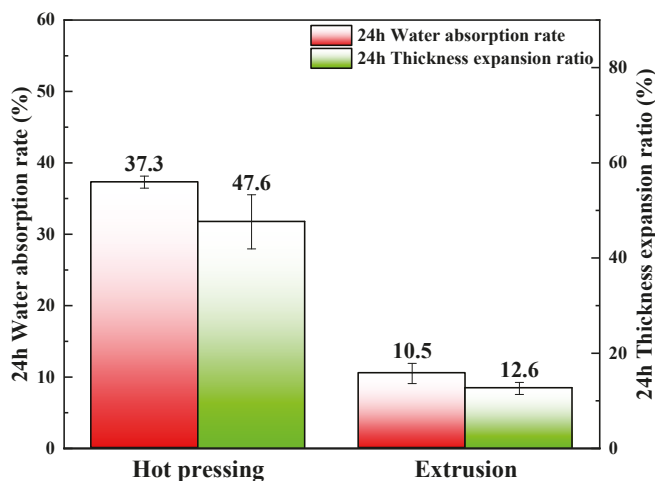


Figure 5. Water absorption mass fractions and thickness expansion ratios of hot pressed and extruded straw/LLDPE composite (immersed for 24 h).

Both the water absorption rate and the thickness expansion ratio of hot pressed straw/LLDPE composite were higher than those of the extruded composite, because in the hot pressing process, LLDPE matrix cannot completely fill in the cavities of the straw stem, and consequently the area of the straw contacting water is larger. In the extrusion process, almost all surfaces of the tiny straw particles were covered with LLDPE matrix [22]. Evenly distributing the raw material can effectively improve water resistance [23]. Possible effective measures include breaking the stem along the length of straw, which can take advantage of long fibers and also facilitate LLDPE matrix to enter the straw cavity during hot pressing, reducing the contact area between straw and water. In addition, a layer of LLDPE can be coated on the outside before hot pressing to seal the material.

3.4. Morphology of the Fracture Surface

3.4.1. Interface Bonding

The interfacial bonding and fiber orientation of the straw/LLDPE composite manufactured through the two methods were characterized by SEM (Figure 6).

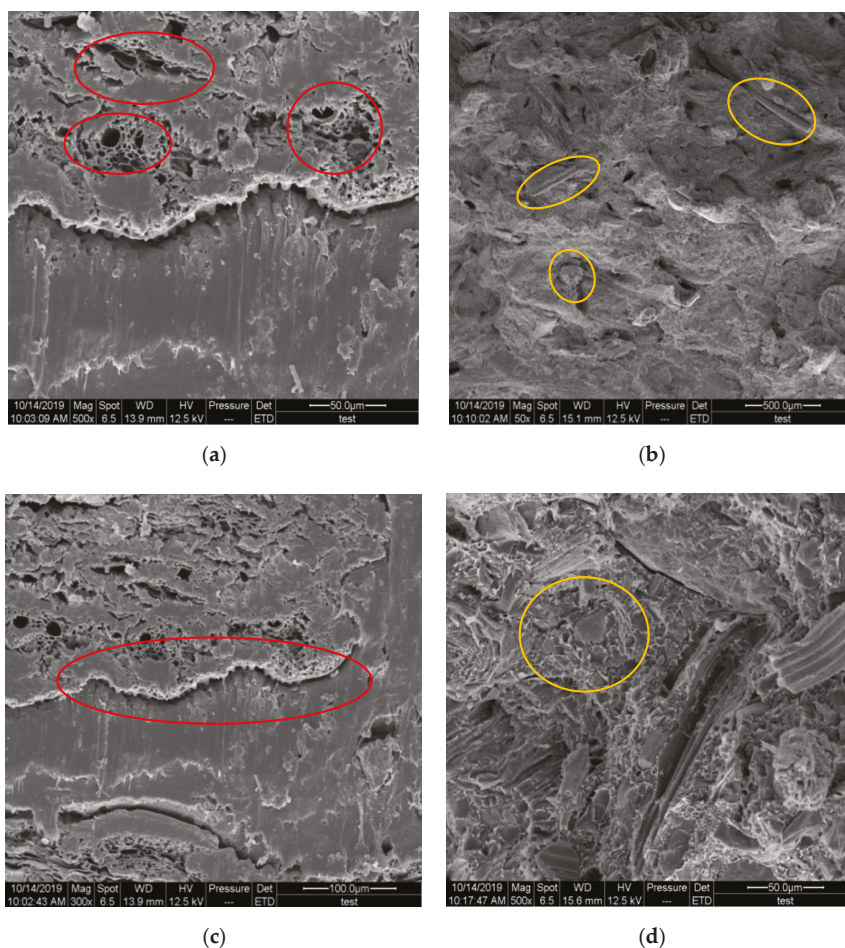


Figure 6. Microscopic morphology of the fracture surface of hot pressed (a,c) and extruded (b,d) straw/LLDPE composite.

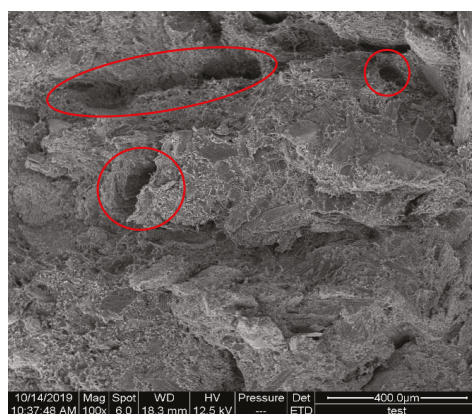
In the hot pressed composite, only the cross section of the straw could be seen (circles in Figure 6a), thus indicating that the direction of the straw was well fixed. In Figure 6b, the circled straw fibers in the extruded composite are randomly distributed. As further shown in circles of Figure 6c, a crack is present at the interface location between the straw and the LLDPE matrix in the hot pressed composite. In contrast, the straw and LLDPE matrix are relatively tightly combined in the extruded composite (circles in Figure 6d). In addition, the hollow structure of the straw in the hot pressed composite is not filled, thereby contributing to the higher impact strength. The holes left by straws that had been pulled out indicated that the straw fibers did not break in tensile loading (Figure 6b,d). However, the straw stems fully broke, and no holes were left in the matrix (Figure 6a,c), thus indicating that the long straw stems contributed to the strength. These structural results explained the differences in both the strength and water absorption of the composite. The hollow structures of the long straws that remained also explained the low density of the hot pressed straw/LLDPE composite (Table 2) [24]. In addition, the extrusion process can uniformly mix the raw materials and tightly combine them, thereby increasing the density of the composite.

Table 2. Density of extruded and hot pressed straw/LLDPE composite.

Manufactured Process	Extrusion	Hot Pressing
Density/(g·cm ⁻³)	1.31	0.83

3.4.2. Analysis of Tensile Fracture Mechanism

In the straw/LLDPE composite, the main fracture forms are fiber fracture, interface detachment and matrix fracture. In Figure 7, the broken straw fiber (Circle 1) and the tip-shaped LLDPE (Circle 2) can be seen. In Figure 8, we can see the holes (The circled part) left by short fibers pull-out, indicating that the strength of the straw itself is not fully exerted in the extruded composite.

**Figure 7.** Optical micrograph of fracture surface of the hot pressed straw/LLDPE composite.**Figure 8.** SEM of fracture surface of the extruded straw/LLDPE composite.

Tensile stress-strain curve of hot pressed and extruded straw/LLDPE composites is shown in Figure 9. Comparing Figure 9a,b, it can be seen that the stress-strain curve of the extruded composite is relatively smooth, thus the fracture process is relatively gentle, which indicates that the tougher LLDPE plays a major bearing role. Therefore, combining Figures 8 and 9b shows that the mechanical strength of the extruded composite mainly comes from the LLDPE matrix. In the curve image of the hot pressed composite, the stress drops suddenly. This is due to the sudden separation of the straw fiber and LLDPE matrix interface and the sudden breaking of the straw. Combining Figures 7 and 9a,

it can be known that the mechanical strength of the hot pressed composite mainly comes from the combination of the fiber matrix and the strength of the straw, and the matrix itself has less effect.

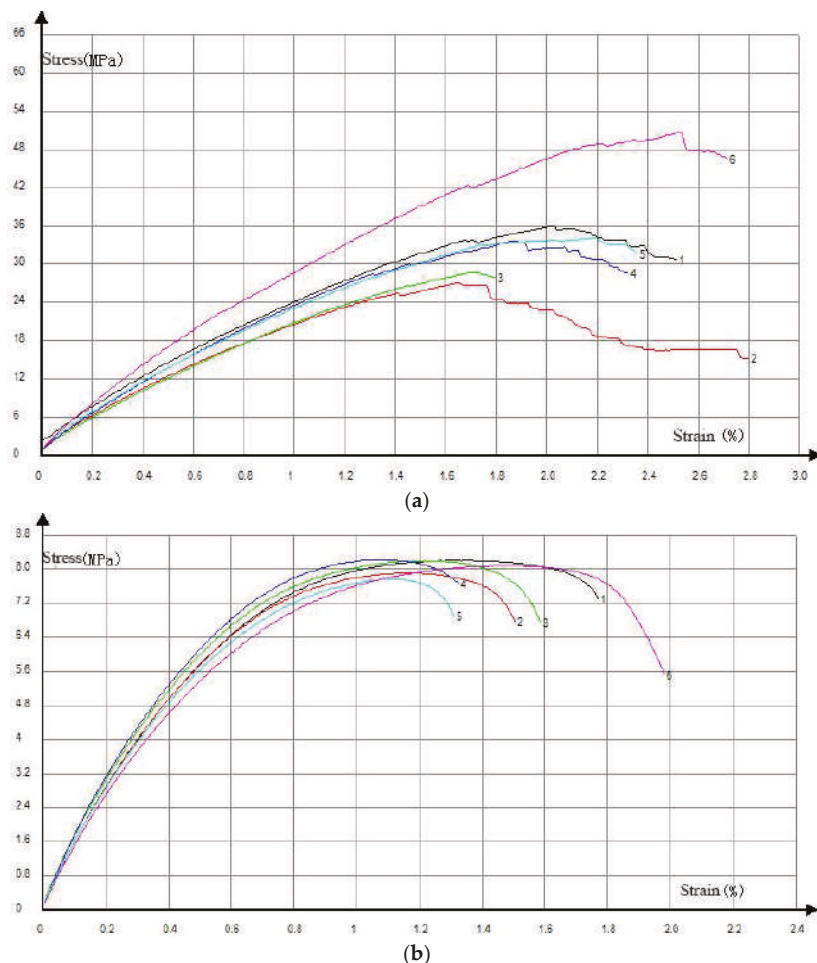
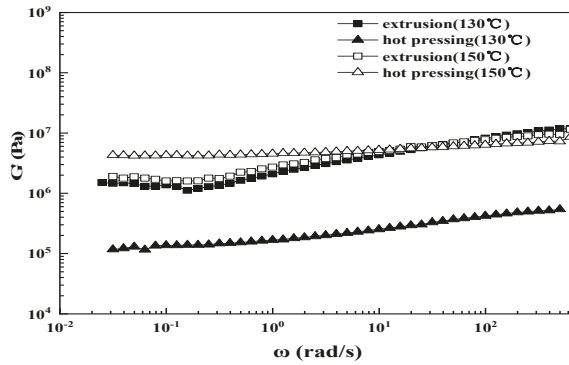


Figure 9. Tensile stress-strain curves of specimen 1 to 6 of hot pressed (a) and extruded (b) straw/LLDPE composite.

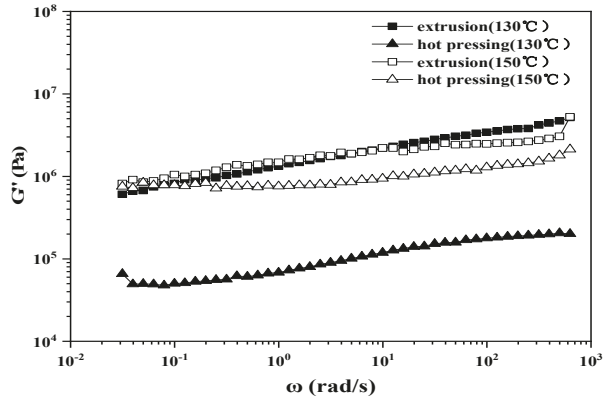
3.5. Dynamic Rheological Performance Analysis

Plots of the storage modulus, loss modulus, loss tangent value and complex viscosity vs ω of straw/LLDPE composite is shown in Figure 10. Figure 10a shows the relationship between the storage modulus (G') and the angular frequency. By increasing the test temperature (from 130 °C to 150 °C), a large increase in storage modulus can be seen for the hot pressed composite, which is not the case for extruded composite. This may be because at a temperature closer to the T_m of LLDPE (T_m of LLDPE measured by DSC is 122 °C), the LLDPE melt is still relatively hard and the molecular chain flexibility is poor. In this case, the uneven fiber distribution has a negative effect on the deformation of the matrix. In contrast to the changes in G' of hot pressed straw/LLDPE composite with frequency, a modulus platform in the low frequency region was observed for the extruded straw/LLDPE composite. This phenomenon, so-called solid-like behavior [25–27], occurs because of

the formation of three-dimensional ordered structures such as agglomerates, skeletons and networks inside the system [28]. The viscoelastic behavior of the low ω region is the motion response of the long-chain segment of the polymer or even the entire macromolecular chain, and the three-dimensional ordered structure limits the long-term movement of macromolecular motion units [25,26,29]. The hot pressed straw/LLDPE composite showed very little change as the frequency increased. The slight modulus increase occurred because the parallel straws acted as a skeleton and prevented the LLDPE from sliding. Similarly, as shown in Figure 10b, both the hot pressed and extruded straw/LLDPE composites showed stable loss modulus with frequency variation.

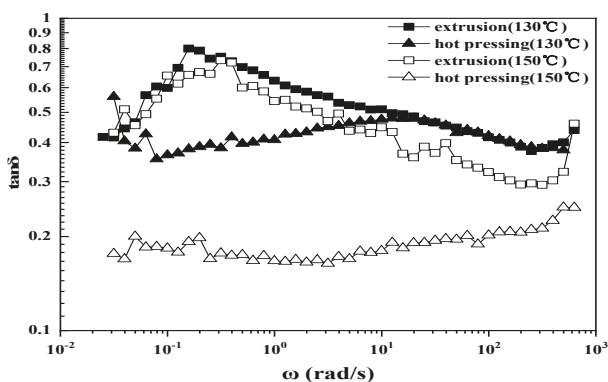


(a)

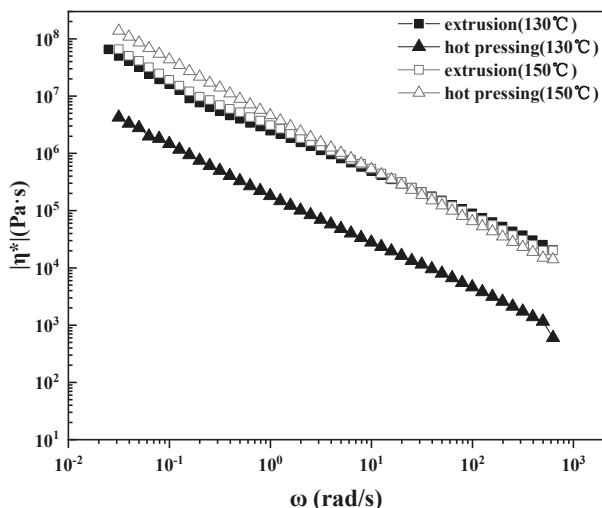


(b)

Figure 10. Cont.



(c)



(d)

Figure 10. Plots of the storage modulus (a), loss modulus (b), loss tangent value (c) and complex viscosity (d) vs ω of straw/LLDPE composite.

Figure 10c shows the relationship between the loss tangent value of the straw/LLDPE melting and the angular frequency. The loss tangent value is the ratio of the loss modulus to the storage modulus. As shown in Figure 10c, the $\tan \delta$ of the extruded straw/LLDPE melt showed a sharp peak at around 0.2 rad/s, whereas the hot pressed straw/LLDPE melt did not show a clear peak. In the $G'—\omega$ curve, the $\tan \delta$ peak appears along with the modulus platform; that is, the $\tan \delta$ peak is also a characteristic of solid-like behavior [30]. The change in the value of $\tan \delta$ indicates a change in viscoelasticity, thus demonstrating that the viscoelasticity of the hot pressed composite is fairly stable [31]. As shown in Figure 10c, $\tan \delta$ was less than 1 over the entire scanning frequency range, thus indicating that the straw/LLDPE melting exhibited elasticity. We conclude that hot pressed straw/LLDPE composite had the clearest elastic characteristics, according to its low $\tan \delta$ value and high G' value [32].

Figure 10d shows the relationship between the complex viscosity ($|\eta^*|$) and the angular frequency.

As shown in the figure, as the frequency increases, the viscosity shows a downward trend, i.e., the phenomenon of shear thinning occurs. This is because the viscosity is the ratio of stress to strain rate, and according to Power-Law Equation

$$\sigma = K \cdot \gamma^n \tag{4}$$

We can get Equation

$$\eta = \frac{\sigma}{\gamma} = K \cdot \gamma^{n-1} \tag{5}$$

where η denotes the viscosity, σ denotes the stress, γ denotes the strain rate, K and n are both constants. High-molecular polymers such as PE are pseudoplastic liquids, and the n value of the pseudoplastic fluid is less than 1, so when the strain rate increases, the viscosity of the system decreases. The opposite of pseudoplastic fluid is dilatant liquid, such as corn paste, whose n value is more than 1, and the viscosity will increase as the strain rate increases [33].

There is always a certain speed gradient between the various liquid layers when the polymer flows. If a large molecule passes through several liquid layers with different flow rates at the same time, each part of the same macromolecule must advance at different speeds. This situation obviously cannot last. Therefore, during the flow, each long-chain molecule always tries to make itself all enter the liquid layer with the same flow rate. The parallel distribution of liquid layers with different flow rates results in the orientation of the macromolecules in the flow direction, which causes the viscosity to decrease with increasing frequency during the flow. With the increase of experimental temperature, the kinetic energy of the molecule of hot pressed composite is increased, but also increases the degree of intermolecular collision, which makes the viscosity increase.

In dynamic tests, the relationship between dynamic viscosity and loss viscosity, the Cole-Cole curve, can give information about the various relaxation processes in heterogeneous polymer systems. As shown in Figure 11, the right end of the curve of the extruded composite is slightly upturned, so-called “tailing” phenomenon occurs. This shows that there are two relaxation mechanisms in the system of the extruded composite. This may be because LLDPE is more prone to entanglement in the extruded composite system, and this structure relaxes very slowly.

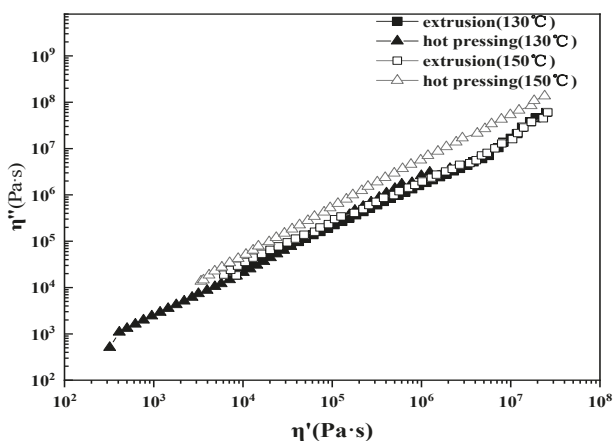


Figure 11. Loss viscosity of straw/LLDPE composite as a function of storage viscosity.

3.6. Physical Drawing of Extruded and Hot Pressed Straw/LLDPE Composites

The physical picture of the extruded and hot pressed composites is shown in Figure 12.

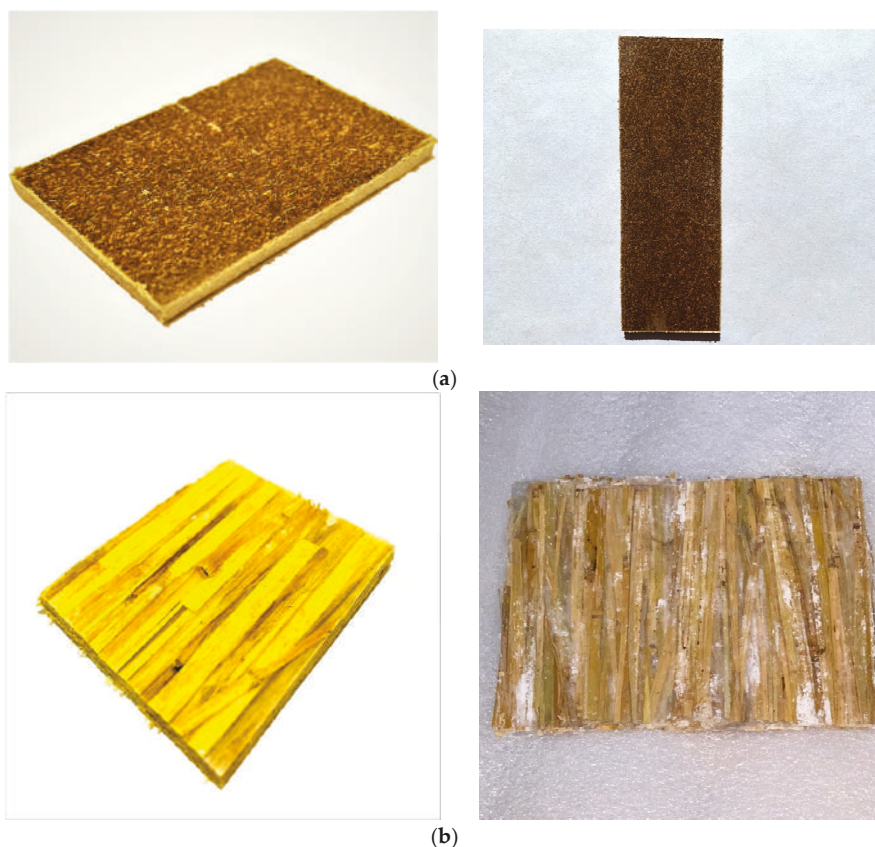


Figure 12. Extruded (a) and hot pressed (b) straw/LLDPE composites.

4. Conclusions

This study developed a new method for constructing straw-plastic composite and compared it with conventional extrusion methods. Tests of the mechanical properties verified that the hot pressed long straw stem reinforced LLDPE composite had relatively higher strength and modulus. Microstructural observations showed better fiber orientation of the hot pressed straw/LLDPE composite, and this factor had the greatest influence on the mechanical properties of the straw/LLDPE composite. According to the results of DSC, straw fibers have a greater resistance to the melting of LLDPE in hot pressed straw/LLDPE composite, so that the melting process requires more heat than extruded composite. The results from dynamic rheological analysis indicated that the storage modulus of the straw/LLDPE melt manufactured by hot pressing was more stable than that of the extruded composite. The elastic characteristics of the hot pressed straw/LLDPE melt were more pronounced than those of the extruded composite. The hot pressed straw/LLDPE composite had higher water absorption, thus indicating its ability to regulate the surrounding relative humidity. Straw/LLDPE composites are expected to be applicable in interior decoration materials, owing to their high strength-to-weight ratio and the absence of chemical emission such as those from adhesives.

Author Contributions: W.W. and L.Z. conceived and designed the experiments; L.Z. and H.X. performed the experiments; W.W. and L.Z. analyzed the data; L.Z. wrote the paper; W.W. revised the paper. All authors have read and agreed to the published version of the manuscript.

Funding: This research received no external funding.

Acknowledgments: The authors gratefully acknowledge the support of the National Natural Science Foundation of China (No. 31670573), and the Innovation Team Sustainable Development Special Project of the Central University Fundamental Research Business Expenses Special Fund Project (No. 2572017ET05).

Conflicts of Interest: The authors declare no conflict of interest.

References

1. Militky, J.Í.; Jabbar, A. Comparative evaluation of fiber treatments on the creep behavior of jute/green epoxy composites. *Compos. Part B Eng.* **2015**, *80*, 361–368. [[CrossRef](#)]
2. Bengtsson, M.; Baillif, M.L.; Oksman, K. Extrusion and mechanical properties of highly filled cellulose fibre–polypropylene composites. *Compos. Part A* **2007**, *38*, 1922–1931. [[CrossRef](#)]
3. Graupner, N.; Herrmann, A.S.; Müssig, J. Natural and man-made cellulose fibre-reinforced poly(lactic acid) (PLA) composites: An overview about mechanical characteristics and application areas. *Compos. Part A Appl. Sci. Manuf.* **2009**, *40*, 810–821. [[CrossRef](#)]
4. Dicker, M.P.M.; Duckworth, P.F.; Baker, A.B.; Francois, G.; Weaver, P.M. Green composites: A review of material attributes and complementary applications. *Compos. Part A Appl. Sci. Manuf.* **2014**, *56*, 280–289. [[CrossRef](#)]
5. Liu, Z.; Huang, F.; Li, B. Investigating contribution factors to China’s grain output increase in period of 2003 to 2011. *Trans. Chin. Soc. Agric. Eng.* **2013**, *29*, 1–8.
6. Li, Y.; Cheng, C.; Xu, L. Design and experiment of baler for 4L-4.0 combine harvester of rice and wheat. *Trans. Chin. Soc. Agric. Eng.* **2016**, *32*, 29–35.
7. Nyambo, C.; Mohanty, A.K.; Misra, M. Effect of Maleated Compatibilizer on Performance of PLA/Wheat Straw-Based Green Composites. *Macromol. Mater. Eng.* **2011**, *296*, 710–718. [[CrossRef](#)]
8. Xiao, Y.; Fu, M. Forming Technology of PP/Straw composites by hot pressing. *Eng. Plast. Appl.* **2005**, *1*, 34–37.
9. Zhang, D.; He, C.; Liu, J. Mechanical properties of straw-powder/PP composites. *Trans. Chin. Soc. Agric. Eng.* **2010**, *26*, 380–384.
10. Zabihzadeh, M.; Dastoorian, F.; Ebrahimi, G. Effect of MAPE on Mechanical and Morphological Properties of Wheat Straw/HDPE Injection Molded Composites. *J. Reinf. Plast. Compos.* **2010**, *29*, 123–131. [[CrossRef](#)]
11. Koster, L. Influencing factors and parameters in the extrusion process. *KGK Rubberpoint.* **2005**, *58*, 362–365.
12. Mandell, J.F.; McGarry, F.J.; Huang, D.D.; Li, C.G. Some effects of matrix and interface properties on the fatigue of short fiber-reinforced thermoplastics. *Polym. Compos.* **2010**, *4*, 32–39. [[CrossRef](#)]
13. Kakisawa, H.; Honda, K.; Kagawa, Y. Effect of wear on interface frictional resistance in fiber-reinforced composite: Model experimental. *Mater. Sci. Eng. A* **2000**, *284*, 226–234. [[CrossRef](#)]
14. Park, C.B. *Polymeric Foams: Science and Technology*; CRC Press: Boca Raton, FL, USA, 2006.
15. Machado, J.S.; Santos, S.; Pinho, F.F.S.; Luis, F.; Alves, A.; Simoes, R.; Rodrigues, J.C. Impact of high moisture conditions on the serviceability performance of wood plastic composite decks. *Mater. Design.* **2016**, *103*, 122–131. [[CrossRef](#)]
16. Sudar, A.; Renner, K.; Moczo, J.; Lummerstorfer, T.; Burgstaller, C.; Jerabek, M.; Gahleitner, M.; Doshev, P.; Pukanszky, B. Fracture resistance of hybrid PP/elastomer/wood composites. *Compos. Struct.* **2016**, *141*, 146–154. [[CrossRef](#)]
17. Yilmazer, U. Effects of the processing conditions and blending with linear low-density polyethylene on the properties of low-density polyethylene films. *J. Appl. Polym. Sci.* **2010**, *42*, 2379–2384. [[CrossRef](#)]
18. Phelps, J.H.; Iii, C.L.T. An anisotropic rotary diffusion model for fiber orientation in short- and long-fiber thermoplastics. *J. Non-Newton. Fluid Mech.* **2009**, *156*, 165–176. [[CrossRef](#)]
19. Wilfong, D.L.; Knight, G.W. Crystallization mechanisms for LLDPE and its fractions. *J. Polym. Sci. Part A Polym. Chem.* **1990**, *28*, 861–870. [[CrossRef](#)]
20. Tubbs, F.R. Physiological Studies in Plant Nutrition: II. The Effect of Manurial Deficiency upon the Mechanical Strength of Barley Straw. *Ann. Botany.* **1930**, *44*, 147–160. [[CrossRef](#)]
21. Prasad, A. A quantitative analysis of low density polyethylene and linear low density polyethylene blends by differential scanning calorimetry and fourier transform infrared spectroscopy methods. *Polym. Eng. Sci.* **2010**, *38*, 1716–1728. [[CrossRef](#)]

22. Huang, X.; Li, Q.; Yang, M.; Luo, Y.; Ye, X.; Yang, Y. Thermal Decomposition and Kinetics Analysis of Larger Particle Neodymium Oxalate. *J. Chin. Soc. Rare Earths* **2016**, *34*, 83–92.
23. Haque, A.; Jeelani, S. Environmental Effects on the Compressive Properties: Thermosetting vs. Thermoplastic Composites. *J. Reinf. Plast. Compos.* **1992**, *11*, 146–157. [[CrossRef](#)]
24. Czel, G.; Czigan, T. A Study of Water Absorption and Mechanical Properties of Glass Fiber/Polyester Composite Pipes – Effects of Specimen Geometry and Preparation. *J. Compos. Mater.* **2008**, *42*, 2815–2827. [[CrossRef](#)]
25. Aranguren, M.I. Effect of reinforcing fillers on the rheology of polymer melts. *J. Rheol.* **1992**, *36*, 1165–1182. [[CrossRef](#)]
26. Wu, G.; Song, Y.; Zheng, Q.; Du, M.; Zhang, P. Dynamic rheological properties for HDPE/CB composite melts. *J. Appl. Polym. Sci.* **2003**, *88*, 2160–2167. [[CrossRef](#)]
27. Romani, F.; Corrieri, R.; Braga, V.; Ciardelli, F. Monitoring the chemical crosslinking of propylene polymers through rheology. *Polymer* **2002**, *43*, 1115–1131. [[CrossRef](#)]
28. Prashantha, K.; Soulestin, J.; Lacrampe, M.F.; Krawczak, P.; Dupin, G.; Claes, M. Masterbatch-based multi-walled carbon nanotube filled polypropylene nanocomposites: Assessment of rheological and mechanical properties. *Compos. Sci. Technol.* **2009**, *69*, 1756–1763. [[CrossRef](#)]
29. Wang, M.; Wang, W.; Liu, T.; Zhang, W.D. Melt rheological properties of nylon 6/multi-walled carbon nanotube composites. *Compos. Sci. Technol.* **2008**, *68*, 2498–2502. [[CrossRef](#)]
30. Dong, Q.; Zheng, Q.; Du, M.; Zhang, M.Q. Temperature-dependence of dynamic rheological properties for high-density polyethylene filled with graphite. *J. Mater. Sci.* **2005**, *40*, 3539–3541. [[CrossRef](#)]
31. Liang, J.Z.; Li, R.K.Y.; Tjong, S.C. Effects of glass bead size and content on the viscoelasticity of filled polypropylene composites. *Polym. Test.* **2000**, *19*, 213–220. [[CrossRef](#)]
32. Unwin, A.P.; Hine, P.J.; Ward, I.M.; Guseva, O.A.; Schweizer, T.; Fujita, M.; Tanaka, E.; Gusev, A.A. Predicting the visco-elastic properties of polystyrene/SIS composite blends using simple analytical micromechanics models. *Compos. Sci. Technol.* **2017**, *142*, 302–310. [[CrossRef](#)]
33. Masao, D.; See, H. *Introduction to Polymer Physics*; South China University of Technology Press: Guangzhou, China, 2011.



© 2020 by the authors. Licensee MDPI, Basel, Switzerland. This article is an open access article distributed under the terms and conditions of the Creative Commons Attribution (CC BY) license (<http://creativecommons.org/licenses/by/4.0/>).

Article

Facile Construction of Superhydrophobic Surfaces by Coating Fluoroalkylsilane/Silica Composite on a Modified Hierarchical Structure of Wood

Jiajie Wang, Yingzhuo Lu, Qindan Chu, Chaoliang Ma, Lianrun Cai, Zhehong Shen * and Hao Chen *

School of Engineering, Zhejiang A&F University, Hangzhou 311300, China; laowangwj0126@163.com (J.W.); tqy033201@163.com (Y.L.); 15306587705@163.com (Q.C.); qq843543030@163.com (C.M.); cailianr21@163.com (L.C.)

* Correspondence: zhehongshen@zafu.edu.cn (Z.S.); haochen@zafu.edu.cn (H.C.)

Received: 15 March 2020; Accepted: 1 April 2020; Published: 4 April 2020

Abstract: Constructing superhydrophobic surfaces by simple and low-cost methods remains a challenge in achieving the large-scale commercial application of superhydrophobic materials. Herein, a facile two-step process is presented to produce a self-healing superhydrophobic surface on wood to improve water and mildew resistance. In this process, the natural hierarchical structure of wood is firstly modified by sanding with sandpaper to obtain an appropriate micro/nano composite structure on the surface, then a fluoroalkylsilane/silica composite suspension is cast and dried on the wood surface to produce the superhydrophobic surface. Due to the full use of the natural hierarchical structure of wood, the whole process does not need complicated equipment or complex procedures to construct the micro/nano composite structure. Moreover, only a very low content of inorganic matter is needed to achieve superhydrophobicity. Encouragingly, the as-obtained superhydrophobic surface exhibits good resistance to abrasion. The superhydrophobicity can still be maintained after 45 abrasion cycles under the pressure of 3.5 KPa and this surface can spontaneously recover its superhydrophobicity at room temperature by self-healing upon damage. Moreover, its self-healing ability can be restored by spraying or casting the fluoroalkylsilane/silica composite suspension onto this surface to replenish the depleted healing agents. When used for wood protection, this superhydrophobic surface greatly improves the water and mildew resistance of wood, thereby prolonging the service life of wood-based materials.

Keywords: superhydrophobic surfaces; self-healing; natural hierarchical microstructures; wood

1. Introduction

The fabrication of superhydrophobic surfaces with water contact angles (CAs) larger than 150° and sliding angles less than 10° has attracted extensive research attention worldwide due to its great potential in both theoretical research and practical applications, such as self-cleaning [1], anti-fouling [2], durable antibacterial uses [3], oil/water separation [4,5], gas sensing and droplet manipulation [6]. The superhydrophobic property of the surface is controlled by its chemical composition and topography. The cooperation of micro/nano scale hierarchical structures with low-surface energy materials has been the main strategy to fabricate superhydrophobic surfaces [7]. Through years of extensive efforts, many chemical and physical methods that generate superhydrophobic surfaces have been developed, such as plasma polymerization/etching [8], chemical vapor deposition [9–12], solvent-mediated phase separation [13], and polymer self-assembly [14–16]. However, some superhydrophobic surfaces are apt to lose their superhydrophobicity during practical applications since the artificial micro/nano hierarchical architectures are susceptible to being damaged after a slight scratch, abrasion, or even

brief contact with fingers, which has hampered their widespread application. Recently, although many researchers have reported the successful fabrication of mechanically durable superhydrophobic surfaces [17–23], it is still highly desired to construct superhydrophobic surfaces by simple and low-cost methods to achieve the large-scale commercial application of superhydrophobic materials.

Wood, as a renewable resource, has great potential in decorative fields to substitute steel, stone, glass, minerals, and synthetic resin. Nevertheless, because it contains many hydrophilic groups such as hydroxyl groups, the wood is apt to absorb water, which can result in dimensional instability and attacks by microorganisms including decay fungi and mildew [24–26]. Therefore, it is of great practical significance to construct a high-performance superhydrophobic surface for the wood.

In this work, we have described a facile process to fabricate a robust self-healing superhydrophobic surface on wood with improved water and mildew resistance. In this process, the natural hierarchical structure of wood was firstly modified by sanding with sandpaper to obtain an appropriate micro/nano composite structure on the surface, then a fluoroalkylsilane/silica composite suspension was cast and dried on the wood surface to produce the superhydrophobic surface. Due to the full use of the natural hierarchical structure of wood, the whole process does not need complicated equipment or complex procedures to construct the micro/nano composite structure. Moreover, only a very low content of inorganic matter is needed to achieve superhydrophobicity. Therefore, the as-obtained superhydrophobic surface is transparent and unveils the natural grains and textures of the original surface. More importantly, benefiting from the unique micro/nano composite structure originated from the natural hierarchical structure of wood, the superhydrophobic surface exhibits robust superhydrophobic performance against physical damages. Furthermore, owing to the intrinsic porous structures of wood, the superhydrophobic surface can preserve a large number of fluoroalkylsilane moieties as the healing agent in the wood pores such as cell cavities and grooves. Once the primary top fluoroalkylsilane layer is decomposed or scratched, the internally-preserved healing agent in the wood pores will migrate to the surface to heal the superhydrophobicity at room temperature. Thus, the superhydrophobic surface exhibits good self-healing ability when damaged. And this self-healing ability can be restored by spraying or casting the fluoroalkylsilane/silica composite suspension onto the wood surface to replenish the depleted healing agents. In addition, when used for wood protection, this superhydrophobic surface greatly improves the water and mildew resistance of wood, thereby prolonging the service life of wood-based materials.

2. Materials and Methods

2.1. Materials

Ethanol (AR, $\geq 99.5\%$), nano fumed silica (99.8wt%, diameter: 7–40nm) and acetic acid (AR, $\geq 99.5\%$) were purchased from Shanghai Chemical Reagent Co. (China). Perfluorooctyltriethoxysilane (KH1322) and Chinese fir wood were kindly donated by Zhejiang Longyou Wood Bond Co. (China). Woodblocks with a size of $40 \times 35 \times 10$ mm (longitudinal \times radial \times tangential) were obtained from the sapwood of Chinese fir (*Cunninghamia lanceolata*).

2.2. Preparation of Fluoroalkylsilane/Silica Suspension

Typically, 0.2 g of KH1322 (as a fluoroalkylsilane) was dissolved in 10 g of ethanol. The solution was mildly stirred until it became homogeneous and transparent. Then, 4 mg silica nanoparticles (the ratio of silica to KH1322 was 2%) were added into the previous solution and ultrasonically treated for one minute until the resulting fluoroalkylsilane/silica composite suspension was homogeneous.

2.3. Preparation of Superhydrophobic Surfaces

The woodblock was first sanded with 240-grit sandpaper under a pressure of $40 \text{ KN} \cdot \text{m}^{-2}$ until a visible clean smooth surface was obtained. In this way, the natural hierarchical structure of wood was modified to obtain an appropriate micro/nano composite structure on the surface. Then, the above

suspension was cast onto the wood surface (40 mm × 35 mm) and heated in the oven for a certain period of time to form superhydrophobic surfaces. The dosage of KH1322 plus silica on the wood surface was calculated to be about 4 g · m⁻². Unless specified, the heating temperature was 120 °C, and the duration of heating was 2 hours.

2.4. Characterization

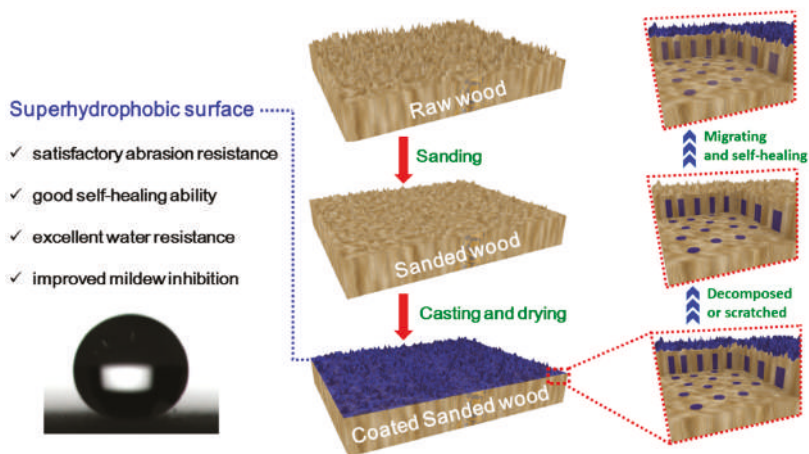
The surface morphology was observed by scanning electronic microscopy (SEM). The VK-X 3D optical laser microscope system (OPM) was used to characterize the three-dimensional surface morphology. The roughness factor (Ra) was calculated according to JIS B0601:1994. The measurement of the surface wettability was performed using a dynamic contact angle (CA) testing instrument (OCA40, Filderstadt, Germany). CA was recorded at 30 seconds after a droplet of liquids (5 µL) was placed on the surface. The sliding angle (SA) was measured by recording the tilt angle of the sample platform at which a liquid droplet (10 µL) started to roll off the surface. Average water CAs were obtained on radial sections by measuring the same sample at six different positions. Fourier transform infrared spectroscopy (FTIR) measurements were carried out using a Nicolet Nexus 470 spectrometer (Thermo Fisher, Waltham, MA, USA). The chemical composition of the wood surface was measured by X-ray photoelectron spectroscopy (XPS, Perkin-Elmer PHI 5000C ECSA, Waltham, MA, USA). The abrasion resistance of the superhydrophobic surface was evaluated by dragging a piece of 240-grit sandpaper under 500 g of weight in one direction with a speed of 1 cm s⁻¹ at a distance of 10 cm per cycle. Digital pictures were captured using a Canon Power Shot A 95 digital camera, and the optical images were obtained with the VK-9710 microscope. Unless specified, the water CA tests and characterizations such as SEM, XPS, FTIR, and OPM were carried on the radial sections of wood.

3. Results and Discussion

3.1. Fabrication of Superhydrophobic Surfaces

The process to fabricate the superhydrophobic surface was shown in Scheme 1. The raw wood was first sanded with 240-grit sandpapers to modify the natural hierarchical structure of the wood to obtain an appropriate micro/nano composite structure on the surface. Then, the homogeneous suspension of KH1322 fluoroalkylsilane and silica was cast onto the surface of the sanded wood and heated in an oven or room-dried for a certain period of time to form the superhydrophobic surface. The resulting material is denoted as coated sanded wood.

Figure 1a displays that the natural hierarchical structure of raw wood is highly uneven with a maximum height of more than 200 µm (Figure 1b) and a roughness factor (Ra) of 38 µm. Moreover, some pores were found to be too large (the inset of Figure 1a) to support the weight of the water droplet that resulted in a homogeneous wetting, namely, Wenzel states [27]. Thus, this natural hierarchical structure is not applicable to directly construct the superhydrophobic surface. As expected, when the fluoroalkylsilane/silica suspension was cast and dried on the surface of this raw wood, the water CA on the resultant surface was only 132°, hence the superhydrophobicity cannot be achieved. Figure 1c demonstrates that a relatively uniform micro/nano hierarchical structure can be obtained by sanding the raw wood with 240-grit sandpapers. Figure 1d manifests that the maximum height and Ra of the modified surface structure of sanded wood decreased to be less than 100 µm and 5.69 µm, respectively. The air in the uniform pores can reduce contact areas between water droplets and surface, resulting in the Cassie–Baxter state [28]. Benefiting from this state, the coated surface obtained by drying the fluoroalkylsilane/silica suspension on the sanded wood exhibited a typical superhydrophobic feature with a water CA of 160° and a sliding angle below 10°.



Scheme 1. Schematic procedure for the preparation of the superhydrophobic wood surface (middle) and its self-healing mechanism (right).

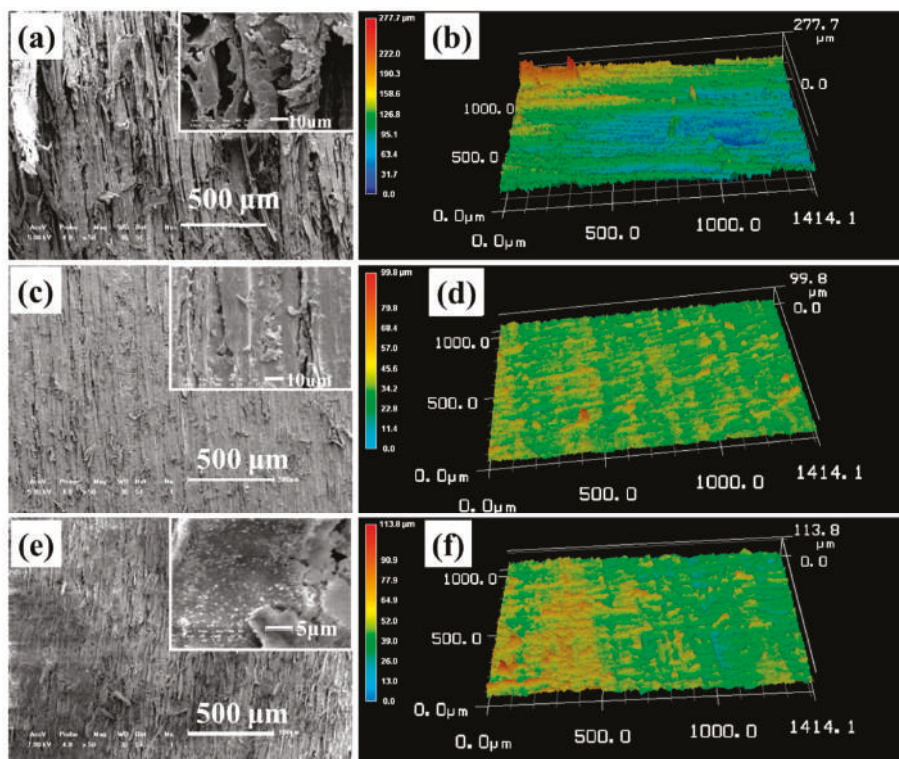


Figure 1. (a) Scanning electronic microscopy (SEM) and (b) 3D optical laser microscope system (OPM) images of raw wood. (c) SEM and (d) 3D OPM images of sanded wood. The insets are magnified SEM images with scale bars at 10 μm. (e) SEM and (f) 3D OPM image of sanded wood coated with KH1322 fluoroalkylsilane and silica.

To understand the detailed formation mechanism of this superhydrophobic surface, its three-dimensional surface morphology was investigated by SEM and OPM. The low magnification SEM image of coated sanded wood in Figure 1e displays a similar micromorphology compared with that of the sanded wood without coating (Figure 1c). However, we can find some new particles on the surface in its high magnification SEM image (the inset of Figure 1e). These particles should be the silane oligomers produced by the KH1322 hydrolysis and silica particles. Their emergence led to an increase in the roughness. As a result, both the maximum height (113.8 μm) and Ra (10.21 μm) of coated sanded wood in the OPM image of Figure 1f have a slight increase compared with the data of the sanded wood without coating (Figure 1d).

Usually, the raw wood surface is hydrophilic due to its naturally porous structure with abundant hydroxyl groups [25]. Thus, the chemical polarity of the surface must be changed to achieve superhydrophobicity. The comparison of FTIR spectra in Figure 2 reveals that there are five new absorbance bands for the coated sanded wood compared with the raw wood. Among them, two peaks at 1267 and 617 cm^{-1} can be attributed to the vibrations of CF_3 and CF groups [29]. The other three absorbance peaks at 898, 805 and 467 cm^{-1} are ascribed to the vibrations of Si-O. It is believed that the molecular chains with these hydrophobic groups combine with the uniform micro/nano hierarchical structure of the sanded wood to achieve the construction of the superhydrophobic wood surface.

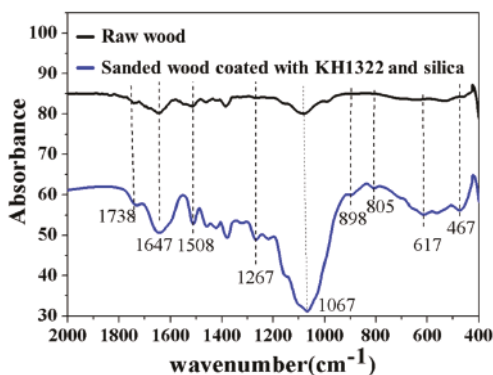


Figure 2. Comparison of Fourier transform infrared spectroscopy (FTIR) spectra between raw wood and sanded wood coated with KH1322 fluoroalkylsilane and silica.

3.2. The Effect of Silica on the Surface Wettability

In this work, the silica was added to prepare the hydrophobic surface. Thus, the effect of silica content on the surface wettability was investigated. It was found that the water CA increased from 152° to 160° when the ratio of silica to KH1322 increased from 0.5% to 2%. However, when the silica ratio further elevated from 2% to 4%, the water CA remained nearly unchanged at 160°. The silica ratio and the total consumption of KH1322 plus silica for superhydrophobic surfaces in the present study were much less than those in previous works [29]. The minimum silica ratio used in this work reached as low as 0.5%, and the total consumption per unit area of KH1322 plus silica was only 4 $\text{g}\cdot\text{m}^{-2}$, indicating a low-cost characteristic of the preparation method.

Unlike previously reported method based on silica to prepare the superhydrophobic surface, the silica plays a major role in accelerating the hydrolysis and condensation of KH1322 in this work, rather than building micro-nano morphologies. Therefore, the superhydrophobic surface could be obtained even under a low silica ratio of 0.5%. The detailed reason for the silica ratio affecting the surface wettability can be explained as follows. When the silica particles were added into KH1322 solutions, the hydrolysis of KH1322 was developed more quickly. The hydrophilic molecular chains containing C-O groups reduced and the wood surface was covered by more hydrophobic molecular chains containing Si-O groups, resulting in an increase in the water CAs correspondingly. When the

silica feeding ratio further increased to 2%, almost all $-\text{OC}_2\text{H}_5$ groups from KH1322 were hydrolyzed to generate ethanol, which was completely removed from the wood surface during the drying process, thus the C-O groups could hardly be detected. At this point, the number of hydrophobic groups reached the maximum value. In order to confirm the above assumptions, XPS was used to analyze the element change on the wood surfaces. In Figure 3a, the C 1s XPS broad peak of sanded wood coated with KH1322 and 0.5% SiO_2 can be fitted to four peaks with binding energies of 283.8, 285.6, 287.3 and 290.9 eV, which can be indexed to the functional groups of Si-C, C-C, C-O, and CF_2 , respectively [30]. Here, the ratio of hydrophilic carbons (C-O groups) to all carbon atoms was calculated to be 3.46% based on the peak areas in Figure 3a. However, for the sanded wood coated with KH1322 and 2% silica, the hydrophobic C atoms (Si-C, C-C, and CF_2 groups) can account for nearly 100% of all C atoms. Hence, the additional increase in the silica ratio to 4% no longer increased the ratio of hydrophobic groups, so the water CAs did not increase further.

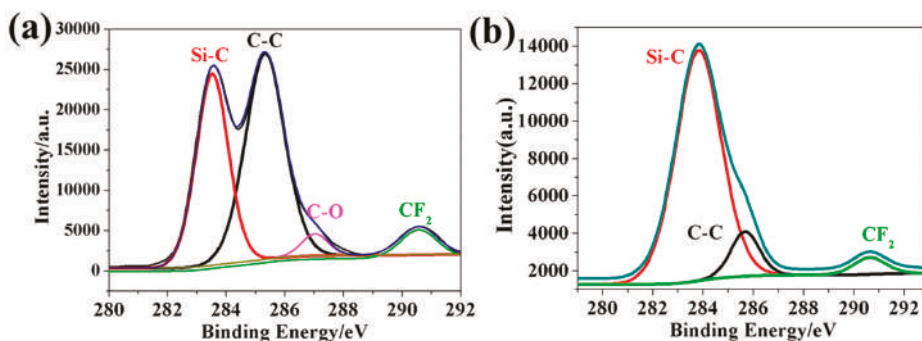


Figure 3. C 1s X-ray photoelectron spectroscopy (XPS) spectra of (a) sanded wood coated with KH1322 and 0.5% SiO_2 and (b) sanded wood coated with KH1322 and 2.0% SiO_2 .

3.3. The Effect of Drying Temperatures on Surface Wettability

Usually, the drying temperature is a key factor that affects the formation of the coating. Therefore, the influence of drying temperature on the surface wettability was also researched. As shown in Figure 4a, the water CA increased from 157° and 160° to 170° with the elevation of the drying temperature from 100°C and 120°C to 130°C . When the drying temperature was increased again to 140°C , the water CA decreased slightly from 170° to 167° . The previous CA increase should result from the reduction of hydrophilic C-O groups. It is believed that the increase in the drying temperature from 100°C to 120°C accelerated the hydrolysis of KH1322. More $-\text{OC}_2\text{H}_5$ groups of KH1322 reacted with the water to release ethanol vapour. Therefore, the hydrophilic C-O groups reduced correspondingly, as illustrated by the diminished peak intensity of C-O groups at 1271 cm^{-1} (Figure 4b). When the drying temperature was further elevated to 130°C , almost all $-\text{OC}_2\text{H}_5$ groups of KH1322 were hydrolyzed to generate ethanol vapour. The virtual disappearance of the C-O signal in Figure 4b demonstrates the removal of more hydrophilic groups. Moreover, the adsorption of hydrophobic groups (Si-O at 810 and 470 cm^{-1}) reached the maximum signal. These facilitate the formation of the superhydrophobic surface with a larger water CA. It could be inferred that the drying temperature of 130°C is high enough to achieve the complete hydrolysis of KH1322. Thus, when the temperature further increased to 140°C , the ratio of hydrophobic groups on the wood surfaces no longer increased, with the result that the water CA would not increase correspondingly.

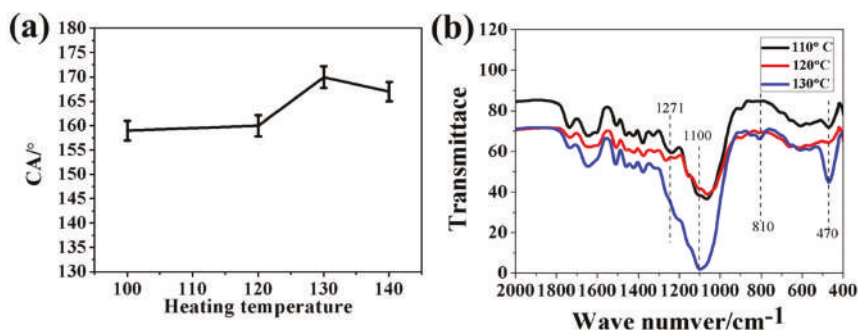


Figure 4. (a) The water contact angles (CAs) of the surfaces of coated sanded wood obtained at different drying temperatures, (b) Comparison of FTIR spectra of sanded woods coated with KH1322 fluoroalkylsilane and silica obtained at different drying temperatures.

Considering that hours of high-temperature drying may induce damages to some wood, the drying at room temperature (25 °C) was also tried to prepare the hydrophobic surface. It was found that the water CA on the as-obtained surface increased from 75° to 155° when the drying time was extended from 2 hours to 8 hours. This result revealed that the fabrication of a superhydrophobic surface on the wood can also be achieved at room temperature when the drying time is long enough. This suggests that the method can be extended to produce superhydrophobic surfaces for thermally unstable wood products.

3.4. Mechanical Robustness and Self-Healing of Superhydrophobic Surfaces

One obstacle to the widespread practical applications of superhydrophobic surfaces is the lack of enough robustness. To investigate the abrasion resistance of the as-obtained superhydrophobic surface, under the loading of 500 grams (pressure: 3.5 KPa), the hydrophobic surface of the coated sanded wood was oriented toward 240-grit sandpaper and moved a distance of 10 cm (each cycle) in a straight line, as shown in Figure 5a. Then, the water CAs of the resulting wood surface were tested. This process was repeated for 45 cycles, and the test results of water CAs were recorded in Figure 5b. One can see that after 45 cycles, the water CA was able to retain a high value of 153°, and the sliding angle was still less than 10°, indicating that the surface of the coated sanded wood maintained its superhydrophobicity. These results demonstrate the satisfactory abrasion resistance of the as-prepared superhydrophobic surface.

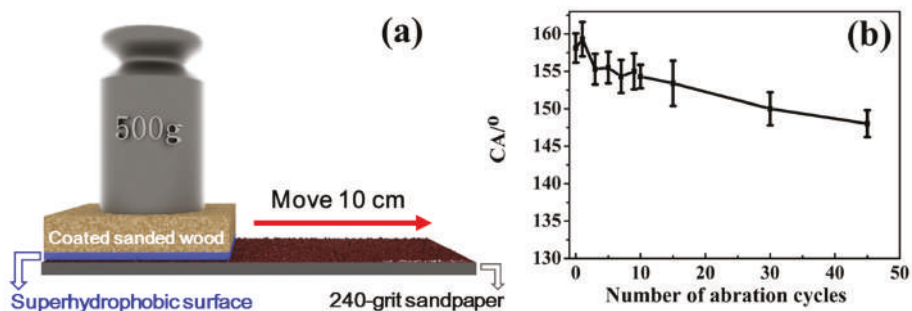


Figure 5. (a) Illustration of the abrasion resistance test for the superhydrophobic surface. (b) Water CAs as a function of the number of abrasion cycles.

As an important indicator affecting service life, the self-healing ability of the superhydrophobic surface was examined by alkali etching. After it was soaked in alkali solution for two hours,

the water CA of the resulting surface decreased from 160° to 0° , indicating that this surface had lost its superhydrophobicity. However, after this damaged surface was exposed in an ambient environment for 8 hours, its water CA and sliding angles returned to 160° and $<10^\circ$, respectively, demonstrating that the original superhydrophobicity of the damaged surface was restored. The recovery of superhydrophobicity should be attributed to the unique inherent porous structure of wood. This intrinsic porous structure can preserve a large number of fluoroalkylsilane moieties as healing agents in wood pores (such as cell cavities and grooves) beneath the superhydrophobic surface. Once the primary top fluoroalkylsilane layer is decomposed or scratched, the internal preserved healing agents in the cell cavities and grooves will migrate to the wood surface (as illustrated by the right part of Scheme 1) to minimize the surface free energy due to the exposure to the hydrophobic air [31,32]. As a result, the superhydrophobicity is healed at room temperature. In this way, the damaged surface recovered its superhydrophobicity at room temperature when the time duration was long enough for the healing agents in pores to migrate onto the wood surface. As displayed in Figure 6a, the etching–healing process can be repeated for nine cycles without decreasing the superhydrophobicity of the self-healed surface. It is believed that the robust internal porous microstructure of wood is essential for the recovery of superhydrophobicity as shown in Figure 6b,c. In addition, it was found that when the temperature increased to 100°C and 140°C , the recovery time of the superhydrophobicity reduced to 2 h and 1 h, respectively. This indicates that this self-healing is temperature-dependent, with a more accelerated self-healing process under higher temperatures and vice versa. At present, the self-healing of the as-constructed superhydrophobic surface can be accomplished at room temperature. Thus, this self-healing can be applied to some wooden decorative materials that are sensitive to heat and ultraviolet radiation. Furthermore, if repeated self-healing runs out of healing agents, the suspension of KH1322 fluoroalkylsilane and silica can be cast and dried onto the surface again to replenish the healing agents.

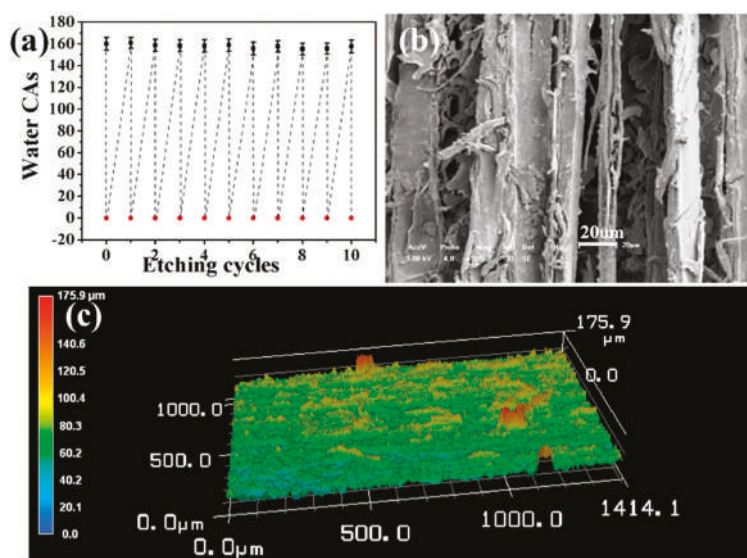


Figure 6. (a) Water CAs of the surface after repeated alkaline etching and self-healing at room temperature. (b) SEM and (c) 3D OPM images of the surface of coated sanded wood after alkaline etching.

3.5. Improvement in Water and Mildew Resistance of Superhydrophobic Surfaces

As a natural biomass material with many hydrophilic groups, raw wood is apt to absorb water and swell in dimension when in contact with water [24]. In order to simulate the rinse effect of rainwater

on the surface of outdoor wood products, the as-obtained superhydrophobic surface of coated sanded wood was washed by running water for 20 minutes (Figure 7a). No residual water can be observed on the superhydrophobic surface after this process (Figure 7b). By contrast, excessive water remained on the surface of raw wood after the same treatment (Figure 7c–d). These results indicate the excellent water resistance of the as-constructed superhydrophobic surface.

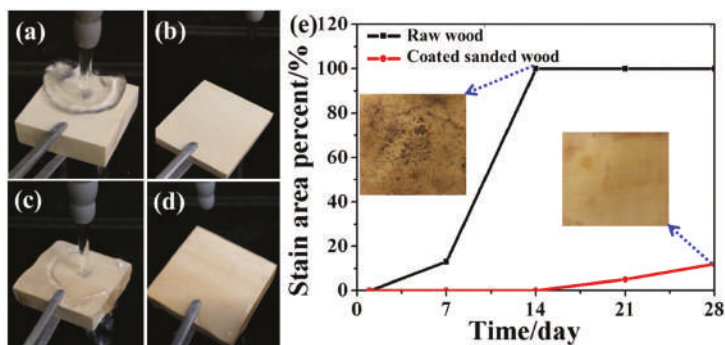


Figure 7. Photographs of the superhydrophobic wood surface (a) during water washing and (b) after water washing. Photographs of the raw wood surface (c) during water washing and (d) after water washing. (e) Comparison of mildew infection on the surface of raw wood and coated sanded wood in a humid environment.

Wood contains protein, starch, cellulose, etc., which can provide nutrients for microbial growth, so it is easily infected by mildew, especially when the wood surface is wet. Here, the mildew resistance ability of the as-prepared superhydrophobic wood surface was studied and compared with that of the raw wood surface. The results in Figure 7e demonstrate that about 13% of the surface area of the raw wood had been infected by mildew on the 7th day when it was placed in an environment with a humidity of 90% and a temperature of 30 °C, and the percentage of the infected area increased to 100% on the 14th day. By contrast, the coated sanded wood with the superhydrophobic surface was not infected by mildew until the 14th day and only 12% of its surface was infected by mildew on the 28th day under the same environment. The improved mildew resistance could be due to the fact that the superhydrophobic surface repelled water and reduced water adsorption thereby inhibiting the growth of mildew. In addition, this surface can maintain its superhydrophobic ability as shown by only minimal contact angle fluctuations (Figure 8) after a long period of high-intensity UV irradiation which demonstrates the fine UV durability of this superhydrophobic surface. Therefore, it is highly promising to employ this superhydrophobic surface to prolong the service life of wood-based materials.

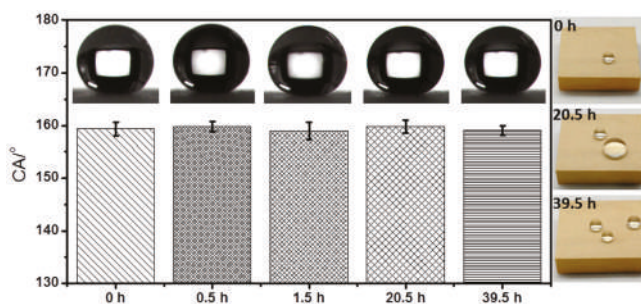


Figure 8. Water CAs and photographs of the coated sanded wood surface after being irradiated with 365 nm UV lamp ($11.6 \text{ mW} \cdot \text{cm}^{-2}$) for different times.

4. Conclusions

In this work, a novel superhydrophobic surface has been fabricated successfully by casting and drying a composite suspension of KH1322 and silica on the modified hierarchical structure of wood. Due to the full use of the natural hierarchical structure of wood, the whole process needs neither complicated equipment nor complex procedures to construct the micro/nano composite structure. Only a very low content of inorganic matter is needed to achieve superhydrophobicity. Furthermore, the fabrication of a superhydrophobic surface can be achieved at room temperature. More importantly, the as-prepared superhydrophobic surface exhibits a satisfactory resistance to abrasion and is able to self-heal at room temperature upon damage. If the healing agents are depleted, the surface can restore its self-healing ability by casting the fluoroalkylsilane/silica composite suspension to replenish the healing agents. When used for wood protection, this superhydrophobic surface greatly improves both mildew inhibition and water resistance of wood, thereby prolonging the service life of wood-based materials. The excellent performance of the as-constructed superhydrophobic surface, the facile and environmentally friendly fabrication process, and the low cost, make this method highly suitable for the protection of various wood-based materials.

Author Contributions: Conceptualization, Z.S.; Data curation, J.W.; Formal analysis, C.M.; Funding acquisition, Z.S. and H.C.; Investigation, J.W., Y.L., Q.C. and C.M.; Methodology, J.W.; Project administration, Z.S. and H.C.; Resources, Q.C. and L.C.; Supervision, Z.S. and H.C.; Validation, L.C.; Visualization, Y.L.; Writing—original draft, Z.S.; Writing—review and editing, H.C. All authors have read and agreed to the published version of the manuscript.

Funding: This work was supported by the Zhejiang Provincial Key Research and Development Project (2019C02037), National Key Project (2017YFD0601105), Zhejiang Provincial Natural Science Foundation of China (LY20E020004), Zhejiang A&F University Scientific Research Training Program for Undergraduates (KX20180113), Jiangsu North Special Project from Jiangsu Suqian (BN2016176), and 151 Talent Project of Zhejiang Province.

Conflicts of Interest: The authors declare no conflict of interest.

References

1. Lu, Y.; Sathasivam, S.; Song, J.; Crick, C.R.; Carmalt, C.J.; Parkin, I.P. Robust self-cleaning surfaces that function when exposed to either air or oil. *Science* **2015**, *347*, 1132–1135. [[CrossRef](#)] [[PubMed](#)]
2. Hou, X.; Hu, Y.; Grinthal, A.; Khan, M.; Aizenberg, J. Liquid-based gating mechanism with tunable multiphase selectivity and antifouling behaviour. *Nature* **2015**, *519*, 70–73. [[CrossRef](#)] [[PubMed](#)]
3. Wu, M.; Ma, B.; Pan, T.; Chen, S.; Sun, J. Silver-nanoparticle-colored cotton fabrics with tunable colors and durable antibacterial and self-healing superhydrophobic properties. *Adv. Funct. Mater.* **2015**, *26*, 569–576. [[CrossRef](#)]
4. Zhang, X.; Li, Z.; Liu, K.; Jiang, L. Bioinspired multifunctional foam with self-cleaning and oil/water separation. *Adv. Funct. Mater.* **2013**, *23*, 2881–2886. [[CrossRef](#)]
5. Ruan, C.; Ai, K.; Li, X.; Lu, L. A Superhydrophobic sponge with excellent absorbency and flame retardancy. *Angew. Chem. Int. Ed.* **2014**, *53*, 5556–5560. [[CrossRef](#)] [[PubMed](#)]
6. Liu, Y.; Wang, X.; Fei, B.; Hu, H.; Lai, C.; Xin, J.H. Bioinspired, Stimuli-responsive, multifunctional superhydrophobic surface with directional wetting, adhesion, and transport of water. *Adv. Funct. Mater.* **2015**, *25*, 5047–5056. [[CrossRef](#)]
7. Hooda, A.; Goyat, M.S.; Pandey, J.K.; Kumar, A.; Gupta, R. A review on fundamentals, constraints and fabrication techniques of superhydrophobic coatings. *Prog. Org. Coat.* **2020**, *142*, 105557. [[CrossRef](#)]
8. Youngblood, J.P.; McCarthy, T.J. Ultrahydrophobic polymer surfaces prepared by simultaneous ablation of polypropylene and sputtering of poly(tetrafluoroethylene) using radio frequency plasma. *Macromolecules* **1999**, *32*, 6800–6806. [[CrossRef](#)]
9. Folkers, J.P.; Laibinis, P.E.; Whitesides, G.M. Self-assembled monolayers of alkanethiols on gold: Comparisons of monolayers containing mixtures of short- and long-chain constituents with methyl and hydroxymethyl terminal groups. *Langmuir* **1992**, *8*, 1330–1341. [[CrossRef](#)]
10. Sharma, A.; Reiter, G. Instability of thin polymer films on coated substrates: Rupture, dewetting, and drop formation. *J. Colloid Interf. Sci* **1996**, *178*, 383–399. [[CrossRef](#)]

11. Shon, Y.-S.; Lee, S.; Colorado, R.; Perry, S.S.; Lee, T.R. Spiroalkanedithiol-Based SAMS reveal unique insight into the wettabilities and frictional properties of organic thin films. *J. Am. Chem. Soc.* **2000**, *122*, 7556–7563. [[CrossRef](#)]
12. Miyauchi, M.; Kieda, N.; Hishita, S.; Mitsuhashi, T.; Nakajima, A.; Watanabe, T.; Hashimoto, K. Reversible wettability control of TiO₂ surface by light irradiation. *Surf. Sci.* **2002**, *511*, 401–407. [[CrossRef](#)]
13. Mutel, B.; Taleb, A.B.; Dessaux, O.; Goudmand, P.; Gengembre, L.; Grimblot, J. Characterization of mixed zinc-oxidized zinc thin films deposited by a cold remote nitrogen plasma. *Thin Solid Films* **1995**, *266*, 119–128. [[CrossRef](#)]
14. Gu, Z.-Z.; Uetsuka, H.; Takahashi, K.; Nakajima, R.; Onishi, H.; Fujishima, A.; Sato, O. Structural color and the lotus effect. *Angew. Chem. Int. Ed.* **2003**, *42*, 894–897. [[CrossRef](#)] [[PubMed](#)]
15. Wang, J.; Wen, Y.; Feng, X.; Song, Y.; Jiang, L. Control over the wettability of colloidal crystal films by assembly temperature. *Macromol. Rapid Commun.* **2006**, *27*, 188–192. [[CrossRef](#)]
16. Wang, J.; Wen, Y.; Hu, J.; Song, Y.; Jiang, L. Fine Control of the wettability transition temperature of colloidal-crystal films: From superhydrophilic to superhydrophobic. *Adv. Funct. Mater.* **2007**, *17*, 219–225. [[CrossRef](#)]
17. Deng, X.; Mammen, L.; Butt, H.J.; Vollmer, D. Candle soot as a template for a transparent robust superamphiphobic coating. *Science* **2012**, *335*, 67–70. [[CrossRef](#)]
18. Deng, X.; Mammen, L.; Zhao, Y.; Lellig, P.; Müllen, K.; Li, C.; Butt, H.J.; Vollmer, D. Transparent, thermally stable and mechanically robust superhydrophobic surfaces made from porous silica capsules. *Adv. Mater.* **2011**, *23*, 2962–2965. [[CrossRef](#)]
19. Latthe, S.; Terashima, C.; Nakata, K.; Sakai, M.; Fujishima, A. Development of sol-gel processed semi-transparent and self-cleaning superhydrophobic coatings. *J. Mater. Chem. A* **2014**, *2*, 5548–5553. [[CrossRef](#)]
20. Geng, Z.; He, J.; Xu, L.; Yao, L. Rational design and elaborate construction of surface nano-structures toward highly antireflective superamphiphobic coatings. *J. Mater. Chem. A* **2013**, *1*, 8721–8724. [[CrossRef](#)]
21. Chen, L.; Sun, X.; Hang, J.; Jin, L.; Shang, D.; Shi, L. Large-scale fabrication of robust superhydrophobic coatings with high rigidity and good flexibility. *Adv. Mater. Interfaces* **2016**, *3*, 1500718. [[CrossRef](#)]
22. Liao, Y.; Zheng, G.; Huang, J.J.; Tian, M.; Wang, R. Development of robust and superhydrophobic membranes to mitigate membrane scaling and fouling in membrane distillation. *J. Membrane Sci.* **2020**, *601*, 117962. [[CrossRef](#)]
23. Kobina Sam, E.; Kobina Sam, D.; Lv, X.; Liu, B.; Xiao, X.; Gong, S.; Yu, W.; Chen, J.; Liu, J. Recent development in the fabrication of self-healing superhydrophobic surfaces. *Chem. Eng. J.* **2019**, *373*, 531–546. [[CrossRef](#)]
24. Shen, Y.; Yitian, W.; Zhehong, S.; Hao, C. Fabrication of Self-healing superhydrophobic surfaces from water-soluble polymer suspensions free of inorganic particles through polymer thermal reconstruction. *Coatings* **2018**, *8*, 144. [[CrossRef](#)]
25. Lewin, M.; Goldstein, I.S. Wood Structure and Composition. *Science* **1991**, *152*, 500–502. [[CrossRef](#)]
26. Barbero-López, A.; Chibily, S.; Tomppo, L.; Salami, A.; Ancin-Murguzur, F.J.; Venäläinen, M.; Lappalainen, R.; Haapala, A. Pyrolysis distillates from tree bark and fibre hemp inhibit the growth of wood-decaying fungi. *Ind. Crop. Prod.* **2019**, *129*, 604–610. [[CrossRef](#)]
27. Wenzel, R.N. Resistance of solid surfaces to wetting by water. *Ind. Eng. Chem.* **1936**, *28*, 988–994. [[CrossRef](#)]
28. Cassie, A.B.D.; Baxter, S. Wettability of porous surfaces. *Trans. Faraday Soc.* **1944**, *40*, 546–551. [[CrossRef](#)]
29. Fu, Q.; Wu, X.; Kumar, D.; Ho, J.W.; Kanhere, P.D.; Srikanth, N.; Liu, E.; Wilson, P.; Chen, Z. Development of sol-gel icephobic coatings: Effect of surface roughness and surface energy. *ACS Appl. Mater. Interfaces* **2014**, *6*, 20685–20692. [[CrossRef](#)]
30. Esteves, A.C.C.; Luo, Y.; van de Put, M.W.P.; Carcouët, C.C.M.; With, G.D. Self-replenishing dual structured superhydrophobic coatings prepared by drop-casting of an all-in-one dispersion. *Adv. Funct. Mater.* **2014**, *24*, 986–992. [[CrossRef](#)]

31. Wang, H.; Xue, Y.; Ding, J.; Feng, L.; Wang, X.; Lin, T. Durable, Self-healing superhydrophobic and superoleophobic surfaces from fluorinated-decyl polyhedral oligomeric silsesquioxane and hydrolyzed fluorinated alkyl silane. *Angew. Chem. Int. Ed.* **2011**, *50*, 11433–11436. [[CrossRef](#)] [[PubMed](#)]
32. Li, Y.; Chen, S.; Wu, M.; Sun, J. All spraying processes for the fabrication of robust, self-healing, superhydrophobic coatings. *Adv. Mater.* **2014**, *26*, 3344–3348. [[CrossRef](#)] [[PubMed](#)]



© 2020 by the authors. Licensee MDPI, Basel, Switzerland. This article is an open access article distributed under the terms and conditions of the Creative Commons Attribution (CC BY) license (<http://creativecommons.org/licenses/by/4.0/>).

Article

Pyrolytic Kinetics of Polystyrene Particle in Nitrogen Atmosphere: Particle Size Effects and Application of Distributed Activation Energy Method

Lin Jiang¹, Xin-Rui Yang¹, Xu Gao¹, Qiang Xu¹, Oisik Das², Jin-Hua Sun^{3,*} and Manja Kitek Kuzman⁴

¹ School of Mechanical Engineering, Nanjing University of Science and Technology, Nanjing 210094, China; ljiang@njust.edu.cn (L.J.); yxr1994@njust.edu.cn (X.-R.Y.); gaouxu@njust.edu.cn (X.G.); xuqiang@njust.edu.cn (Q.X.)

² The Division of Material Science, Department of Engineering Sciences and Mathematics, Luleå University of Technology, 97187 Luleå, Sweden; oisik.das@ltu.se

³ State key laboratory of Fire Science, University of Science and Technology of China, Hefei 264000, China

⁴ Department of Wood Science and Technology, Biotechnical Faculty, University of Ljubljana, Jamnikarjeva 101, 1000 Ljubljana, Slovenia; manja.kuzman@bf.uni-lj.si

* Correspondence: sunjh@ustc.edu.cn; Tel.: +86-551-63606425

Received: 11 December 2019; Accepted: 8 February 2020; Published: 12 February 2020

Abstract: This work was motivated by a study of particle size effects on pyrolysis kinetics and models of polystyrene particle. Micro-size polystyrene particles with four different diameters, 5, 10, 15, and 50 μm , were selected as experimental materials. Activation energies were obtained by isoconversional methods, and pyrolysis model of each particle size and heating rate was examined through different reaction models by the Coats–Redfern method. To identify the controlling model, the Avrami–Eroféev model was identified as the controlling pyrolysis model for polystyrene pyrolysis. Accommodation function effect was employed to modify the Avrami–Eroféev model. The model was then modified to $f(\alpha) = n\alpha^{0.39n - 1.15}(1 - \alpha)[-\ln(1 - \alpha)]^{1 - 1/n}$, by which the polystyrene pyrolysis with different particle sizes can be well explained. It was found that the reaction model cannot be influenced by particle geometric dimension. The reaction rate can be changed because the specific surface area will decrease with particle diameter. To separate each step reaction and identify their distributions to kinetics, distributed activation energy method was introduced to calculate the weight factor and kinetic triplets. Results showed that particle size has big impacts on both first and second step reactions. Smaller size particle can accelerate the process of pyrolysis reaction. Finally, sensitivity analysis was brought to check the sensitivity and weight of each parameter in the model.

Keywords: particle size; model free; model fitting; avrami–eroféev; DAEM

1. Introduction

To meet the needs of society, various kinds of advanced materials with different functions have been invented and updated greatly. In the ultrafine materials research area, researchers have tried to generate particles with even smaller diameters. After a normal particle is processed by ultrafine technology, particles will own some unique characteristics, including large specific surface area and high chemical activity. The peculiar physical and chemical characteristics make ultrafine particles the focus of advanced materials nowadays. During the processes of particles' industrial manufacture, storage, and transportation, particles with different sizes behave differently when considering their safety concerns. Therefore, particle size effects are essential influence factors needed to be considered when researchers explore particle thermal safety problems. The chemical kinetics and reaction model can be greatly influenced by particle size [1]. After the block is processed by ultrafine processing technology,

particle specific surface area can be greatly increased, which can influence combustible pyrolysis and reaction rates when heating, and even the reaction model and products can be changed [2,3].

So, the work reported here was motivated by a study of particle size effects on pyrolysis behavior, chemical kinetics, and reaction model when surrounded with heating. Micro-size polystyrene particles with four different diameters were selected as typical particle materials. Activation energies were obtained by several different isoconversional methods. The pyrolysis model of each particle size and heating rate was examined by nineteen different reaction model candidates by the Coats–Redfern methods, among which the three best models were then selected, and the reaction model function was then reconstructed by selected models. The particle size effects on kinetics and reaction model could be concluded. To separate step reactions from whole reaction and identify their distributions to kinetics, a distributed activation energy method was then introduced to calculate the weight factor and kinetic triplets.

2. Literature Review

Polystyrene is a commonly-used polymer material in daily life, which is usually employed as thermal insulation materials in extruded or expandable formation, whose kinetics and reaction mechanism have been studied. Jiao et al. studied the kinetics and volatile products of expandable polystyrene and extruded polystyrene with TGA and TGA-MS-FTIR, respectively. They found that the activation energies with conversions of expandable polystyrene are a little higher than extruded polystyrene, which means expandable polystyrene is a little more stable than the extruded one. During the pyrolysis process, small molecules including CO, C₂H₃, C₂H₅, and phenyl were detected [4]. After this, Jiao and Sun explored the reaction mechanism of polystyrene during the pyrolysis process. It was found that two pyrolysis reactions exist during the whole heating process. One is the small pyrolysis of styrene monomers around 275 °C, and the other is breakage of the main chain and large amounts of styrene generation around 430 °C [5]. Cheng et al. compared the thermal degradation behaviors of micron polymethyl methacrylate (PMMA) and polystyrene (PS) by a traditional kinetics method. They found that the particle size diameters can result in the decrease of activation energies, but have no obvious influence on pre-exponential factors [6]. Other researchers have conducted related studies about particle size effects on material pyrolysis behavior. Shen et al. [7] investigated the wood particle size effects on the yield of bio-oil production. Results showed that the yield of bio-oil production can decrease with the particle size increasing, among which the light bio-oil fractions increased and the heavy bio-oil decreased. Marcilla et al. [8] tested different sizes milled powders of almond shells and olive stones. They found that the milling process can provoke the structure damage of both biomasses, and thus cause the difference in thermal behavior. Also, the milling process may cause the increase of mineral substance. Blasi [9] investigated the particle size and heating rate effects on cellulose pyrolysis by means of a computational model. Three main regimes of particle sizes were found to control pyrolysis processes, including thermally thick, thermally thin, and pure kinetic control, which were adjudged by particle size and heating rate conditions. Hanson [10] studied particle size effects on pyrolysis of coal, and found that a smaller particle was more likely to produce char residue larger than itself. For larger particle pyrolysis, it is more likely to produce a fragment. Yu et al. [11] ground the coal sample by a planetary ball mill, and the coal samples were classified into three groups according to different ground particle sizes. They found that particles with different sizes contain different carbon and ash contents, which is resulted by the characteristics of coal's uneven texture and solidity.

Most selected samples of previous pyrolysis studies relating particle size effects were self-ground in the laboratory, among which biomass and coal were mostly employed. During the grinding process, it is hard to form particles with uniform shape and component, as these solids have uneven density and distribution. This can result in that the particles employed in thermal analysis experiments do not have uniform distribution, which can definitely cause thermal analysis profiles fluctuations and bad data repeatability. In this study, the polystyrene sample we used was produced by Suzhou Nanomicro Technology Co., Ltd. The particles were produced with uniform shape and diameter, the

diameters of which were 5, 10, 15, and 50 μm. Uniform diameter can guarantee the veracity and reliability of experimental results. More details about experimental sample particle size can be found in Section 4. Most publications including the above reviewed ones preferred to employ a traditional kinetics method when dealing with polymer pyrolysis kinetics problems. However, for the case of polymer pyrolysis, there must be more than one reaction during the pyrolysis procedure. So, in this study, after the traditional kinetics analysis we will introduce distributed activation energy model to explore PS pyrolysis kinetics to distinguish the weight of each sub reaction.

3. Traditional Kinetic Methods

Thermogravimetric analysis (TGA) apparatus can heat the sample with a fixed heating rate and gas flow to blow off the volatiles, and record the instant mass loss. The mass conversion at a certain time can be calculated by instant mass loss divided by total mass loss. The pyrolysis reaction can be expressed by the arithmetic product of two functions, including reaction rate constant and reaction model,

$$d\alpha/dt = A \exp[-E_a/(RT)]f(\alpha) \tag{1}$$

where A , E_a , and R are the pre-exponential factor, the apparent activation energy, and the gas constant, respectively. By TGA testing technique and kinetics calculation methods, the kinetic details can be obtained by measurement and parameterization. After processing natural logarithm to both sides of Equation (1) and then integrating, the reaction rate can yield to

$$g(\alpha) = \frac{A}{\beta} \int_{T_0}^T \exp(-\Delta E_a/RT) dT \tag{2}$$

in which the temperature part has no analytical solution. β means heating rate and equals to dT/dt . Many researchers have tried to solve the integration with reasonable approximations, commonly used methods like KAS [12,13], FWO [14,15], and Tang et al. [16,17] methods, among which different approximation solutions were employed to Equation (2) as listed in Table 1.

Table 1. Three commonly used isoconversional methods for activation energy calculation.

Methods	Expression	Description
Flynn–Wall–Ozawa method	$\log\beta = \log(AE_a/Rg(\alpha)) - 2.315 - 0.4567E_a/RT$	Modified general isoconversional equation by Doyle approximation.
Kissinger–Akahira–Sunose	$\ln(\beta/T^2) = \ln(AR/E_a g(\alpha)) - E_a/RT$	Modified general isoconversional equation by Coats–Redfern approximation.
Tang et al.	$\ln(\beta/T^{1.894661}) = \ln[AE_a/Rg(\alpha)] + 3.635041 - 1.894661\ln E_a - 1.001450E_a/RT$	Tang et al. proposed an improved approximation for temperature integral.

Solved by numerical integration, kinetics parameters can be calculated more accurately with appropriate approximations. Vyazovkin et al. [18–20] developed an advanced isoconversional method which contains the temperature integration.

$$I(E_\alpha, T_\alpha) = \int_0^{T_\alpha} \exp\left(\frac{-E_a}{RT}\right) dT \tag{3}$$

$$I = \frac{E_a}{R} p(x) \tag{4}$$

Then the Vyazovkin method equation can be expressed as Equations (3) and (4), where x equals to E_a/RT . At a certain conversional extent, the value of apparent activation can be identified by minimizing the following formula,

$$\Omega(E_a) = \sum_{i=1}^n \sum_{j \neq i}^n \frac{I(E_{a,i}, T_{a,i}) \beta_j}{I(E_{a,j}, T_{a,j}) \beta_i} \quad (5)$$

The temperature integration can be calculated after a series of transforms. Farjas and Roura [21] derived the six-order Padé approximation, which can give an absolute error less than 10^{-16} for $x > 12$

$$p(x) \approx \frac{\exp(-x)}{x} \times \left(\frac{x^5 + 40x^4 + 552x^3 + 3168x^2 + 7092x + 4320}{x^6 + 42x^5 + 630x^4 + 4200x^3 + 12600x^2 + 15120x + 5040} \right) \quad (6)$$

By Equations (3)–(6), for each conversion the minimization value can be obtained, by this method, a relative dependency between activation energy and conversion range can be obtained.

Model fitting method is a reaction model exploring method using well-known different theoretical reaction models to fit experimental α - T profiles, meanwhile for each model a set of activation energy and pre-exponential factor can be obtained. The Coats–Redfern method is one commonly used model-fitting method, which explores the asymptotic series expansion with the following formula,

$$\ln \frac{g(\alpha)}{T^2} = \ln \left(\frac{AR}{\beta E_a} \left[1 - \left(\frac{2RT^*}{E_a} \right) \right] \right) - \frac{E_a}{RT} \quad (7)$$

where $g(\alpha)$ is the integral form of the reaction model as shown in Table 1, and T^* is the average temperature during all the heating process. For each reaction model as listed in Table 1, plotting $\ln[g(\alpha)/T^2]$ vs. $1/T$ can obtain sets of activation energy and pre-exponential factor. The model which has the best linearity with experimental profile is considered as the real reaction model.

There are nineteen commonly used reaction models in a kinetics area [5,6]. Each model will be used to fit the experimental formation with the obtainment of activation energy and pre-exponential factor. Then according to the fitness of experimental data and theoretical model calculation, one correlation coefficient can be obtained. So, for all nineteen models, there must exist one maximum correlation coefficient. In previous studies, usually the model with the maximum coefficient is identified as the ideal reaction model. However, sometimes the model with the maximum coefficient may be not the real reaction model, which can be checked by model reconstruction with experimental data. So, this model reconstruction [22–26] should be further processed to check if the obtained model can fit experimental profile well, and which procedure is necessary, but is usually ignored in previous related literatures.

The compensation effects means that there must exist one relation between the kinetics parameters that the change of activation energy causing a linear variation of the natural logarithm of the pre-exponential factor. The change of activation energy can be caused by the heating rate or model selection; however, they must be limited to one reaction. When several models are used in the same heating rate, several sets of activation energies and pre-exponential factors can be obtained, then the kinetics compensation effects can be created. The compensation effects between kinetics parameters can be expressed by the following formula,

$$\ln A_i = a + bE_i \quad (8)$$

where i means that the kinetic parameters are obtained from the i -th model, and parameters a and b are kinetics compensation parameters.

All models listed can be examined by Coats–Redfern method, by which nineteen corresponding sets of kinetics parameters can be obtained. Then the calculated activation energy and the pre-exponential factor can be used to evaluate the compensation effect formula parameters a and b . Based on the obtained compensation effects formula, the pre-exponential factor at each conversional extent can be evaluated according to the activation energies obtained by isoconversional methods.

4. Distributed Activation Energy Method

The kinetics methods introduced above belong to traditional kinetics methodology, which usually regards the pyrolysis reaction as one overall reaction, and the activation energy at a certain conversion extent is regarded as global activation energy. However, for polymer pyrolysis reaction, it is unreasonable to take one overall pyrolysis as one step reaction. Considering this reason, distributed activation energy method (DAEM) is adopted to separate the total reaction into several parallel reactions, which was originally adopted to separate the sub-reactions of biomass and coal [27–30]. The idea of distributed activation energy was firstly brought up by Vand [31], and then was developed to solve the pyrolysis problem of coal by Pitt [32].

DAEM assumes that the total reaction can consist of several parallel reaction groups. For each reaction group, it has its own sets of reactions on a molecular level. The decomposition reaction on molecular level can be expressed as,

$$d\left(\frac{m_i(t)}{m_i^*}\right)/dt = A_i \exp\left(\frac{-E_i}{RT}\right)\left(\frac{m^* - m_i(t)}{m_i^*}\right) \quad (9)$$

where i means the i_{th} molecular level reaction, $m_i(t)$ means the volatile mass fraction at time t , m_i^* means the total volatile mass fraction, A_i and E_i are the kinetic parameters for this reaction.

Integrating Equation (9) and assuming that the species i is one of the pool reaction group of component j , then we have the following expression of degradation of component j ,

$$\alpha_j = 1 - \int_0^\infty \exp\left[-\int_{T_0}^T \frac{A_j}{\beta_j} \exp\left(-\frac{E_i}{RT}\right)dT\right] f(E)dE \quad (10)$$

$$\frac{d\alpha_j}{dT} = \int_0^\infty \frac{A_j}{\beta_j} \exp\left[-\frac{E_i}{RT}\right] - \int_{T_0}^T \frac{A_j}{\beta_j} \exp\left(-\frac{E_i}{RT}\right)dT] f(E)dE \quad (11)$$

α_j means the conversion of component j . $f(E)$ means that the group reaction in component j follows the distribution functions $f(E)$, among which Gaussian distribution function is the earliest and most extensive applied one. The Gaussian distribution can be expressed as

$$f_G(E) = \frac{1}{\sigma \sqrt{2\pi}} \exp\left(-\frac{(E - E_0)^2}{2\sigma^2}\right) \quad (12)$$

where the distribution has the center at E_0 and the standard deviation σ . The random distribution is distributed symmetrically at the left and right sides of E_0 . For Gaussian distribution, the range between $E_0 - 1.5\sigma$ and $E_0 + 1.5\sigma$ covers 99.7% random distribution. In this study, we consider 60 times standard deviation, which means the integration of Gaussian distribution ranges from $E_0 - 30\sigma$ and $E_0 + 30\sigma$. All equations about DAEM have temperature integration, which cannot be solved accurately in Equations (10)–(12). So, an approximation about temperature integration is also recommended here, here we calculate $p(x)$ the same as Equation (6). By calculating the j_{th} component DAEM mass loss rate, the overall reaction formula can be calculated as a linear reaction combination of all components,

$$\alpha = \sum_{j=1}^M c_j \alpha_j \quad (13)$$

$$d\alpha/dT = \sum_{j=1}^M c_j (d\alpha/dT)_j \quad (14)$$

where c_j means a weight factor equaling to the amount of volatiles formed from the j_{th} pseudo-component decomposition. It should be noted that Gaussian distribution is a symmetric

distribution centered at E_0 from the shape of the curve. The distributed activation energy assumed that the total pyrolysis reaction is made of multiple parallel reactions, which is a reasonable assumption for polymer degradation.

5. Experimental

Micro polystyrene particles were provided by Nano-Micro Technology Co., Ltd., Suzhou, China. Four available diameters, 5, 10, 15, and 50 μm , were selected. All particles showed uniform size according to the scanning electron microscopy examining figures (<http://en.nanomicrotech.com/>). Furthermore, the particle size was double checked by a Laser Diffraction Particle Size Analyzer, SALD-2300, produced by Shimadzu Corporation, Kyoto, Japan. Particle size was identified by the light intensity distribution pattern of scattered light that is irradiated from sample particle surface when laser lights radiate them. The particle size diameters for four particle sizes are shown in Figure 1.

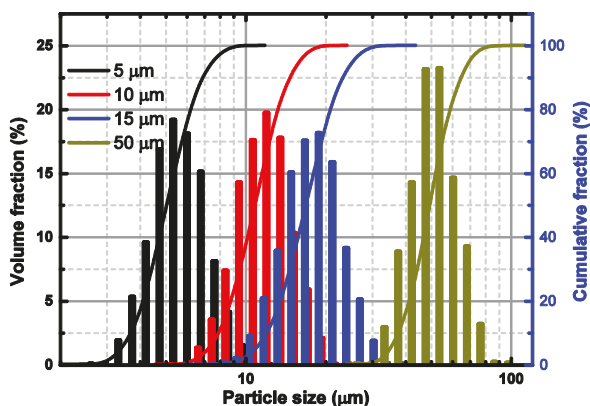


Figure 1. Particle size diameters of polystyrene particles with four different sizes, 5, 10, 15, and 50 μm .

The thermal degradation experiments were conducted on SDT Q600 instrument by TA Instruments (New Castle, USA). Experiments were performed in nitrogen atmosphere with 40 mL min^{-1} flow rate as purge gas and 20 mL min^{-1} as protective gas. Samples were heated in TGA with four heating rates, 3, 5, 7.5, and $10 \text{ K}\cdot\text{min}^{-1}$ from ambient temperature to $850 \text{ }^\circ\text{C}$. An initial sample weight around 3 mg was guaranteed for all testing.

6. Results and Discussion

6.1. Pyrolytic Characteristics Observations

Figure 2 shows the TGA and Differential thermogravimetry (DTG) profiles of polystyrene with four different sizes in nitrogen atmosphere. Detailed thermal pyrolysis temperatures are listed in Table 2. We can find that the pyrolysis profiles of polystyrene with different sizes show similar variations. The DTG curve shows an obvious single peak, which can be identified as a one step reaction. In nitrogen atmosphere, the percentage of heat loss keeps around $90.71 \pm 0.80\%$ constantly. From the TGA and DTG curves, we can find that sample sizes cannot cause the change of the reaction process or TGA profiles obviously.

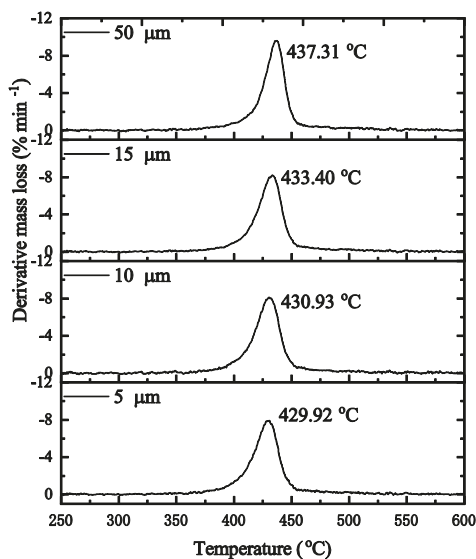


Figure 2. Differential thermogravimetry (DTG) profiles of polystyrene pyrolysis in nitrogen atmosphere at $3 \text{ K}\cdot\text{min}^{-1}$ for 5, 10, 15, and $50 \mu\text{m}$ particle sizes.

Table 2. Characteristic temperature T_0 , T_p and T_f for polystyrene pyrolysis determined from thermogravimetric analysis (TGA) profiles at different heating rates.

β ($^{\circ}\text{C}\cdot\text{min}^{-1}$)	T_0 ($^{\circ}\text{C}$)	T_p ($^{\circ}\text{C}$)	T_f ($^{\circ}\text{C}$)	α_{max}
5 μm				
3	367	430	535	91
5	351	438	545	92
7.5	369	443	528	91
10	349	447	530	92
10 μm				
3	378	431	572	92
5	378	437	531	91
7.5	381	458	528	90
10	379	460	534	91
15 μm				
3	368	433	524	90
5	369	440	534	91
7.5	386	446	529	90
10	382	449	529	91
50 μm				
3	375	437.31	537.50	90
5	381	444.23	534.04	90
7.5	385	451.87	530.90	89
10	359	455.82	535.81	90

For all the samples with different sizes, DTG curves show similar variations with one single peak, as the particles are produced from the same assignment. With the increase of particle size from 5 to $50 \mu\text{m}$, the peak temperature increased monotonically. The $5 \mu\text{m}$ particle shows the minimum pyrolysis peak temperature and onset temperature, and $50 \mu\text{m}$ shows the maximum temperatures. For

a polystyrene particle with a smaller diameter, it has a larger specific surface area, which means for the same sample masses, a smaller particle has more surface heated than a larger particle. For the TGA experiments in this study, we controlled all testing at the same weight at around 3 mg. Then for the 5 μm particle, its specific surface area is 10 times larger than 50 μm particle. Large specific surface area results in faster heat transfer and shorter time to trigger reaction.

6.2. Kinetics Parameters

The activation energies of polystyrene with four different sample sizes were calculated by five different commonly used isoconversional methods. Then, the dependences of activation energies on conversional extent for different calculated methods can be obtained. Figure 3a shows the activation energy calculation results based on different calculation methods. Five curves show the same variation with increasing conversional extent while Friedman results showed different variation from four other methods. The main reason that caused the deviation by the Friedman method with others is data noise brought during data differential process by total mass to use da/dt , while the other four methods do not need a derivation step [33–35]. So FWO, KAS, Tang et al., and advanced Vyazovkin methods show almost the same calculation values, which proved the accuracy of the method calculation.

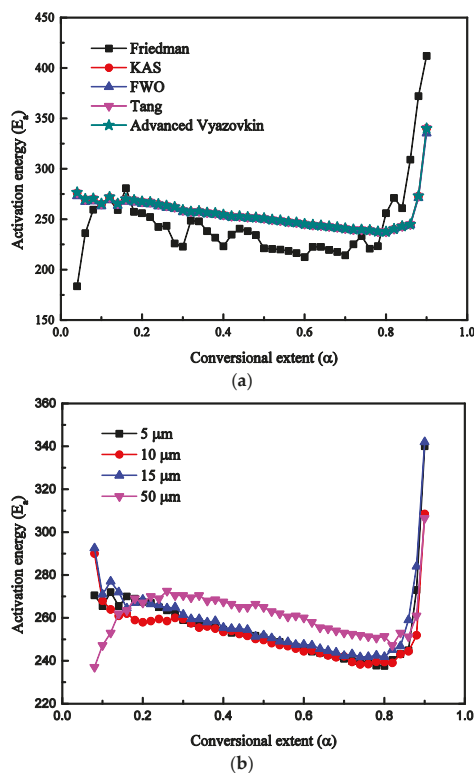


Figure 3. (a) Dependencies of the activation energy on extent of polystyrene conversion determined by five iso-conversional methods including KAS, FWO, Tang, Friedman, and advanced Vyazovkin methods. (b) Dependencies of the activation energy on conversional extent of four different size polystyrene determined by Vyazovkin methods.

Figure 3b shows the dependencies of activation energies on conversional extent for four different polystyrene particle sizes. The activation energy results were calculated by the advanced Vyazovkin

method. The advanced isoconversional method developed by Vyazovkin is a commonly used thermal kinetics method, which excluded the influences of reaction model and needs for differential data to obtain activation energies. From Figure 3b, we can find that the variation tendencies are the same. During the conversional extent 0–0.2, the activation energies fluctuate significantly because a small amount of styrene molecules pyrolyzes and escapes from the main chain. During the conversional extent 0.2–0.85, four size samples show the same variation tendencies. With the increase of conversional extent, the activation energies of all four samples decrease almost linearly, which stage corresponds to the pyrolysis of polystyrene main body. When $\alpha > 0.85$, the activation energies increase rapidly with the increase of conversional extent. During this extent, the mass loss is mainly composed by polystyrene residue, which is hard to pyrolyze continuously and results in a rapid increase of activation energy.

During the main pyrolysis stage, with the increase of conversional extent, activation energies decrease slowly and linearly for all four sizes of samples. The activation energies of 5 and 10 μm are very close to each other for each conversional extent, both of which are smaller than activation energies of 15 μm particle size. The 50 μm size particle shows the maximum activation energies compared with another three sizes, which means that the reaction of 50 μm is the hardest to trigger. This difference on kinetics is mainly caused by their different specific surface area. For all four samples, 50 μm particle sample has the smallest specific surface area, therefore it has the maximum activation energies. The specific surface area of 5 μm particle size is 10 times than 50 μm particle size.

6.3. Model Fitting Method and Compensation Effects

By the isoconversional method calculation, we learned that the main pyrolysis stage ($\alpha = 0.2\text{--}0.85$) of four sample sizes has constant activation energies where one existing reaction model may fit well. Isoconversional methods can only calculate the activation energies at a certain conversional extent, but fail to obtain the reaction model. With employment of the Coats–Redfern method, experimental data for four particle sizes can fit with all nineteen models. Then for each tested model, one set of activation energy and pre-exponential factor can be obtained. Three models with best linear coefficients for four sample sizes and heating rates are selected to list in Table 3, considering the linearity coefficient and activation energy appropriateness.

Table 3. Activation energies, pre-exponential, and corresponding linearity coefficient calculated by Coats–Redfern method for the three best models.

	3 °C min ⁻¹				5 °C min ⁻¹				7.5 °C min ⁻¹				10 °C min ⁻¹			
	Model	lnA	Ea	r ²	Model	lnA	Ea	r ²	Model	lnA	Ea	r ²	Model	lnA	Ea	r ²
5 μm	8	73.17	462.33	0.998	8	73.54	466.64	0.999	8	70.47	451.10	0.999	8	66.29	426.76	0.998
	12	45.99	304.33	0.998	12	46.41	307.16	0.999	12	44.47	296.76	0.998	12	41.76	280.52	0.998
	13	32.32	225.33	0.998	13	32.75	227.42	0.999	13	31.39	219.59	0.998	13	29.41	207.40	0.998
10 μm	8	75.06	469.28	0.990	8	71.09	448.69	0.988	8	71.57	453.59	0.987	8	68.97	439.20	0.988
	12	47.26	308.99	0.990	12	44.76	295.22	0.987	12	45.22	298.44	0.986	12	43.56	288.83	0.988
	13	33.28	228.84	0.989	13	31.52	218.48	0.987	13	31.95	220.87	0.986	13	30.77	213.65	0.987
15 μm	8	76.54	478.30	0.993	8	74.02	466.03	0.993	8	72.31	458.14	0.992	8	69.84	444.63	0.992
	12	48.26	315.00	0.993	12	46.73	306.77	0.992	12	45.71	301.48	0.992	12	44.15	292.45	0.992
	13	34.03	233.35	0.992	13	33.00	227.15	0.992	13	32.32	223.15	0.992	13	31.22	216.36	0.992
50 μm	8	80.36	502.22	0.989	8	77.78	489.67	0.984	8	76.64	485.47	0.983	8	75.33	478.41	0.983
	12	50.81	330.93	0.987	12	49.24	322.52	0.984	12	48.61	319.68	0.982	12	47.82	314.95	0.982
	13	35.96	245.28	0.988	13	34.89	238.94	0.983	13	34.51	236.78	0.982	13	33.99	233.22	0.981

Models 8, 12, 13 means first order model, Avrami–Eroféev model ($n = 1.5$), and Avrami–Eroféev model ($n = 2$).

From the kinetics calculation results listed in Table 3, we can see that the kinetics triplet calculations are greatly dependable on the model selection. The activation energies calculated by Model 13 are around 225 $\text{kJ}\cdot\text{mol}^{-1}$, while for Model 8, the calculation result is around 463 $\text{kJ}\cdot\text{mol}^{-1}$. From Table 3, we can find that for all cases of each particle size and heating rate, the best three models are the same, i.e., first-order model (F1), Avrami–Eroféev (A3/2), and Avrami–Eroféev (A2). All three models show good linearity, larger than 0.98. However, the A3/2 and A2 models are more reasonable than the F1 model because the activation energies obtained by Avrami–Eroféev are closer to the results by isoconversional

methods. Also, the experimental $f(\alpha)$ shows an increase first then decrease variation, whose variation tendency only fits the Avrami–Eroféev model. Although the dimensional diffusion model has the similar variation, its magnitude is too small to fit with experimental results.

Calculation of activation energy at each conversional extent allows the reconstruction of the pyrolysis model, which acquires pre-exponential knowledge in advance. For one fixed reaction at one known heating rate, the activation energies have a linear relation with natural logarithm of the pre-exponential factor called compensation effect, which can be expressed as $\ln A_j = a + bE_j$, where a and b are constants for one reaction, $a = \ln k_{iso}$ and $b = 1/RT_{iso}$. k_{iso} is called artificial isokinetic rate and T_{iso} is defined as artificial isokinetic temperature. The subject j means the selected model. If the model we employed in calculation is not appropriately hypothesized, then the kinetic parameter artificial isokinetic temperature may locate out of the experimental temperature.

For each model, one set of kinetic parameters can be calculated. Then all the kinetics parameters can be used for modelling compensation effects, as listed in Table 4. Results showed that all the heating rates for each particle size have good linearity, as shown in Figure 4, which allows for the prediction of the pre-exponential factor at each conversional extent.

Table 4. The values of k_{iso} and T_{iso} by model fitting methods for pyrolysis of polystyrene particles with four sizes.

Particle Size	3 K min ⁻¹		5 K min ⁻¹		7.5 K min ⁻¹		10 K min ⁻¹	
	k_{iso}	T_{iso}	k_{iso}	T_{iso}	k_{iso}	T_{iso}	k_{iso}	T_{iso}
5 μm	0.001446	704.10	0.002360	711.74	0.003338	719.24	0.004233	722.76
10 μm	0.001407	697.77	0.002181	705.57	0.003241	712.49	0.004162	716.62
15 μm	0.001447	698.59	0.002301	706.27	0.003332	713.09	0.004265	717.20
50 μm	0.001482	701.24	0.00233	708.72	0.003393	715.68	0.004423	719.17

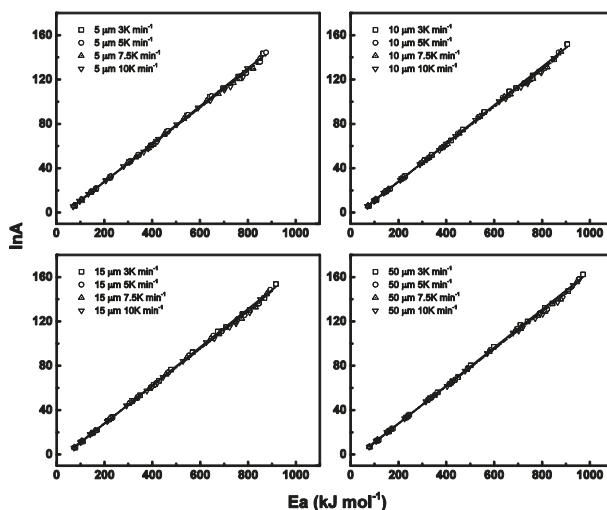


Figure 4. The isokinetic relationships ($\ln A$ vs. E_a) obtained during degradation process using Coats–Redfern method for different particle sizes and heating rates.

6.4. Numerical Reconstruction

In Section 6.2, the activation energies at each conversional extent were obtained by isoconversional methods. Then, nineteen models were checked by the Coats–Redfern method to obtain a reasonable model describing polystyrene particle pyrolysis for cases of four different particle sizes. Avrami–Eroféev models (both A3/2 and A2) showed high linearity to the fitting with experimental profiles. Based on

kinetic triplet results by different models, compensation effects could be employed to create numerical connection between activation energies and the pre-exponential factors, by which the pre-exponential factor at each conversional extent can also be clear. Based on the obtained pre-exponential factor on conversional extent, the calculated reaction model function can be obtained and compared with the theoretical reaction model function to examine the validity of the reaction model.

For all nineteen models, only the Avrami–Eroféev model can fit with experimental data during all conversional ranges; however, the results are still unsatisfactory to fit all heating rates well. This is because the most universally employed model in thermal kinetics is not applicable for reactions in/on media that are solid or porous structured [36]. So, when the pyrolysis kinetics are being described and refitted accurately, one accommodation function should be introduced to modify the model based on its known function. The real reaction model can be calculated by the arithmetic products of two functions, one is the accommodation function which can be expressed by α^m , and the other is a classical reaction model. The new kinetics model after modification can be expressed by

$$f(\alpha) = n\alpha^m(1 - \alpha)[- \ln(1 - \alpha)]^{1 - 1/n} \tag{15}$$

Figure 5 shows the comparisons of experimental $f(\alpha)$ points during all conversional ranges with theoretical profiles based on Equation (15) for four particle sizes. Results show that the experimental and theoretical data can match reasonably well during all conversional extents with two parameters m and n to describe the reaction model.

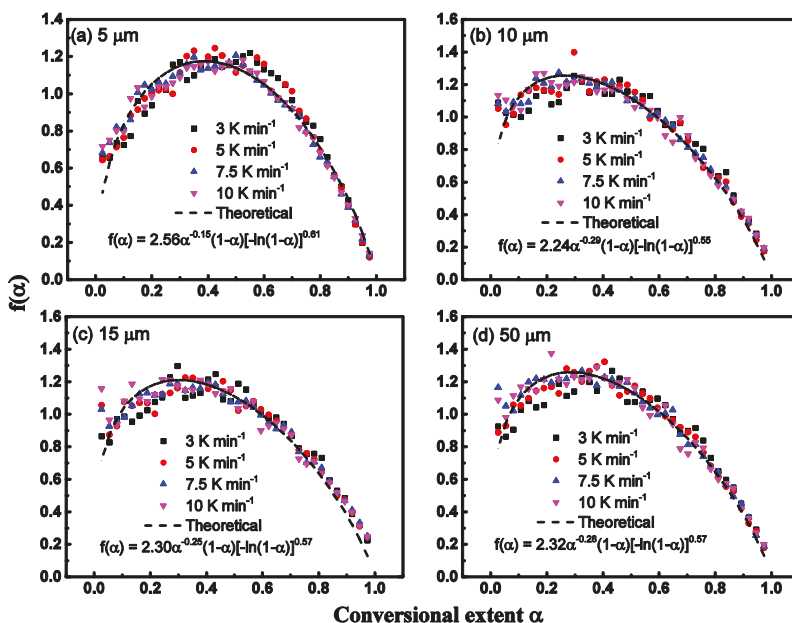


Figure 5. The experimental kinetics function $f(\alpha)$ reconstructed from isoconversional kinetic method of polystyrene pyrolysis for 3, 5, 7.5, and 10 K·min⁻¹ heating rates. The dash line means the reconstructed profile of modified Avrami–Eroféev reaction model.

By further processing experimental data of each heating rate, sixteen sets of m and n parameters are obtained. We find that there is a roughly linear relationship between all m and n , which can be described by $m = 0.39n - 1.15$ with $R^2 = 0.92$. Then, the pyrolysis model function can be rewritten by

$$f(\alpha) = n\alpha^{0.39n - 1.15}(1 - \alpha)[- \ln(1 - \alpha)]^{1 - 1/n} \tag{16}$$

As shown in Figure 6, four sample size experimental data were put together for model reconstruction since the reconstruction model lines in Figure 5 show similar variations. Results showed that for all four sample sizes, the reaction model can be described as $f(\alpha) = 2.02\alpha^{-0.27}(1 - \alpha)[-\ln(1 - \alpha)]^{0.50}$. It can be concluded that the pyrolysis model, $f(\alpha)$, cannot be influenced by sample particle size because the geometric dimension cannot change the chemical reaction principles. Although the reaction model function $f(\alpha)$ cannot be influenced by particle size, the activation energies and reaction rate can be influenced greatly because the specific surface area can influence the heat transfer and evaporation rate of the particle surface.

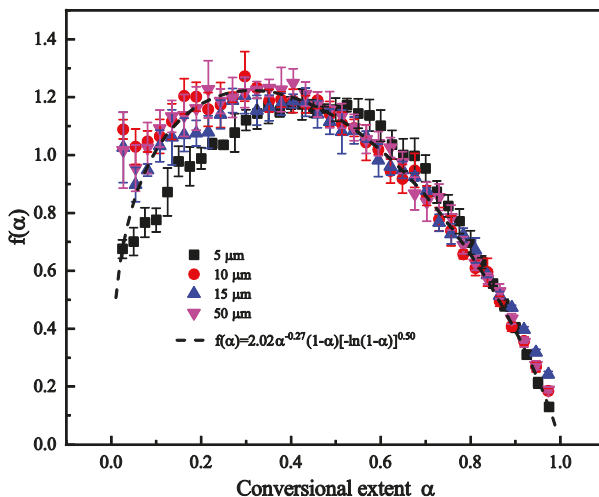


Figure 6. The experimental kinetics function $f(\alpha)$ reconstructed for 5, 10, 15, and 50 μm sample size.

It should be noted that in previous literatures about polymer pyrolysis model identification, it is far from enough that only linearity coefficients are obtained, by which the models are ranked. For each model will have its one linearity coefficient, and there must exist one model with the highest fitness; which however, does not mean that this model can describe the pyrolysis process well, especially when fitting with experimental data. Figures 5 and 6 shows that the reconstructed model can describe the experimental well after modification, though the format of the final model shows difference with traditional nineteen models. We can also call the final reaction model an apparent model, which can be regarded as the combination of several step reaction models.

6.5. Step-Reaction Separation by Distributed Activation Energy Method

By traditional kinetics methods, we can only see that the activation energies are different for different sample size, while we cannot distinguish which step reaction makes the difference on pyrolysis kinetics. So, in this section, distributed activation energy method was employed to separate the step reaction from overall pyrolysis reaction, by which we can see the weight of step reaction on activation energy for different particle sizes. Details about the mechanism of DAEM have been introduced in Section 4, and the solution of DAEM equations was based on programming MATLAB to obtain the kinetics parameters. To improve the accuracy of kinetic results, experimental data of α and $d\alpha/dt$ was employed to fit by DAEM model at the same time, which was judged by getting the minimum value of squared sum residuals (SSR), which can be expressed by

$$SSR = \sum_{n=1}^e \sum_{m=1}^f \left\{ \left[\alpha_{num}(T_k) - \alpha_{exp}(T_k) \right]^2 + \left[\left(\frac{d\alpha}{dT_k} \right)_{num} - \left(\frac{d\alpha}{dT_k} \right)_{exp} \right]^2 \right\} \quad (17)$$

where e and f mean all heating rates and selected experimental data points. The subscripts num and exp mean the numerical DAEM model and experimental data, respectively.

For PS pyrolysis in nitrogen, the pyrolysis mechanism has been explored a lot. It is generally acknowledged that the pyrolysis process can be divided into two steps. The first step is the pyrolysis of the main PS structure with a generation of large volatile molecules, during which the structure will show a large mass loss. The second step is the generation of single molecule styrene mainly from the large molecule and a little bit from the residual body. During the DAEM calculation, we hypothesize that PS pyrolysis process includes two reaction steps. Equations (9)–(14) were solved based on genetic algorithm (GA) in MATLAB. GA is an advanced algorithm based on Darwin's evolution theory, searching the best fitness in solving a high-dimensional optimization problem. For each new generation, GA will generate a certain amount of individuals randomly and simultaneously, among which each individual will be employed to fit with experimental data with fitness obtained. The individual with best fitness will be adopted as a parent to produce next generation. During producing, each generation process, selection, interaction, cross, and variation are all considered. Finally, one individual with best fitness is identified as the final parameters.

The aforementioned two-pseudo-component pyrolysis mechanism was employed during DAEM, and the searching ranges for four parameters, natural logarithm of pre-exponential factor, standard derivation of Gaussian distribution, activation energy, and weight factor were 5–60, 0–15 kJ mol^{-1} , 100–380 kJ mol^{-1} , and 0–1, respectively. In each heating rate, 100 points with uniform intervals were selected from the original data during the 600–900 K temperature range. Table 5 shows the DAEM calculation parameters with best fitness for two component reactions hypothesis. Figure 7 shows the activation energy distributions for both step reactions. From Table 5 and Figure 7, we can find that the activation energy distributions of 5 μm is more concentrated than the other three particle sizes especially for the second step reaction at 260–290 kJ mol^{-1} , which means the 5 μm particle is much easier to pyrolyze compared with other particles, and the first step reaction group is more concentrated. The centered activation energy increases with particle size increasing in both reaction processes, which is in accordance with the results by the isoconversional method. Obviously, the particle size effects on the second reaction are more obvious than the first step reaction.

Table 5. Distributed activation energy method (DAEM) fitness for different particle size with different heating rates.

Component	Parameter	5 μm	10 μm	15 μm	50 μm
Component 1	$\ln A_1$	38.7179	40.8492	42.6370	42.4292
		0.0063	2.2146	2.3269	2.4410
	$E_{0,1}$	262.9934	272.7594	283.5884	283.0256
	n_1	0.9004	0.8426	0.8339	0.8613
Component 2	$\ln A_2$	16.3841	18.9673	21.2544	21.8706
		4.7951	9.1801	9.1128	8.9726
	$E_{0,2}$	145.3102	155.9962	169.6331	176.2200
	n_2	0.1153	0.1614	0.1744	0.1430

Figure 8 shows the experimental α and da/dt , DAEM fitting α and da/dt , and step reaction distributions. We can find that the experimental data and DAEM fitting can match each other reasonably well for all sixteen cases. And the mass loss by the first reaction occupies most of the reaction.

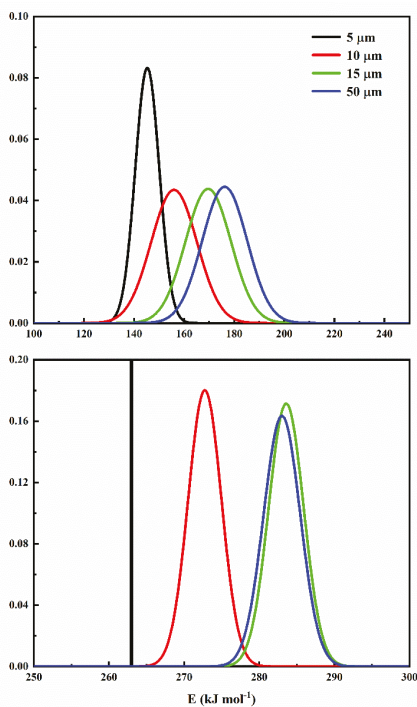


Figure 7. Activation energy distribution in distributed activation energy distribution method with Gaussian distribution for four particle sizes.

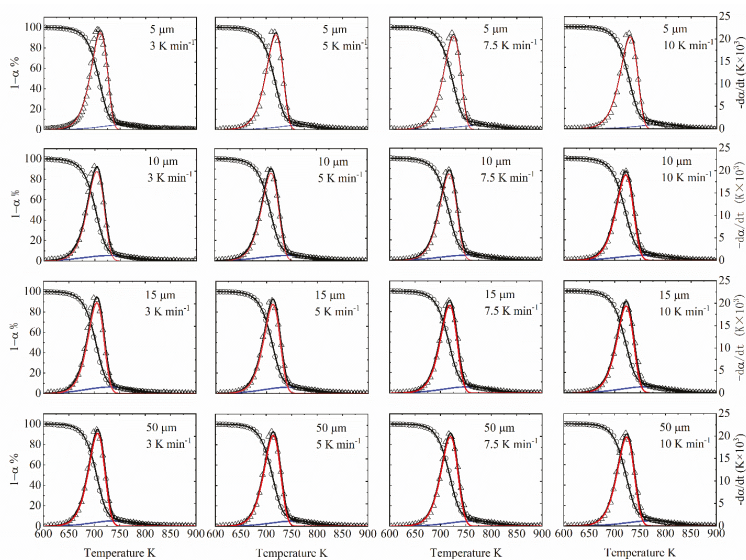


Figure 8. Comparison between DAEM calculation (solid lines, including α and $d\alpha/dt$ for overall reaction and step reactions) and experimental data (points, including α and $d\alpha/dt$) for different particle size with different heating rates.

To quantitatively show the fitness between calculation and experimental, here we use Equation (18) to evaluate the fitness, and the higher result means better fitness, here we employ the weight coefficient as 0.5, Equation (18) can be expressed as

$$Fit_{v1} = 1 - \sqrt{\sum_{m=1}^b \left[\left(\frac{d\alpha}{dT} \right)_{num} - \left(\frac{d\alpha}{dT} \right)_{exp} \right]^2 / f / \left[\left(\frac{d\alpha}{dT} \right)_{exp} \right]_{max}} \quad (18a)$$

$$Fit_{v2} = 1 - \sqrt{\sum_{m=1}^b (\alpha_{num} - \alpha_{exp})^2 / f / (\alpha_{exp})_{max}} \quad (18b)$$

$$Fit_v = [\kappa Fit_{v1} + (1 - \kappa) Fit_{v2}] \times 100\% \quad (18c)$$

Table 6 shows the fitness results for different heating rates during DAEM fitting. We can see all fitness are larger than 98.5%, which proves the good performance of DAEM in TGA and DTG curve prediction.

Table 6. DAEM fitness for different particle size with different heating rates.

Particle Size	Fitness			
	3 K min ⁻¹	5 K min ⁻¹	7.5 K min ⁻¹	10 K min ⁻¹
5 μm	98.06	98.01	98.20	98.29
10 μm	98.39	98.77	98.77	98.78
15 μm	98.13	98.74	98.75	98.71
50 μm	98.52	98.72	98.70	98.79

6.6. Sensitivity Analysis of DAEM Parameters

After calculating the DAEM parameters of different particles, we also need to carry out the sensitivity analysis to judge which parameter is more important and sensitive. The method to check its sensitivity is to change the target parameter by a small value and remain the rest parameters unchanged. The variation range of parameter is very small, here we employ the range ±0.1. lg(ssr) to quantitatively judge the parameter sensitivity, where ssr is the SSR with changed parameter divided by the optimal SSR value. Parameters lnA₁, σ, E_{0,1}, n₁, and lnA₂, σ, E_{1,2}, n₂, are numbered as 1–8 as shown in y-axis of Figure 9, where x-axis means the relative changed value of parameters ranging from 0.9 to 1.1, y-axis means the order of eight parameters, and the color value in Figure 9 means lg(ssr). The blue color presents that the parameter is insensitive and accurate, while the red color means sensitive to the value change. So, during calculation, we should check the accuracy of these sensitive parameter to make sure its accuracy. Obviously, the pre-exponential factor and activation energy we obtained by DAEM methods are insensitive compared with weight factor and distribution factor, which means the result is reasonably dependable. Here in Figure 9, the data is 50 μm PS pyrolysis DAEM parameters. The parameters of other particle sizes show the same weight with 50 μm particle, so here we won't discuss other particle size cases anymore.

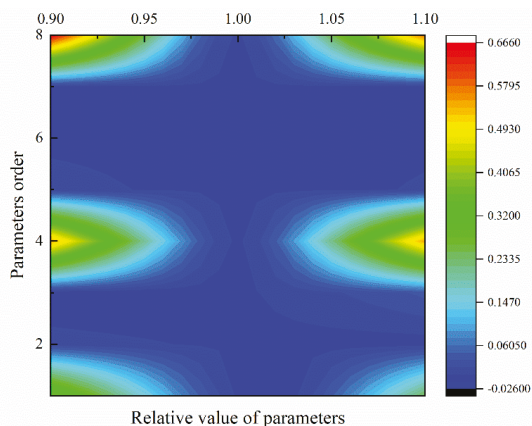


Figure 9. Sensitivity of eight DAEM parameters for 50 μm PS pyrolysis. This figure shows 50 μm PS particle case, and the sensitivity of other particles shows the same weight distribution.

7. Conclusion

Here we explore the particle size effects on pyrolysis of polystyrene from aspects of pyrolysis behavior, kinetics, reaction model, reconstruction, and validation. The final reaction model can provide scientific guidance to polymer pyrolysis modeling [22–27]. In this study, to explore the particle size effects on pyrolysis behavior, polystyrene particles with four different sizes, 5, 10, 15, and 50 μm , were selected to conduct a series of TG experiments. Isoconversional methods were employed to calculate kinetic parameters during all conversional extents. Results show that the temperature of the DTG curve peak will decrease first, then increase with particle size for the same heating rate, which may be caused by the competition of compactness and specific surface area effects. During the main pyrolysis stage, with the increase of conversional extent, activation energies decrease slowly and linearly for all four size samples. With the increase of particle size, the activation energies will increase for the same conversional extent, which means that the reaction of the largest particle is the hardest to trigger. The Avrami–Eroféev model was identified by the Coats–Redfern method as the controlling model during the polystyrene pyrolysis process. Considering the accommodation function of the reaction model, Avrami–Eroféev model was modified as $f(\alpha) = 2.02\alpha^{-0.27}(1-\alpha)[- \ln(1-\alpha)]^{0.50}$, by which the polystyrene pyrolysis process can be well explained. To find the weight of each step reaction, the DAEM model was employed to separate the step reaction from overall reaction. Results showed that both step reactions can be largely influenced by particle size, especially for the second step. For the five μm particle, the activation energy distributions in both step reactions are more concentrated and forward, and its reaction is more uniform.

Author Contributions: Conceptualization, L.J. and J.-H.S.; methodology, L.J., Q.X., O.D. and J.-H.S.; software, L.J.; validation, L.J., O.D.; formal analysis, L.J., X.-R.Y.; investigation, L.J.; resources, L.J., X.G.; data curation, L.J., J.-H.S.; writing—original draft preparation, L.J., O.D., Q.X., J.-H.S.; writing—review and editing, L.J., O.D., Q.X., J.-H.S.; visualization, L.J., M.K.K.; supervision, Q.X., J.-H.S.; project administration, L.J.; funding acquisition, L.J., Q.X., O.D., and M.K.K. All authors have read and agreed to the published version of the manuscript.

Funding: The authors would like to thank the National Natural Science Foundation of China (NSFC, Grant 51806208), the joint project of NSFC and STINT (51911530151, China side, and CH2018-7733, Sweden side), Slovenian Research Agency for project BI-CN/18-20-016, and Slovenia–China joint research fund 12-22. Oisik Das expresses his gratitude to Bio4Energy. Manja Kitek Kuzman thanks Slovenian Research Agency for financial support within the scope of the program P4-0015, as well as BI-CN/18-20-016.

Conflicts of Interest: The authors declare no conflicts of interest.

References

1. Zhang, D.; Jiang, L.; Lu, S.; Cao, C.; Zhang, H.-P. Particle size effects on thermal kinetics and pyrolysis mechanisms of energetic 5-amino-1h-tetrazole. *Fuel* **2018**, *217*, 553–560. [[CrossRef](#)]
2. Ding, Y.; Fukumoto, K.; Ezekoye, O.A.; Lu, S.; Wang, C.; Li, C. Experimental and numerical simulation of multi-component combustion of typical charring material. *Combustion Flame* **2020**, *211*, 417–429. [[CrossRef](#)]
3. Ding, Y.; Zhang, W.; Yu, L.; Lu, K. The accuracy and efficiency of GA and PSO optimization schemes on estimating reaction kinetic parameters of biomass pyrolysis. *Energy* **2019**, *176*, 582–588. [[CrossRef](#)]
4. Jiao, L.; Xu, G.; Wang, Q.; Xu, Q.; Sun, J. Kinetics and volatile products of thermal degradation of building insulation materials. *Thermochim. Acta* **2012**, *547*, 120–125. [[CrossRef](#)]
5. Jiao, L.; Sun, J. A thermal degradation study of insulation materials extruded polystyrene. *Procedia Eng.* **2014**, *71*, 622–628. [[CrossRef](#)]
6. Cheng, J.; Pan, Y.; Yao, J.; Wang, X.; Pan, F.; Jiang, J. Mechanisms and kinetics studies on the thermal decomposition of micron Poly (methyl methacrylate) and polystyrene. *J. Loss Prev. Process Ind.* **2016**, *40*, 139–146. [[CrossRef](#)]
7. Shen, J.; Wang, X.S.; Garcia-Perez, M.; Mourant, D.; Rhodes, M.J.; Li, C.Z. Effects of particle size on the fast pyrolysis of oil mallee woody biomass. *Fuel* **2009**, *88*, 1810–1817. [[CrossRef](#)]
8. Marcilla, A.; García, A.N.; Pastor, M.V.; León, M.; Sánchez, A.; Gómez, D. Thermal decomposition of the different particles size fractions of almond shells and olive stones. Thermal behaviour changes due to the milling processes. *Thermochim. Acta* **2013**, *564*, 24–33. [[CrossRef](#)]
9. Di Blasi, C. Kinetic and heat transfer control in the slow and flash pyrolysis of solids. *Ind. Eng. Chem. Res.* **1996**, *35*, 37–46. [[CrossRef](#)]
10. Hanson, S.; Patrick, J.W.; Walker, A. The effect of coal particle size on pyrolysis and steam gasification. *Fuel* **2002**, *81*, 531–537. [[CrossRef](#)]
11. Yu, D.; Xu, M.; Sui, J.; Liu, X.; Yu, Y.; Cao, Q. Effect of coal particle size on the proximate composition and combustion properties. *Thermochim. Acta* **2005**, *439*, 103–109. [[CrossRef](#)]
12. Kissinger, H.E. Reaction kinetics in differential thermal analysis. *Anal. Chem.* **1957**, *29*, 1702–1706. [[CrossRef](#)]
13. Akahira, T.; Sunose, T. Method of determining activation deterioration constant of electrical insulating materials. *Res. Rep. Chiba. Inst. Technol.* **1971**, *16*, 22–31.
14. Flynn, J.H.; Wall, L.A. A quick, direct method for the determination of activation energy from thermogravimetric data. *J. Polym. Sci. Pol. Lett.* **1966**, *4*, 323–328. [[CrossRef](#)]
15. Ozawa, T. A new method of analyzing thermogravimetric data. *Bull. Chem. Soc. Jap.* **1965**, *38*, 1881–1886. [[CrossRef](#)]
16. Tang, W.; Liu, Y.; Zhang, H.; Wang, C. New approximate formula for Arrhenius temperature integral. *Thermochim. Acta* **2003**, *408*, 39–43. [[CrossRef](#)]
17. Tang, W.; Chen, D.; Wang, C. Kinetic study on the thermal dehydration of $\text{CaCO}_3 \cdot \text{H}_2\text{O}$ by the master plots method. *Aiche J.* **2006**, *52*, 2211–2216.
18. Vyazovkin, S.; Dollimore, D. Linear and nonlinear procedures in isoconversional computations of the activation energy of nonisothermal reactions in solids. *J. Chem. Inf. Comput. Sci.* **1996**, *36*, 42–45. [[CrossRef](#)]
19. Vyazovkin, S. Advanced isoconversional method. *J. Anal. Calorim.* **1997**, *49*, 1493–1499. [[CrossRef](#)]
20. Vyazovkin, S. Evaluation of activation energy of thermally stimulated solid-state reactions under arbitrary variation of temperature. *J. Comput. Chem.* **1997**, *18*, 393–402. [[CrossRef](#)]
21. Farjas, J.; Roura, P. Isoconversional analysis of solid state transformations. *J. Anal. Calorim.* **2011**, *105*, 757–766. [[CrossRef](#)]
22. Li, K.Y.; Huang, X.; Fleischmann, C.; Rein, G.; Ji, J. Pyrolysis of medium-density fiberboard: Optimized search for kinetics scheme and parameters via a genetic algorithm driven by Kissinger's method. *Energy Fuels* **2014**, *28*, 6130–6139. [[CrossRef](#)]
23. Li, K.; Pau, D.S.W.; Wang, J.; Ji, J. Modelling pyrolysis of charring materials: Determining flame heat flux using bench-scale experiments of medium density fibreboard (MDF). *Chem. Eng. Sci.* **2015**, *123*, 39–48. [[CrossRef](#)]
24. Li, K.Y.; Pau, D.S.W.; Hou, Y.N.; Ji, J. Modeling pyrolysis of charring materials: Determining kinetic properties and heat of pyrolysis of medium density fiberboard. *Ind. Eng. Chem. Res.* **2013**, *53*, 141–149. [[CrossRef](#)]

25. Gao, X.; Jiang, L.; Xu, Q.; Wu, W.-Q.; Mensah, R.A. Thermal kinetics and reactive mechanism of cellulose nitrate decomposition by traditional multi kinetics and modeling calculation under isothermal and non-isothermal conditions. *Ind. Crop. Prod.* **2020**, *145*, 112085. [[CrossRef](#)]
26. Li, K.; Pau, D.S.; Zhang, H. Pyrolysis of polyurethane foam: Optimized search for kinetic properties via simultaneous K-K method, genetic algorithm and elemental analysis. *Fire Mater.* **2016**, *40*, 800–817. [[CrossRef](#)]
27. Chen, R.; Xu, X.; Lu, S.; Zhang, Y.; Lo, S. Pyrolysis study of waste phenolic fibre-reinforced plastic by thermogravimetry/Fourier transform infrared/mass spectrometry analysis. *Energy Convers. Manag.* **2018**, *165*, 555–566. [[CrossRef](#)]
28. Chen, R.; Li, Q.; Zhang, Y.; Xu, X.; Zhang, D. Pyrolysis kinetics and mechanism of typical industrial non-tyre rubber wastes by peak-differentiating analysis and multi kinetics methods. *Fuel* **2019**, *235*, 1224–1237. [[CrossRef](#)]
29. Kong, S.; Huang, X.; Li, K.; Song, X. Adsorption/desorption isotherms of CH₄ and C₂H₆ on typical shale samples. *Fuel* **2019**, *255*, 115632. [[CrossRef](#)]
30. Gao, Z.; Wan, H.; Ji, J.; Bi, Y. Experimental prediction on the performance and propagation of ceiling jets under the influence of wall confinement. *Energy* **2019**, *178*, 378–385. [[CrossRef](#)]
31. Vand, V. A theory of the irreversible electrical resistance changes of metallic films evaporated in vacuum. *Proc. Phys. Soc.* **1943**, *55*, 222. [[CrossRef](#)]
32. Pitt, G.J. The kinetic of the evolution of volatile products from coal. *Fuel* **1962**, *41*, 267–274.
33. Cao, H.Q.; Duan, Q.L.; Chai, H.; Li, X.-X.; Sun, J.-H. Experimental study of the effect of typical halides on pyrolysis of ammonium nitrate using model reconstruction. *J. Hazard. Mater.* **2020**, *384*, 121297. [[CrossRef](#)] [[PubMed](#)]
34. Li, M.; Jiang, L.; He, J.J.; Sun, J.-H. Kinetic triplet determination and modified mechanism function construction for thermo-oxidative degradation of waste polyurethane foam using conventional methods and distributed activation energy model method. *Energy* **2019**, *175*, 1–13. [[CrossRef](#)]
35. Chai, H.; Duan, Q.; Jiang, L.; Gong, L.; Chen, H.; Sun, J. Theoretical and experimental study on the effect of nitrogen content on the thermal characteristics of nitrocellulose under low heating rates. *Cellulose* **2019**, *26*, 763–776. [[CrossRef](#)]
36. Koga, N.; Malek, J. Accommodation of the actual solid-state process in the kinetic model function. Part 2. Applicability of the empirical kinetic model function to diffusion-controlled reactions. *Thermochim. Acta* **1996**, *282*, 69–80. [[CrossRef](#)]



© 2020 by the authors. Licensee MDPI, Basel, Switzerland. This article is an open access article distributed under the terms and conditions of the Creative Commons Attribution (CC BY) license (<http://creativecommons.org/licenses/by/4.0/>).